Kinetics and Connectivity of Grain Boundaries in Three-dimensional Metallic Systems

by

Jiwoong Kang

A dissertation submitted in partial fulfillment
of the requirements for the degree of
Doctor of Philosophy
(Chemical Engineering)
in the University of Michigan
2022

Doctoral Committee:

Assistant Professor Ashwin J. Shahani, Chair
Professor John E. Allison
Professor Sharon C. Glotzer
Professor Robert M. Ziff

Jiwoong Kang

kangjw@umich.edu

ORCID iD: 0000-0002-9118-6845

Dedication

To my family and friends

Acknowledgements

I would like to express my sincere gratitude to my advisor Prof. Ashwin J. Shahani for his unwavering support and invaluable guidance throughout my time as a graduate student at University of Michigan. Under his exceptional mentorship, I have grown and progressed as an engineer, a scientist, and a presenter. I would like to thank the committee members: Prof. Sharon C. Glotzer, Prof. Robert Ziff, and Prof. John E. Allison, for providing insightful feedback. Their constructive critique and suggestion during meetings helped me enrich my dissertation work.

I would also like to thank every member of the Shahani research group, Dr. Ning Lu, Dr. Nancy Senabulya, Dr. Hadi Parsamehr, Dr. Insung Han, Dr. Saman Moniri, Dr. Yeqing Wang, Dr. Caleb Reese, Dr. Shanmukha Kiran, Paul Chao, Geordie Lindemann, Marcel Chlupsa, Aaron Gladstein. I thank them not only for sharing their thoughts and ideas, but also for making my years at Michigan enjoyable with great friendship.

Special thanks to my research collaborators: Prof. Robert Suter (Carnegie Mellon University) for sharing insight on x-ray imaging techniques, Dr. Hrishikesh Bale (Carl Zeiss Microscopy) for providing state-of-the-art laboratory x-ray diffraction microscopic capabilities, Dr. Matthew Streeter & Dr. Robert Shalloo (Imperial College London) for experimental assistance, Prof. Paul Sanders (Michigan Technological University) for supporting mechanical processing capabilities.

I would like to thank my family for being my biggest supporter through this journey. Thank you to my parents, Bongsoo Kang and Ae-Ja Oh, for unconditional support and encouragement to pursue my passion. Thank you to my parents-in-law, Yoonik Cha and Wehyang Choi, for warm

encouragement. My biggest appreciation goes to my wife, Hyunji Cha, for being always there for me. I am grateful to have you by my side to share everything. Lastly, I thank my son, Leo, for his emotional support by his presence

Table of Contents

List of Tables

List of Figures

Abstract

As the intrinsic microstructure of polycrystalline materials governs their properties, it is of fundamental interest to understand the underlying microstructures and their evolution mechanisms. Despite decades of research on this topic, many open questions remain unanswered (see **Chapters 1-4**). This is mainly because conventional experimental approaches provide limited information on microstructures either spatially (two-dimensional) or temporally (destructive). Thus, in this dissertation, nondestructive three-dimensional modalities (**Chapter 5**), namely absorption contrast tomography (ACT) and laboratory-based diffraction contrast tomography (LabDCT), are employed to capture the evolution of three-dimensional microstructures in polycrystalline materials. Armed with these techniques, this dissertation examines two scientific phenomena: (1) *abnormal grain growth* and (2) *percolation behavior of grain boundary networks*.

Firstly, **Chapter 6** of this dissertation describes the newly developed in-house 3D x-ray diffraction (3DXRD) data processing framework, *PolyProc*. As LabDCT becomes more and more accessible, needs are placed on developing data processing frameworks that are as efficient as possible. *PolyProc* fulfills the demand as it can intake a range of 3DXRD datasets and output analysis-ready datasets with further functionalities, such as a visualization and grain statistics. The framework is heavily utilized throughout the following chapters.

The following **Chapter 7 and 8** focus on identifying the mechanism of abnormal grain growth (AGG) in a particle-containing alloy. By integrating ACT and LabDCT, we capture occurrence of AGG together with the spatial distributions of second phase particles. The holistic

view of microstructure enables us to conclude that distribution of articles determines the trajectories of grain boundaries. That is, the particle distribution is highly correlated to the occurrence of AGG. We further investigate the origin of non-random particle distribution, which manifests during the isothermal anneal close to the solvus temperature. We find that it stems from residual segregation of the solute phase following solidification.

Finally, **Chapter 9** covers the percolation behavior of 3D polycrystalline materials. By collecting a large-scale 3D grain structure by LabDCT, we determine a percolation threshold of the high angle grain boundaries. We harness finite-size scaling analysis from bond percolation theory. We further confirm good agreement of the threshold with the theoretical result, validating the applicability of percolation theory on grain boundary networks. We further investigate the percolation behavior of triple junction (TJ) lines, which we confirm to show a lower percolation threshold than GB. We also observe vastly different percolation behaviors between TJ networks and theoretical diamond lattice, despite their topological similarities. We attribute the discrepancy to hyper-coordination of nodes and a spatial clustering of TJs in the microstructure.

Overall, the findings in the dissertation expand our knowledge on kinetics and connectivity of grain boundaries in 3D metallic systems, which can contribute for designing efficient metallurgical processing methods and tailored microstructures for industrial applications.

Part I. Introduction

Chapter 1. Microstructure of Polycrystals

Solid materials can be classified based on the degree of arrangement in their crystal structures. A *single crystal* (or monocrystal) refers a solid consisting of a continuous lattice. At the other extreme, an *amorphous material* refers to a solid with no apparent long-range order. Other solids that fall into the middle of the spectrum between these two structures are called *polycrystalline materials*. Polycrystals are comprised of a number of microscopic crystals (grains) with different sizes, shapes, and crystallographic orientations (**Figure. 1.1**). A discontinuity of the lattice (grain) structure occurs at the interface between two facing grains and this planar defect is called a *grain boundary*. Grain boundaries are of interest as they possess an excess free volume and energy due to the mismatch between two crystallographic orientations. The free volume and energy, then, are responsible for many microstructural phenomena [1,2], reviewed below.

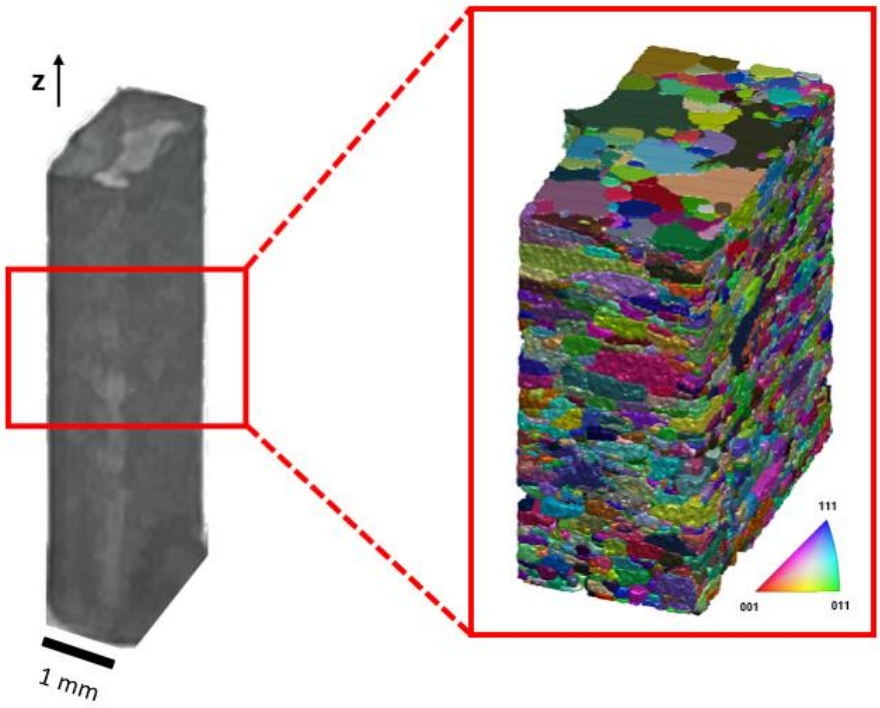

Figure 1.1. Polycrystalline microstructure of Al-3.5wt%Cu alloy, in which the Al grains are colored based on their orientation with respect to the specimen z direction.

Polycrystals are characterized by the arrangement of the grains and grain boundaries, since they vastly influence the properties of materials (*e.g.*, mechanical [3–5], chemical [6], and electrical properties [7,8]). For example, the well-known Hall-Petch relationship [3,4] explains the direct correlation between yield strength σ_y and grain size d of a polycrystal as $\sigma_y \propto d^{-1/2}$ (**Figure. 1.2**). This relationship can be explained because grain boundaries function as barriers to dislocation motion due to the discontinuity of a slip direction. Thus, in general, the smaller the grain size, the greater the surface area of grain boundaries per unit volume, and a concomitant enhancement in mechanical properties of the material as dislocation motion is impeded. Of note that the relationship starts to fail as grain size becomes nano scale (~100 nm) (namely, nanocrystalline materials) due to grain rotations, formation of shear bands, and so on [5,9–13]

In addition to their *density*, the *connectivity* of grain boundaries can influence the susceptibility towards intergranular failure modes [14–19] (*e.g.*, liquid metal embrittlement [20,21]). **Fig. 1.3** shows an example of liquid metal embrittlement, recorded in real-time. The three-dimensional reconstruction shows the liquid Ga penetrates through Al polycrystal along connected paths of failure-susceptible grain boundaries [21].

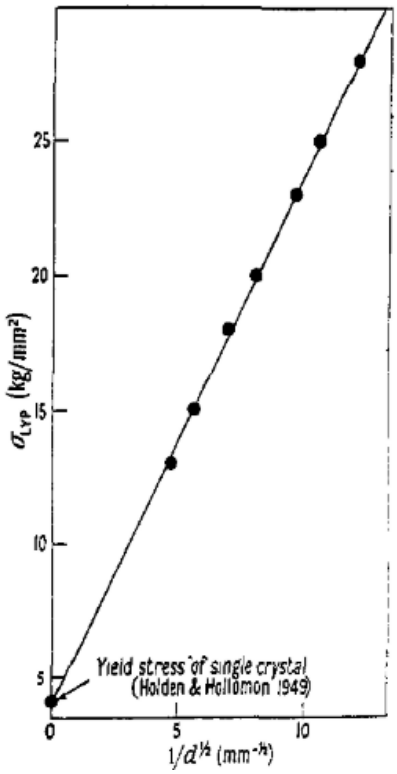

Figure 1.2. Schematic of hardness or strength (σ_y) as a function of normalized grain size (d). The grain size was calculated as average grain diameter. Reprinted from Ref. [4].

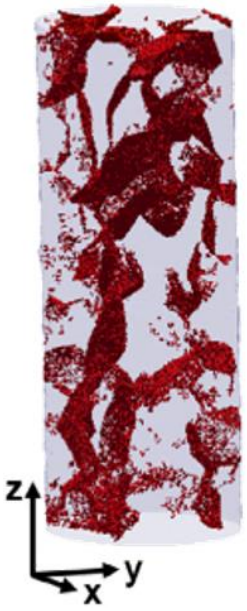

Figure 1.3. Illustration of the penetration of liquid Ga inside an Al polycrystal sample. The Ga distribution is indicated by red dots inside a translucent cylindrical Al sample. Diameter of the cylindrical Al sample is 600 μm. Reprinted from Ref. [21].

As suggested by these two illustrative examples, microstructures provide an essential fingerprint on the behavior of materials. Thus, it is of great interest to understand the fundamental origins of microstructure and its evolution during processing. In this dissertation, I investigate, more specifically, abnormal grain growth and percolation. In the rest of **Part** I, I provide an overview of the relevant background and theory for each phenomenon.

Chapter 2. A Primer on Grain Growth

Grains tend to grow in response to external stimuli (*e.g.*, heat, magnetic field). Generally, the driving force for grain growth is *capillarity* or the reduction of the excess free energy stored in the grain boundary (in the absence of other competing factors such as strain energy, *etc.*). It follows that, along a grain growth process, the density of grain boundaries decreases as a result of an increase in mean grain size. The grain growth process generally follows one of two mechanisms, *normal grain growth* (NGG) and *abnormal grain growth* (AGG). NGG occurs when grains grow continuously, maintaining a unimodal and self-similar grain size distribution in the steady state (**Fig 2.1a**). AGG refers to a discontinuous growth phenomenon in which few grains grow more rapidly compared to other grains, developing a bimodal distribution of grain size at intermediate time-scales. Eventually, the few large grains eventually impinge on one other and the system returns to unimodal distribution at long times. In a few cases, however, the abnormal grain consumes the entire microstructure, resulting in a single crystal.

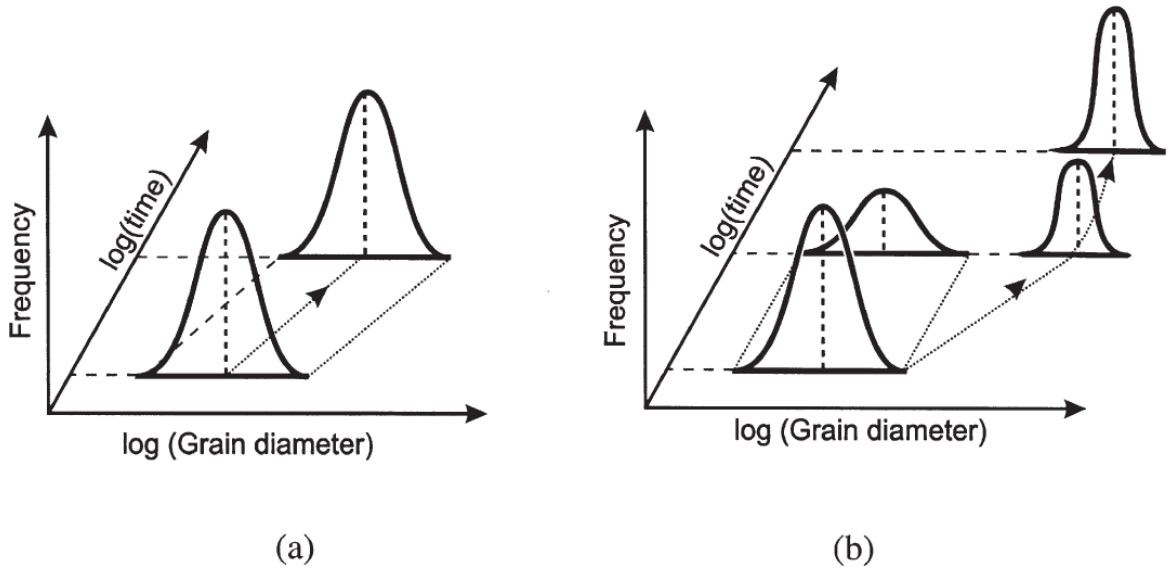

Figure 2.1. Evolution of grain size distribution over time for (a) normal grain growth (NGG) and (b) abnormal grain growth (AGG). Note in (a) that NGG retains unimodal distribution of grain size, whereas in (b) AGG develops bimodal distribution. Reprinted from Ref. [1].

The rate of grain growth depends on many factors including, but not limited to, the following. We discuss each on qualitative grounds first, and then provide quantitative details later on in **Part I**.

Temperature

Grain growth entails the migration of grain boundaries, in which the kinetics are highly influenced by temperature, through an Arrhenius-type relationship. Since the driving force for grain growth (the reduction of grain boundary density) is small (on the order of 10^{-2} MPa [22]), growth can be accelerated at elevated temperatures by providing external stimulus in the form of heat.

Second phase particles

Among the factors inhibiting grain growth, an introduction of second phase particles can hamper the migration of grain boundaries and slow down grain growth, in turn. This is because the particles "pin" the grain boundaries in the same way that they may pin dislocations.

Texture

A strong texture in materials implies a substantial fraction of low angle grain boundaries with relatively lower grain boundary energies. Thus, the capillary driving force for grain growth can be decreased due to a lower excess free energy in the system.

2.1. Theories on Normal Grain Growth

2.1.1. Burke and Turnbull model

The capillary driving pressure for grain boundary migration is related to the curvature of the boundary [23,24]. When the principal radii of curvature (R_1 and R_2) and excess energy (γ_b) of a boundary are defined, the driving pressure (P) can be modelled as

$$P = \gamma_b\left(\frac{1}{R_1} + \frac{1}{R_2}\right) \quad \textbf{(Equation 2.1)}$$

The major assumptions of the model by Burke and Turnbull is (1) a temporally and spatially uniform grain boundary energy (γ_b) and (2) the radius of curvature (R) being proportional to the mean radius ($\bar{R}$) of an individual grain. Then, using (2) and assuming further that the boundary is part of a sphere of radius ($R = R_1 = R_2$), **Equation 2.1** becomes

$$P = \frac{\alpha\gamma_b}{\bar{R}} \quad \textbf{(Equation 2.2)}$$

where α is a geometric constant.

In order to link **Equation 2.2** to a kinetic rate law, Burke and Turnbull supposed a linear relationship between the driving pressure (P) and the grain boundary velocity. That is, $\frac{dR}{dt} = cP$, where c is constant (later shown to be related to the grain boundary mobility). This linear form is consistent with the premise of linear irreversible thermodynamics [25]. Based on the assumptions, the following equations can be established:

$$\frac{d\bar{R}}{dt} = \frac{\alpha c_1 \gamma_b}{\bar{R}} \quad \textbf{(Equation 2.3)}$$

$$\bar{R}^2 - \bar{R}_0^2 = 2\alpha c_1 \gamma_b t \quad \textbf{(Equation 2.4)}$$

$$\bar{R}^2 - \bar{R}_0^2 = c_2 t \quad \textbf{(Equation 2.5)}$$

where $\bar{R}$ and $\bar{R}_0$ refer the mean grain size at time step t and the initial state at which steady-state grain growth commences, respectively, and c_2 is a constant ($c_2 = 2\alpha c_1 \gamma_b$).

Equation 2.5 indicates parabolic growth of grains. If we let $t \gg t_0$ and hence $\bar{R} \gg \bar{R}_0$, the equation can be further generalized as

$$\bar{R} = c_2 t^{1/n} \quad \textbf{(Equation 2.6)}$$

where the constant n, also known as the *grain growth exponent*, is equal to 2 for the model.

The analytically driven grain growth exponent (n) has been validated with respect to experimental measurements [26–28]. Higgins [28] reported that the values of grain growth exponent (n) are well above 2 in most metals and alloys that they tested with the general result that the exponent takes on lower values at higher temperatures. The discrepancy between theoretical value of 2 and those values obtained experimentally can be explained by various microstructural features, which are further discussed in **Chapter 2**.

Unfortunately, this model considers the ensemble-average grain size ($\bar{R}$) of the system and therefore does not tell us whether a given grain will grow or shrink. This question can be resolved by other, more sophisticated treatments of the grain growth kinetics.

2.1.2. Hillert Model

It is widely accepted that the grain boundary velocity (v) is proportional to grain boundary mobility (M) and driving pressure (P), under low driving pressures:

$$v = MP \quad \textbf{(Equation 2.7)}$$

Note this equation resembles **Equation 2.3**. Hillert's mean field theory explains how an *individual* grain grows and shrinks based on a critical grain size [29]. The mean field theory introduces a grain shape factor (g) and net curvature (κ_{net}) as follows:

$$v = M\gamma_b g\kappa_{net} \quad \textbf{(Equation 2.8)}$$

where κ_{net} refers to the sum of the inverse of principal radii of curvature of the grain boundary (*i.e.*, $\frac{1}{R_1} + \frac{1}{R_2}$) and $P = \gamma_b g\kappa_{net}$. To circumvent difficulties in the measurement of the principal radii, Hillert introduced a critical grain size (R_{cr}) to replace a part of the driving pressure, *i.e.*,

$$g\kappa_{net} = \alpha(\frac{1}{R_{cr}} - \frac{1}{R}) \quad \textbf{(Equation 2.9)}$$

where α is a dimensionless constant. Thus, combining **Equations 2.8 – 2.9** yields

$$v = M\gamma_b\alpha(\frac{1}{R_{cr}} - \frac{1}{R}) \quad \textbf{(Equation 2.10)}$$

Hillert further claimed that the critical grain size (R_{cr}) is equivalent to the mean grain size ($\bar{R}$) for a 2D system since the mean number of neighbors $\bar{n}$ of a grain is 6 and this is the critical number of neighbors that a grain must exceed in order to grow (see also **Section 2.1.3** below). So,

$$v = M\gamma_b\alpha(\frac{1}{\bar{R}} - \frac{1}{R}) \quad \textbf{(Equation 2.11)}$$

Equation 2.11 indicates that a grain will interact with a mean grain size, as is typical of mean-field models of microstructure evolution (*e.g.*, Lifshitz-Slyozov-Wagner theory of coarsening [30]). On the other hand, the critical grain size (R_{cr}) is larger than the mean grain size ($\bar{R}$) in a 3D system. The mean field model further postulates that *abnormal grain growth* (AGG) will occur for grains with twice size of the mean grain size (further discussed in **Section 2.3**).

2.1.3. Topological Aspects of Grain Growth

Due to constraints imposed by the space-filling condition, not only the boundaries of individual grains, but also the interaction between neighboring grains should be considered. The topology of polycrystals was first elaborated by Smith [31]. He explained that the normal grain growth is driven by topological requirements and surface tension equilibria at the triple junctions or triple lines between three abutting grain boundaries.

With this in mind, Von Neumann [32] and Mullins [33] proposed the basis of 2D grain growth as

$$\frac{dR}{dt} = \frac{M\gamma_b}{R}\left(\frac{N}{6} - 1\right) \quad \textbf{(Equation 2.12)}$$

where R is grain radius, M is grain boundary mobility, γ grain boundary interfacial energy, and N refers the number of sides for a given grain. This equation was derived assuming a uniform and isotropic γ_b and hence a dihedral angle at the triple junctions of 120°. **Equation 2.12** explains evolution of grains based on the number of nearest neighboring grains with critical number of 6. Thus, in 2D systems, hexagonal shape grains are metastable while grains with higher or lower number of sides will grow and shrink, respectively.

The analytical 2D von Neumann model was recently extended [34,35] to 3D and even higher dimensions using concept of mean width and triple line length:

$$\frac{dV}{dt} = -2\pi M\gamma_b\left(L(D) - \frac{1}{6}\sum_{i=1}^{n} \mathrm{e_i}\,(D)\right) \quad \textbf{(Equation 2.13)}$$

where $\frac{dV}{dt}$ is rate of a grain volume change, $L(D)$ is linear size measurement of a grain D, and $\mathrm{e_i}(D)$ is length of the i^{th} triple line of a grain D. With respect to 3D systems, other experimental [36] and theoretical [37,38] studies reported that zero integral mean curvature of the grains is achieved for an average of 13-14 grain faces. This means that the point of metastable equilibrium ($\frac{dV}{dt} = 0$) can be attained for grains with around 13-14 sides.

2.1.4. Influence of Texture on Grain Growth

Most analytical theories are based on idealized microstructure with isotropic grain boundary energy and mobility. This is reasonable for foams or froths but not for solid materials. This is because the structure of grain boundaries varies depending on the misorientation between two adjacent grains [1,2] as well as the inclination of the grain boundary plane [39]. Misorientation is defined as the difference in crystallographic orientation between two adjacent grains. Based on

the misorientation, grain boundaries can be classified as a *low angle* (LAGB) or *high angle* (HAGB). The distinction between the two classes is generally accepted as a misorientation angle of 15˚. That is, grain boundaries with a misorientation angle greater than 15˚ are classified as HAGBs, and ones with less than 15˚ are LAGBs. LAGBs are considered as an array of discrete dislocations without overlap. It means that only a fraction of the atomic arrangements is interrupted, and thus, LAGBs are generally associated with lower grain boundary energy, as noted analytically by Read and Shockley [40]. In contrast, in HAGBs, an arrangement of geometrically necessary dislocations can no longer accommodate greater than a 15˚misorientation angle. There is a greater area of interrupted lattice structure with greater excess free volume and consequently a higher grain boundary energy. In addition, there are special configurations of HAGBs that do not follow the general characteristics of HAGBs. These special boundaries are called *coincidence site lattices* (CSL). CSLs generally attain lower grain boundary energy compared to other HAGBs by two adjacent grains sharing coincident sites of the lattice. The reciprocal of the fraction of the shared lattice site is denoted by Σ. For instance, a Σ3 CSL (termed a *coherent twin boundary*) refers one out of three lattice sites that are shared between the two facing grains. As one third of lattice sites are common, such a CSL is expected to have a lower grain boundary than other HAGBs.

The mobility of grain boundaries is also highly influenced by texture of the microstructure. As the mobility of grain boundary is closely related to the misorientation, Humphreys [41] devised an expression for grain boundary mobility in the form of a sigmoidal function:

$$M = M_m(1 - e^{-5\left(\frac{\theta}{\theta_M}\right)^4}) \qquad \textbf{(Equation 2.14)}$$

where M_m is the generalized mobility of a HAGB. Of note that M_m is itself sensitive to temperature and obeys an Arrhenius type relationship. Similar to the grain boundary energy, many studies report on the importance of grain boundary mobility on grain growth [42,43].

The kinetics of grain growth can be influenced by the presence of particular types of grain boundaries. A *textured* microstructure, with a large number of grains sharing a similar orientation, results in substantial fraction of low angle grain boundaries in the system. Then, the rate of grain growth decreases as the driving pressure of growth process, which is reduction of excess free energy from grain boundaries decreases (see also **Equations 2.3** and **2.8**). The same can be said for a microstructure contains a large fraction of coincidence site lattices with relatively lower grain boundary energy. The field of *grain boundary engineering* is inspired by controlling the density of grain boundaries with relatively lower energy γ_b and/or low mobility M.

2.2. Theories on Grain Growth in Particle-containing Alloys

2.2.1 Zener-Smith Model

The presence of a stable distribution of second phase particles greatly influences the evolution of microstructure (*e.g.*, recrystallization, recovery, and grain growth) as the particles exert a pinning force or pressure on the grain boundaries. The pinning effect is known as Zener pinning in honor of the predictions made by Smith and Zener [44].

Zener pinning by a single particle

They proposed the basis of particle pinning by considering an idealized system where a single spherical particle interacts with a boundary. When a grain boundary encounters a particle at an angle β as shown in **Figure 2.2**, the drag force F acting on the line of contact is

$$F = 2\pi r\gamma_b \cos\beta \sin\beta \qquad \textbf{(Equation 2.15)}$$

The maximum drag force is obtained as

$$F_{max} = \pi r\gamma_b \qquad \textbf{(Equation 2.16)}$$

when the angle (β) is 45˚.

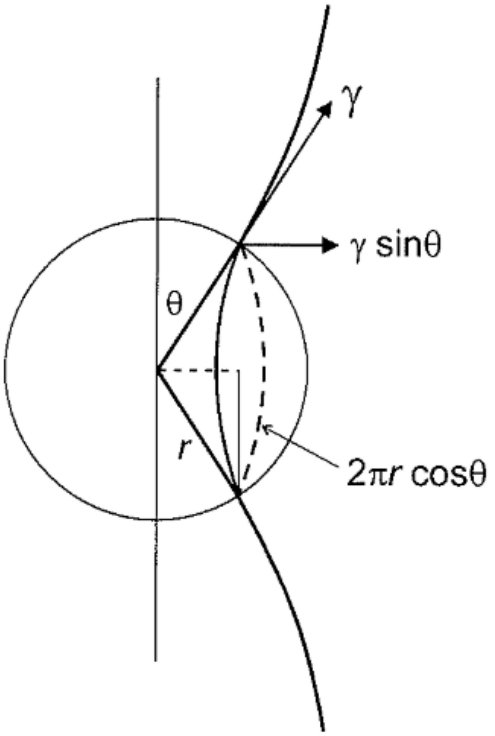

Figure 2.2. Illustration of an interaction between a grain boundary (thick line) and a spherical particle according to Zener and Smith. Reprinted from Ref. [45].

The nature of the drag force makes sense since the particle effectively removes a region of the boundary (a circle of diameter $2\pi r\cos\beta$), resulting in a decrease of overall grain boundary energy.

Smith and Zener further generalize the pinning force and evaluate the point at which the particle pinning pressure is equal to the capillary pressure for grain growth. This leads to a critical grain size (R_c) at which grain growth is fully arrested,

$$R_c = \frac{4r}{3f} \qquad \textbf{(Equation 2.17)}$$

where f is volume fraction of particles and r is the radius of the particles.

This simple criterion in **Equation 2.17** (sometimes known as the Zener equation) allows one to predict the limiting grain size provided details on the particles (r and f) are known. The Zener equation has been the basis of any theory that deals with particle containing systems. Several

modifications to the original equation have been proposed since its inception due to a number of assumptions of the original formulation. These assumptions are as follows [45]:

- Isotropic grain boundary energy
- Uniformly sized particles
- Perfectly spherical shaped particles
- Random distribution of particles
- Maximum pinning force (F_{max}) from every particle
- Incoherent particle phase
- No time-evolution of particle phase
- Grain boundary curvature being equal to grain size (see also **Equation 2.2**)

In light of these limitations, the Zener equation is often expressed in a more generalized form as

$$R_c = K\frac{r}{f^m} \quad \textbf{(Equation 2.18)}$$

where K is a dimensionless constant and m is an exponent for the volume fraction f.

Of not is that the Zener equation is not in itself a theory of grain growth in the presence of particles as it does not elaborate on the mean grain size, the grain size distribution as a function of time, and the time-invariant grain growth rate. Rather, the Zener equation provides insight on only the "pinned state" wherein the capillary driving pressure and the pinning pressure are balanced.

2.2.2. Influence of Particles on Kinetics of Grain Growth

Second phase particles will reduce the rate of grain growth as the pinning pressure necessarily opposes the capillary driving pressure. Incorporating the concept of the drag force P_z to the Burke and Turnbull model [23,24], and noting $P_z \propto \frac{1}{R_c}$, we can write

$$\frac{dR}{dt} = M(P - P_z) = M\gamma_b(\frac{\alpha}{R} - \frac{3f}{4r}) \quad \textbf{(Equation 2.19)}$$

The revised Burke and Turnbull model suggests parabolic growth of grains at initial stages and stagnation at later stages when $P = P_z$ and hence $\frac{dR}{dt} = 0$.

In a similar way, we can include the pinning force in the Hillert model as

$$\frac{dR}{dt} = M\gamma_b\left(\frac{1}{R_c} - \frac{1}{R} \pm \alpha\frac{3f}{4r}\right) \quad \textbf{(Equation 2.20)}$$

where α is constant that depends on the dimensionality of the system [1].

As can be seen, the extension of both grain growth models with respect to the pinning force are based on the original Zener equation. Thus, the accuracy of these models is highly dependent on the validity of the assumptions that enabled a straightforward derivation of the Zener equation.

2.3. Theories on Abnormal Grain Growth

Abnormal grain growth (AGG), also known as a *secondary recrystallization*, refers discontinuous grain growth process in which a few grains grow rapidly compared to other grains by consuming surrounding smaller grains. One key feature of AGG is the development of a bimodal grain size distribution. According to **Chapter 1**, an abrupt change in grain structure resulting from AGG may be considered an undesired phenomenon. Thus, preventing AGG has been an active field of study for engineering alloys. On the other hand, AGG can be beneficial for producing large-grained materials and/or single crystals [46,47].

The driving force for AGG is the reduction of grain boundary energy, similar to that of NGG. From an analytical point of view, Thompson *et al.* [48] report the conditions for AGG in an *ideal grain assembly* (*i.e.*, monophase, isotropic boundary energy and mobility). They considered a grain size R in an ideal assembly with mean grain size $\bar{R}$ and suggested a condition for AGG:

$$\frac{4R}{\bar{R}} - \frac{R^2}{\bar{R}^2} - 4 > 0 \quad \textbf{(Equation 2.21)}$$

This condition can never be satisfied because large grain will always grow more slowly than average grain, eventually rejoining the normal size distribution. Thus, AGG cannot be initiated in an *ideal* grain structure.

In contrast, in real engineering materials, AGG is a relatively common occurrence. For example, Dennis *et al*. [49] reports AGG in Al-3.5wt%Cu alloys (**Figure 2.3**). Upon annealing at 485℃, which is below the solvus temperature (491℃) of $\theta - Al_2Cu$ particle phase, abnormally large grains grew, contributing to a bimodal distribution of grain size. The open question is *which* grains are selected and *why* (the selection problem), and also *how* these grains grew into the microstructure (the persistence problem). Even though such questions on the mechanism of AGG remain unanswered, the main factors leading to AGG are thought to be

- Second-phase particles **(Section 2.3.1)**
- Texture **(Section 2.3.2)**

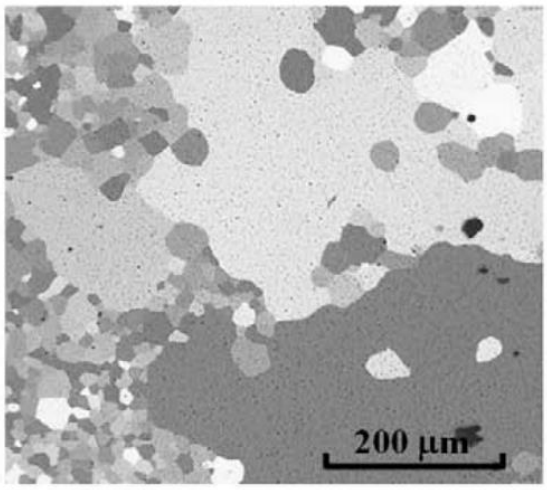

Figure 2.3. Micrograph showing abnormal grain growth in an Al-3.5wt%Cu alloy after being annealed isothermally at 485℃ for 30 minutes. The grey matrix is primary Al phase and black specks are Al_2Cu particle phase. Reprinted from Ref. [49].

2.3.1. Second-phase Particles

As discussed in **Section 2.1.4**, second phase particles inhibit grain boundary migration by exerting pinning pressure. However, like the example given in **Figure 2.3**, AGG can occur in in particle containing systems. Thus, there are many competing explanations to reconcile this counter-intuitive phenomenon.

Grain topology is strongly correlated to the size of a grain through the Lewis law [50]. Thus, it has been generally accepted that a grain with an initial size advantage, and thus a greater number of nearest neighbors, is likely initiate AGG (in a *non-ideal grain assembly*). Considering a pinned microstructure with mean grain size ($\bar{R}$) due to second phase particles, a grain with size advantage attains greater capillary driving pressure and, thus, a higher growth rate according to

$$\frac{dR_{ab}}{dt} = \frac{\alpha M \gamma_b}{\bar{R}} \quad \textbf{(Equation 2.22)}$$

where α is constant and R_{ab} is a size of a grain with size advantage (which should eventually become the abnormal grain in the microstructure). The equation indicates that a grain with a persistent size advantage will grow with a constant rate if we suppose that the mean grain size ($\bar{R}$) is fixed or constant due to the effect of particle pinning [51].

In a similar vein, Andersen *et al.* [52] analytically modelled the initiation of AGG in a 2D system and presented the results in the form of a "mechanism map." To construct it, they suggest two conditions that must be fulfilled for AGG: (1) the abnormal grain should grow and (2) it should have a higher growth rate than other normal grains. These two statements can be expressed as

$$\frac{dR_{ab}}{dt} > 0 \quad \textbf{(Equation 2.23)}$$

$$\frac{d\left(\frac{R_{ab}}{\bar{R}}\right)}{dt} > 0 \quad \textbf{(Equation 2.24)}$$

Under these conditions, they derived the mechanism map shown in **Figure 2.4.** The inner locus of the two lines (corresponding to **Equations 2.23 – 2.24**) gives the stability field for AGG (labelled "A"). In the shaded region, NGG takes over. If the pinning force is relatively weak, and hence $\frac{\bar{R}}{\bar{R}_{Lim}} \rightarrow 1$, then the large grains will be incorporated into the steady-state grain size distribution and NGG will prevail. The mechanism map shows that the critical grain size advantage for a grain to become abnormal grain to be $\frac{R_{ab}}{\bar{R}} = 1.4$ times that of the mean grain size ($\bar{R}$) when the normal grains are fully pinned ($\frac{\bar{R}}{\bar{R}_{Lim}} = 1$). This result is strictly valid for 2D grain assemblies. 3D extensions to the mechanism map are given in Refs. [34,52].

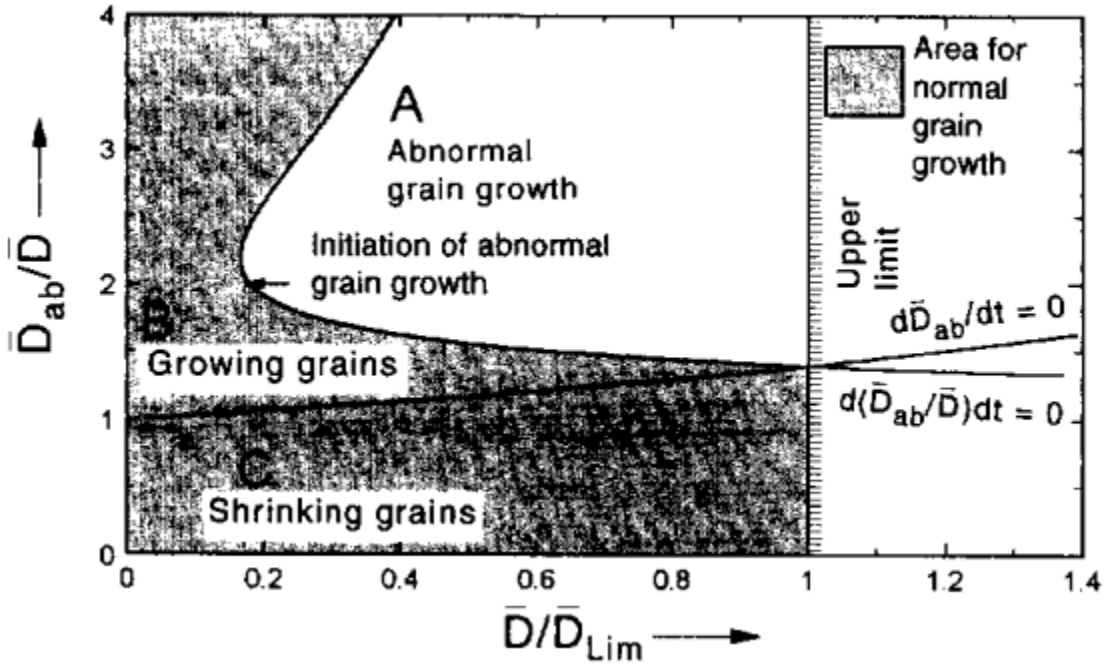

Figure 2.4. Mechanism map for abnormal grain growth based on the two conditions given in **Equations 2.22 – 2.23**. Of note that D in the figure indicates diameter, which can be equivalent of $2R$. See text for details. Reprinted from Ref. [52].

2.3.2. Texture

As mentioned in **Section 2.1.4**, the texture of microstructure influences grain growth behavior due to its influence on the grain boundary energy and mobility. AGG is commonly

observed in many polycrystalline metallic systems with strong textures [53–55]. Extensive numerical and analytical investigations on AGG in textured microstructures were conducted by Refs. [41,56,57]. For example, Humphreys correlated the tendency of AGG with how sharp or diffuse is the texture in a microstructure [41]. One with a sharp texture component tends to attain small mean misorientation ($\bar{\theta}$) between grains, resulting in a subgrain structure. Then, other grains with either random or different texture components may possess high angle grain boundaries, providing potential nuclei for AGG. A correlation map between the sharpness of texture and the occurrence of AGG is given in **Figure 2.5**. **Figure 2.5** shows the conditions under which a particular grain with misorientation angle of θ within a textured microstructure with mean misorientation of $\bar{\theta}$ will grow abnormally. Such a diagram suggests that if mean misorientation ($\bar{\theta}$) is low as $5^\circ$with sharp texture, a grain with misorientation of $\theta = 10^\circ$ can potentially grow up to ~70 times larger than the mean grain size. In contrary, if the mean misorientation ($\bar{\theta}$) is low as $15^\circ$with diffuse texture, one grain can potentially grow no larger than ~2.5 times of the mean grain size. As this is within a normal size distribution of a microstructure (indicated as shaded region), this means no AGG is expected in the microstructure.

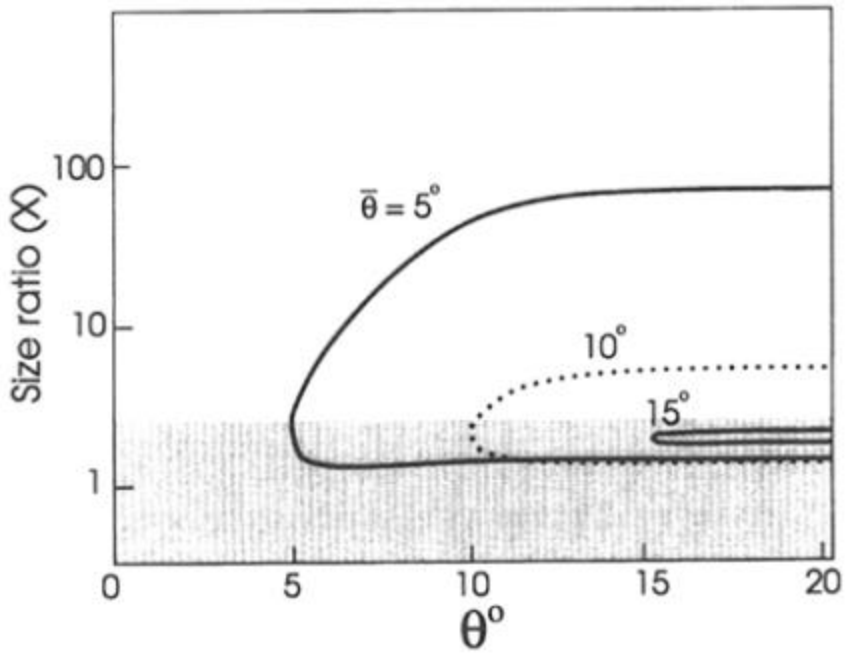

Figure 2.5. Conditions for abnormal grain growth in textured microstructure as a function of the misorientation of the grains from the microstructure and the size advantage of the abnormal grains (similar to **Figure 2.4**). The shaded region represents the range of sizes in the microstructure of 0 – 2.5 $\bar{R}$, which indicates normal size distribution of a microstructure. See text for details. Reprinted from Ref. [41].

Chapter 3. A Primer on Percolation in Grain Boundary Networks

As briefly mentioned in **Chapter 1**, the connectivity of grain boundaries can determine characteristics of an entire microstructure, especially its susceptibility with respect to intergranular failure. That is, when failure-susceptible (*i.e.*, sensitized) grain boundaries form a connected path, external stimuli (*e.g.*, oxide phase, stress, and liquid metal) can propagate more readily through the microstructure causing failure (*e.g.*, corrosion fatigue crack propagation [14,58,59], and liquid metal embrittlement [20,21], to name a few). Thus, there is renewed interest to understand the underlying structure of grain boundary networks and their connectivity.

3.1. Percolation Theory

Consider a collection of points that are distributed in space. Percolation theory [46,47] models the connectivity of the points that are linked in a random manner. The probability of the linkage is given as p. There are two basic types of percolation: *site* and *bond* percolation. The latter holds when points are fixed, and linkages (referred to as "open bonds") are made at random. The former holds when points are randomly positioned and turned on (referred to as "open sites"), and the linkages are defined based on the adjacency between open sites. In this chapter, bond percolation is of special interest due to the similarity between bonds and grain boundaries.

Percolation is achieved when there exists a path of connected points that travels infinitely far. In many applications it will be of interest to define the critical probability of open bonds for percolation. Intuitively, this critical probability, termed the *bond percolation threshold* (p_c), depends on coordination number (Z), which represents the number of bonds connected to a site.

In ideal lattices, the value of percolation threshold (p_c) regularly decreases with an increase in the coordination number (Z) as [60]

$$p_c = \frac{1}{Z}\left(\frac{d}{d-1}\right) \quad \textbf{(Equation 3.1)}$$

where d refers dimensionality of a system.

The relation intuitively make sense that the percolation is more easily attained when there are more channels to percolate.

3.1.1. Critical Behavior near Percolation Threshold ($\boldsymbol{p_c}$)

The onset of percolation is characterized by the critical behavior of geometrical properties near percolation threshold (p_c), as will be elaborated below.

Percolation probability (Π)

Π is a probability that there exists a continuous path within a single cluster of open bonds. In an infinite domain, it behaves as a step function: for $p < p_c$, percolation is not attained with only finite clusters of open bonds, and Π is zero. For $p < p_c$, Π is one. Thus, Π can be expressed as

$$\Pi(p) = \begin{cases} 0, & p < p_c \\ 1, & p \geq p_c \end{cases} \quad \textbf{(Equation 3.2)}$$

Order parameter (P_∞)

P_∞ represents the probability that a given bond belongs to an infinitely-connected, percolating path. Thus, if $p < p_c$, where percolation is not realized with only finite clusters, P_∞ is zero. Once $p \geq p_c$, P_∞ increases with p by a power law according to

$$P_\infty(p) = \begin{cases} 0, & p < p_c \\ C_P(p - p_c)^\beta, & p \geq p_c \end{cases} \quad \textbf{(Equation 3.3)}$$

where coefficient C_P is an amplitude prefactor and β is a critical exponent.

Correlation length (ξ)

ξ describes linear size of finite clusters as the mean distance between two sites on one finite cluster. As p approaches p_c, ξ increases with p through a power law relationship,

$$\xi(p) = C_\xi |p - p_c|^{-\nu} \quad \textbf{(Equation 3.4)}$$

where coefficient C_ξ is the amplitude prefactor and ν is a critical exponent.

Mass (S)

S refers the mean number of bonds contained within a finite cluster. As p becomes closer to p_c, S increases with p through a power law relationship as

$$S(p) = C_S |p - p_c|^{-\gamma} \quad \textbf{(Equation 3.5)}$$

where coefficient C_s is an amplitude prefactor and γ is another critical exponent.

The behaviors of order parameter (P_∞) and mass (S) *vs.* p are illustrated in **Figure. 3.1**.

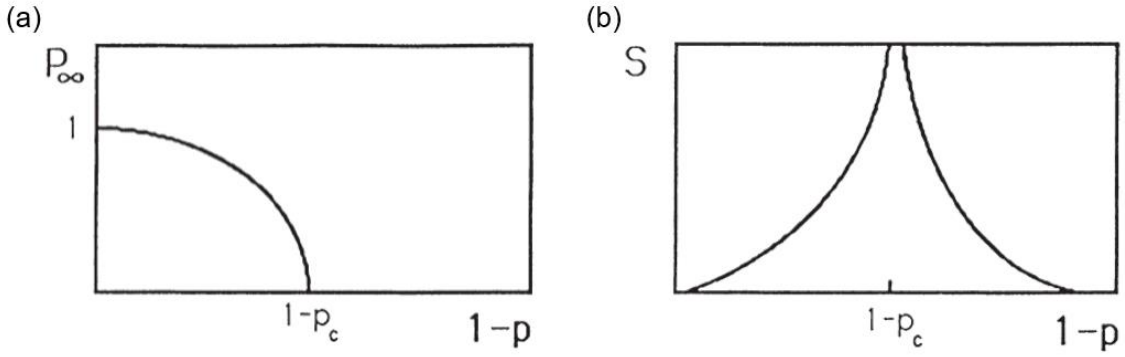

Figure 3.1. Illustration of critical behaviors of (a) order parameter (P_∞) and (b) mass (S) as a function of the fraction of open bonds p, in an infinitely large system. Reprinted from ref. [61].

3.1.2. Critical Exponents

The critical exponents β, ν, and γ introduced above describe the critical bahavior of each parameter with the percolation threshold. They are *universal constants* that only depends on the dimensionalty of a system. **Table 3.1** summarizes values of the exponents in 3D.

Table 3.1. Critical exponents for percolation theory in 3D.

Exponent	Value in 3D	Ref.
β	0.417	[61–63]
ν	0.875	
γ	1.795	

3.1.3. Finite Size Effect and Scaling Analysis

In practice, we must contend with systems that are *not* infinitely large. Considering a cubic shaped system size of size L^3, we expect different behaviors of the variables from **Section 3.1.2**, depending on the magnitude of L. When a system is large enough ($L \gg \xi$), it will practically function as if it is infinitely large ($L \to \infty$), and in this limit the variables will be independent of system size (L). Then, the following relationship between the variables are expected:

$$\xi(p) = C_\xi |p - p_c|^{-\nu} \to |p - p_c| \propto \xi^{-1/\nu} \quad \textbf{(Equation 3.6)}$$

Applying **Equation 3.6** to the order parameter (P) and mass (S), we find

$$P(p) \propto (p - p_c)^\beta \propto \xi^{-\beta/\nu} \quad \textbf{(Equation 3.7)}$$

$$S(p) \propto |p - p_c|^{-\gamma} \propto \xi^{\gamma/\nu} \quad \textbf{(Equation 3.8)}$$

However, the finite size influences the percolation behavior when $L < \xi$, *i.e.*, the correlation length (ξ) is limited by the system size (L). In this case, the variables can be expressed as

$$P(p, L) \propto (p - p_c)^\beta \propto L^{-\beta/\nu} \quad \textbf{(Equation 3.9)}$$

$$S(p, L) \propto |p - p_c|^{-\gamma} \propto L^{\gamma/\nu} \quad \textbf{(Equation 3.10)}$$

Once the order parameter (P) and mass (S) are measured for a system of known size L, we can leverage the relationships in **Equations 3.9 – 3.10** to extract the percolation threshold. That is, **Equation 3.9** implies that a plot of logarithm of order parameter ($\ln P(p, L)$) versus logarithm of system size ($\ln L$) should be linear with slope $n(L)$ given by

$$n(L) = \frac{d(\ln P)}{d(\ln L)}\Big|_{p_c} = -\frac{\beta}{\nu}$$ (**Equation 3.11**)

Therefore, the percolation threshold in an infinite system can be estimated by determining the value of p for which the slope $n(L)$ attains a value of $-\frac{\beta}{\nu}$ (or −0.477, from **Table 3.1**).

Meanwhile, the finite-sized percolation probability (Π) can be defined as a probability of percolation over an ensemble of systems, each with a given size L. That is, Π can be computed as the fraction of percolating finite systems as multiple such systems may contain a percolating pathway for a given value of p. For finite-sized systems, the behavior of Π deviates from a step function (**Equation 3.2)** and instead shows as an 'S-shaped' curve with an inflection point (not pictured). The step becomes more diffuse as the system size decreases, since there exists a finite probability that at $p < p_c$ a cluster of open bonds will span from one side of the system to the other. The converse is also true above $p > p_c$.

From the 'S-shaped' curve, two more variables can be extracted:

Point of inflection (p_{max})

p_{max} refers to the probability where the change in Π with p is maximal, *i.e.*,

$$p_{max} = \max\left(\frac{d\Pi}{dp}\right)$$ (**Equation 3.12**)

This parameter converges to p_c according to **Equation 3.13** as percolation probability (Π) is also expected to follow a general scaling law.

$$(p_{max} - p_c) \propto L^{-\frac{1}{\nu}}$$ (**Equation 3.13**)

Equation 3.13 implies that a plot of p_{max} *vs.* $L^{-\frac{1}{\nu}}$ should show a linear relationship with an intercept that gives an estimation of the percolation threshold (p_c).

Average concentration (p_{av})

p_{av} refers an average concentration of bonds at which a percolating path is attained for the first time. It can be mathematically expressed in terms of Π as

$$p_{av} = \int_0^1 p\left(\frac{d\Pi}{dp}\right)dp \qquad \textbf{(Equation 3.14)}$$

As shown from the **Equation 3.14**, p_{av} is the area under the curve of $\frac{d\Pi}{dp}$ from a purely numerical standpoint. Similar to p_{max}, p_{av} converges to p_c as

$$(p_{av} - p_c) \propto L^{-\frac{1}{\nu}} \qquad \textbf{(Equation 3.15)}$$

Equation 3.15 implies that a plot of p_{av} *vs.* $L^{-\frac{1}{\nu}}$ should show a linear relationship with an intercept that gives an estimation of the percolation threshold (p_c).

Outside of what is elaborated here, finite size scaling provides rich relationships between different percolation variables and structural properties and the percolation threshold. In **Section 3.1**, I focus only on those variables that we employ for our own analysis.

3.2. Percolation applied to Microstructure

Percolation theory provides a statistical framework to investigate the connectivity of a microstructural network. Thus far, there has been a few efforts to study the connectivity of grain boundaries in the lens of bond percolation [64–67]. Again, the bonds represent the planar grain boundaries: open bonds that are available for percolation represent failure susceptible HAGBs with relatively high free volume and energy; closed bonds represent other non-failure susceptible grain boundaries with lower grain boundary energy, such as LAGBs and CSLs. In order to invoke percolation theory, we thus assume throughout a *binary classification* of microstructural features.

3.2.1. Percolating Microstructural Features

Given a polycrystalline microstructure, different types of features may percolate in 3D, such as grain boundaries (GBs) and a triple junction lines (TJs).

Grain Boundaries (GBs)

As introduced in **Chapter 1**, the GB is a planar defect that partitions two grains with different crystallographic orientation. GBs possess an excess free volume and thus offers faster diffusion paths compare to intragranular regions with continuous lattices. For this reason, the GB is the most commonly cited percolating element for investigation of microstructure connectivity [64–66].

Triple Junction lines (TJs)

The TJ is a linear defect where three grains or GBs meet at an edge. TJs are considered to provide even faster diffusion paths compared to GBs. In nanocrystalline materials where the density of TJs is substantial, unusually high grain boundary diffusions have been attributed to connectivity of TJs [68–74]. Thus, one could also consider the TJ as a viable percolating element for investigation of microstructure connectivity. There are four different types of TJs depending on the number of failure susceptible (open) GBs ($0, 1, 2, \text{and } 3$) that meet at the TJ line. To use percolation theory, however, we must combine them into two groups: TJs with at least one failure susceptible GBs are the so-called "open" TJs, and those without any failure susceptible GBs (0) are "closed" TJs.

Quadruple Nodes (QNs)

A QN is a point defect where four grains or six GBs or four TJs meet at a point. QNs can be considered as sites, using the same language as in percolation theory. They can be classified based on the number of failure susceptible (open) GBs ($0, 1, \dots, \text{and } 6$) and the number of open TJs ($0, 1, \dots, \text{and } 4$). It follows that nine types of QNs exist (described further in **Chapter 9**).

3.2.2. Crystallographic Constraints

Polycrystals require crystallographic constraints at TJs, in order to maintain a consistency of grain orientations around the TJ line. One such constraint is known as the Σ-product rule [75],

$$\Sigma a \Sigma b = m^2 \Sigma c \qquad \textbf{(Equation 3.16)}$$

where a, b, and c refer the three GBs that meet at a TJ, and m is a common divisor of a and b. For example, at a given TJ, two Σ3 twin boundaries meet to form a Σ9 boundary. Accordingly, the misorientation of the third GB depends on other two GBs at the TJ. Consequently, the connectivity of GBs cannot necessarily be considered as random in the problem of bond percolation. Furthermore, it has been reported in Ref. [66] that the crystallographic constraints propagate to circuits drawn around QNs, involving four grains and four GBs.

3.2.3. Brandon Criterion

In **Section 3.2.1**, we introduce the idea of grouping GBs based on their relative GB energy. To distinguish between high *vs*. low grain boundary energy, we employ Brandon criterion [76]

$$\Delta\theta_{max} = \theta_0 \Sigma^{-n} \quad \textbf{(Equation 3.17)}$$

where $\Delta\theta_{max}$ is a tolerable angular deviation to a given CSL type and θ_0 is a constant of 15° for angular limit for low angle GBs and n is a constant. Different values of exponent, n, has been proposed in the literature including $\frac{1}{2}$ [76], $\frac{2}{3}$ [77], $\frac{5}{6}$ [78], or 1 [79]. In my work, I regard n as an adjustable parameter. That is, the greater a value of n, the more restrictive criterion for CSL from **Equation 3.17**, and hence the higher the fraction of failure susceptible HAGBs.

Chapter 4. Dissertation Outline

The main objective of this dissertation is to unravel longstanding questions on kinetics and connectivity of grain boundaries in metallic polycrystals by leveraging new advancements in three-dimensional x-ray imaging techniques in the laboratory.

This dissertation is organized into four main parts. Firstly, **Part I** (**Chapters 1 – 4**) serves as an introduction of the dissertation. **Chapter 1** introduces the motivation of my work and relevant terminologies regarding microstructure of polycrystals. **Chapters 2 and 3** explain the theoretical background of scientific phenomena of interest, namely the evolution and percolation of grain boundary networks. **Part II** presents an overview of three-dimensional x-ray imaging techniques used to characterize granular microstructures non-destructively. This part not only summarizes the basic working principle of the imaging techniques but also elaborates on the sample preparation and data processing routines. **Part III** is divided into **Chapters 5 – 8**, in which each chapter is based on my publications [80–82] and a forthcoming publication [83]. **Chapter 5** presents an in-house function package, *PolyProc*, for three-dimensional x-ray diffraction datasets. It includes routines to convert as-reconstructed data into processed data with other further functions that allow for statistical analyses and visualizations. **Chapters 6 – 7** investigate the mechanism of abnormal grain growth in phase-particle containing systems; since the distribution of particles is intrinsically coupled to AGG, we also investigate the origin of non-random particle distribution. **Chapter 8** reports percolation behavior of grain boundary and triple junction networks. We apply bond percolation theory to investigate the connectivity of real, three-dimensional, bulk microstructures as well as differences between grain boundary and triple junction networks. **Part IV** serves to

conclude the dissertation (**Chapter 8**) and provide an outlook into potential future studies (**Chapter 9**). An overall list of references is given in **Part V**.

Part II. Experimental Methods

Chapter 5. Non-destructive Three-dimensional X-ray Imaging Techniques

This chapter provides an overview of the core x-ray imaging techniques used for the experiments reported in this dissertation. More specific procedures, including sample preparation and data acquisition and processing, are provided in the respective chapters.

5.1. Laboratory-based X-ray Tomography

5.1.1. Basic Principles

X-ray tomography is a non-destructive 3D imaging technique that enable us to investigate the dynamics (time-evolution) of 3D bulk materials. There are many different tomographic techniques based on different interactions of x-rays with matter, *e.g.*, absorption, diffraction, and scattering. For my PhD projects, absorption and diffraction contrast tomography have been employed. Absorption contrast tomography (ACT) is based on the attenuation behavior of the *forward transmitted* x-ray beam as it penetrates the sample. That is, incident x-ray beam attenuates more easily through denser materials, resulting in lower transmission rate. That is, the mass attenuation coefficient μ scales with the atomic number Z as

$$\mu \propto \rho_a Z^4 \lambda^3 \qquad \textbf{(Equation 5.1)}$$

where ρ_a is an atomic density and λ is a wavelength of incident radiation.

The difference in attenuation, then, is utilized to distinguish between material phases with different densities and/or compositions. On the other hand, laboratory-based diffraction contrast tomography (LabDCT) is based on the *diffracted* x-ray beam that must satisfy Braggs' condition. As diffracted beam is orders of magnitude weaker compared to transmitted beam, in LabDCT, the *transmitted* x-ray beam is blocked (with a beam stop) to enhance signal-to-noise ratio of the diffraction signals.

We implement LabDCT on a Zeiss Xradia 520 Versa X-ray microscope at the Michigan Center for Materials Characterization at the University of Michigan. The source is a divergent, polychromatic x-ray beam. In **Chapters 6 – 7**, the sample is positioned according to the Laue focusing geometry, keeping the same distance between sample to source and sample to detector. Then, a grain functions as a lens to the x-rays into a diffraction spot or "steak" (**Figure 3.1**). On the other hand, recent advancements enable to overcome the restriction of the Laue focusing geometry. By implementing a flat panel detector and a new software capability in stitching multiples scans, we can achieve a projection geometry and a larger final field of view. In **Chapter 9**, these recent advancements in LabDCT are leveraged to characterize ~10,000 grains.

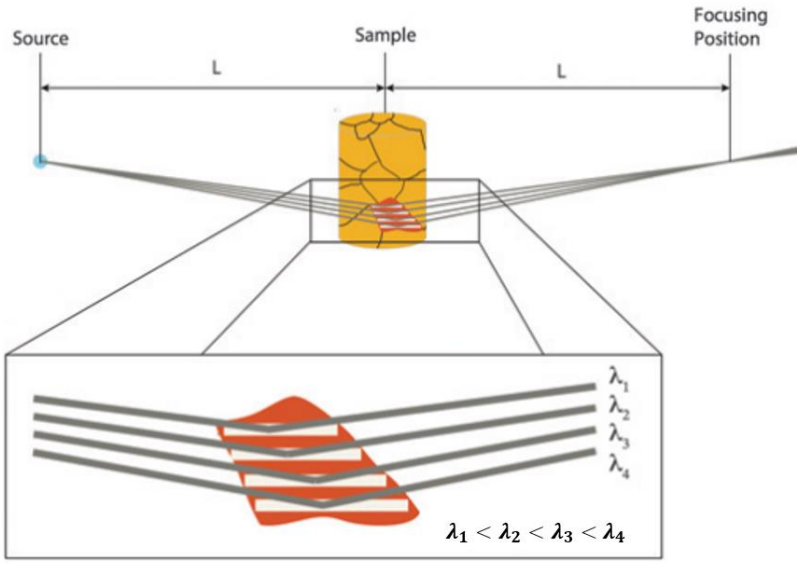

Figure 5.1. Schematic of Laue-focusing geometry, under which a divergent polychromatic x-ray beam (grey lines) is diffracted and focused by a grain (red). Reprinted from Ref. [84].

After the incident x-ray beam interacts with a sample, the transmitted or diffracted beam is absorbed by a scintillator, which converts the absorbed energy into visible light. The resulting is then detected by the CCD camera. To reconstruct 3D bulk microstructure, we collect consecutive projection images as the sample rotates about the vertical axis, with a small angular increment. Schematics of the experimental setups for both ACT and LabDCT modules are given in **Figure 3.2**. ACT **(Figure 3.2a)** and LabDCT with flat panel detector **(Figure 3.2c)** are capable of geometrical magnification due to the projection geometry. That is, by changing the sample to detector distance, the projection image can be enlarged at the cost of signal to noise ratio.

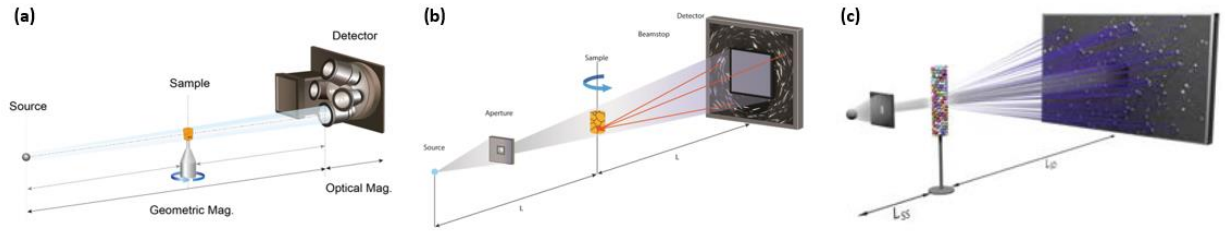

Figure 5.2. Schematics of the three types of laboratory-based X-ray tomography experiments: (a) ACT, (b) LabDCT with Laue focusing geometry, and (c) LabDCT with projection geometry. See text for details. Reprinted from Ref. [84] and courtesy of Zeiss.

5.1.2. Sample Preparation

Samples are prepared for both types of x-ray imaging experiments (ACT and DCT) starting with high purity alloy ingots prepared with the vacuum arc remelting (VAR). The Al-3.5wt%Cu was selected based on, not limited to, its suitability under x-ray microscopes (see also **Chapter 6**). The Al matrix phase and second phase θ-Al_2Cu particle phase exhibit substantial absorption contrast due to their density difference, and this contrast allows to characterize the distribution of second phase particles within the Al matrix phase through ACT. Particular attention is needed for the DCT modality as diffracted beam is orders of magnitude weaker compared to transmitted beam. That said, the Al phase is light enough to ensure large enough sample size to (1) observe bulk behavior of microstructure evolution and (2) include thousands of grains, while maintaining high enough signal to noise ratio on the detector plane. Care was taken to ensure the Al-based alloy samples were *fully recrystallized* prior to imaging under LabDCT, since residual strain can lead to a smearing of the diffraction spots on the detector and consequently artifacts in the reconstructed grain maps (see **Figure 3.3**). Such smearing makes it difficult to identify the diffracting grains.

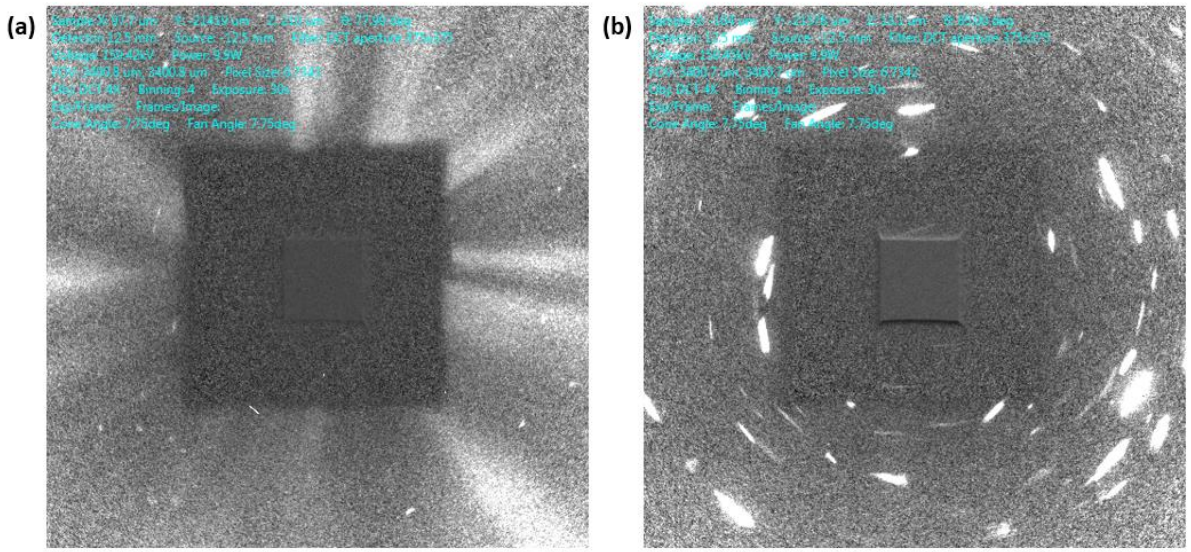

Figure 5.3. Example diffraction projection images for (a) a highly strained state and (b) a fully recrystallized state. Of note the images are taken using the same, pure Al sample. Smearing of the diffraction spots can be observed from (a), while clear diffraction streaks are observed from (b).

After proper mechanical and heat treatments (described in **Chapter 6**), the ingot was machined *via* electric discharge machining (EDM) to realize a desired geometry (typically 1 mm in diameter; any larger would lead to significant attenuation of the x-ray beam). Depending on the experiment, electropolishing with nitric acid-based electrolyte (HNO3:CH3OH = 1:2) at −20℃ was done to further decrease the sample size. This is to prevent the introduction of strain in the samples as the alloy is soft enough to be strained by mechanical polishing.

5.1.3. Data Collection and Reconstruction

The collected x-ray (projection) images from ACT were reconstructed using the filtered back projection algorithm [85] from the Scout and Scan software on the laboratory x-ray microscope. Segmentation between different phases was done by simple thresholding [86] due to clear contrast between the phases of interest. On the other hand, reconstruction of LabDCT data was performed using GrainMapper 3D^{TM} software [80,87] developed by Xnovo Technology ApS. The as-reconstructed dataset was then imported into *PolyProc*, a MATLAB-based modular processing pipeline for X-ray diffraction tomography, for further processing and analysis. Generally, the initial reconstruction data cannot be used for analysis as is due to noise in the grain maps (see **Figure 3.4** for a comparison of the data before and after processing with *PolyProc*). Thus, they are “cleaned up” based on filters for grain size, misorientation, and completeness to remove any unreliable data. Further details on these routines are elaborated in **Chapter 6**. Hereafter, completeness refers to the fraction of matching diffraction streaks between experimental projection images and calculated diffraction patterns obtained from forward modeling the reconstruction data.

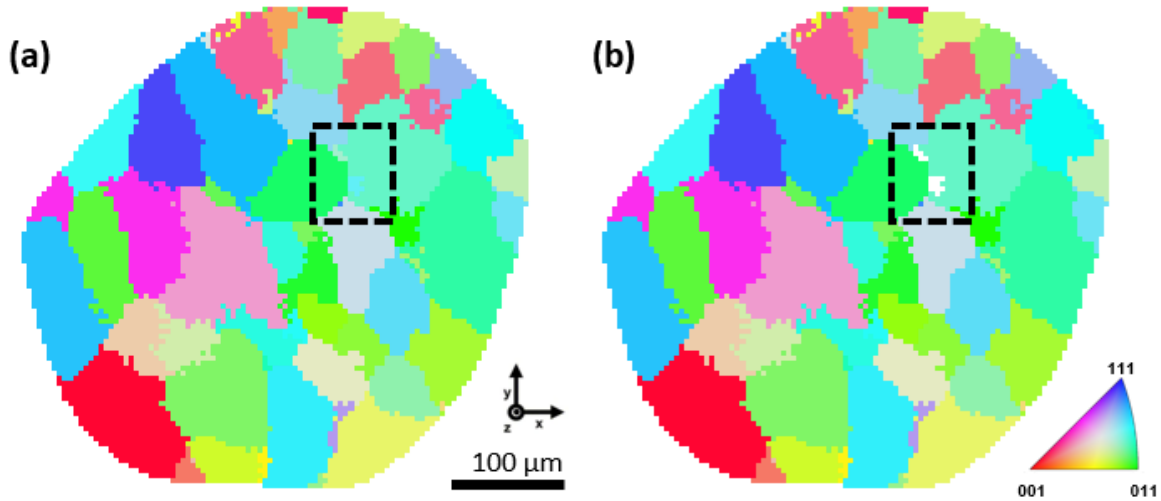

Figure 5.4. Result of data processing with *PolyProc* by comparing (a) before and (b) after the data process shown in 2D. Two grains indicated in the black box from the (a) before processing dataset are considered unreliable and cleaned up in (b) after processing dataset.

Part III. Results and Discussion

Chapter 6. Processing of 3D X-ray Diffraction Data *via PolyProc*

This chapter is based on the article published in *Integrating Materials and Manufacturing Innovation* [80], for which I retain the right to include it in this dissertation, provided it is not published commercially. The co-authors are Ning Lu, Issac Loo, Nancy Senabulya, and Ashwin J. Shahani. This work was supported by the Army Research Office Young Investigator Program under award no. W911NF-18-1-0162 and University of Michigan College of Engineering.

6.1. Introduction

The microstructures of materials, from ceramics to superalloys, are three-dimensional (3D) in nature. Such materials are opaque to most probes, hence they have been traditionally studied by two-dimensional (2D) techniques, *e.g.*, optical or electron microscopy. By coupling the image capture with microstructure sectioning, 3D characterization is possible [36,88–90]. Unfortunately, however, serial sectioning entails the removal of consecutive layers of material to collect 2D images, and so this method is fundamentally destructive. Instead, nondestructive metrologies are needed to detect various microstructural features (*e.g.*, grains and precipitates) and monitor their evolution with a sufficient temporal resolution. For this purpose, X-ray imaging techniques enable the direct visualization of 3D microstructure in a non-destructive manner, since X-rays can penetrate deeply in the materials investigated. Computed tomography (CT) is one of the oldest 3D

imaging [91] techniques that make use of an X-ray beam. As the transmitted X-rays are sensitive to the density of the material, the resulting 3D microstructure shows density differences through the illuminated sample. This is the basis of absorption CT (denoted as ACT). on the other hand, analysis of the *diffracted* X-ray beam is the hallmark of 3D X-ray diffraction (3DXRD) [92–98]. Thus, X-ray microscopes capable of diffraction provide a unique opportunity to characterize poly-crystalline materials in 3D.

Recognizing the promise of 3DXRD, investigators in the past decade have developed a number of different 3DXRD techniques, such as high-energy X-ray diffraction microscopy (HEDM) [95], diffraction contrast tomography (DCT) [94,96,98], and scanning 3DXRD (S3DXRD) [97], to name a few. These techniques are all based on X-ray diffraction, and thus they share common features in terms of their working principle: As a "hard" ($\geqq$ 10 keV) X-ray beam illuminates a specimen, a detector placed behind the sample collects diffraction patterns (spots or streaks) that are generated when grains in the microstructure satisfy the Bragg condition. To track the locations of all grains within the tomographic field-of-view, the specimen is rotated with a small angular increment ($\lesssim 2°$). The diffraction images collected must then be segmented or partitioned into two classes (streak and background). The segmented diffraction streaks are then indexed as grains through a reconstruction procedure, such as the GrainMapper3D algorithm used here. Differences in the 3DXRD techniques stem from the shapes and sizes of incident X-ray beam, chromaticity of source, resolution of detector, and means of reconstruction [99].

Until recently, non-destructive grain mapping *via* 3DXRD was only available at synchrotron facilities with limited accessibility. With the recent development of laboratory-based X-ray diffraction tomography (denoted as LabDCT), bulk polycrystalline specimens can now be readily characterized from one's own laboratory [84,98,100], spearheading a new age in 3D

materials science. Unlike synchrotron-based DCT, LabDCT makes use of a polychromatic, divergent beam, thereby requiring a different reconstruction procedure. A number of studies have already demonstrated the efficacy of LabDCT for the high-throughput characterization of polycrystalline microstructures [87,101–103]. For instance, Keinan *et al.* integrated ACT and LabDCT imaging modalities on a single X-ray microscope to gain new insight on the microstructure of metallurgical-grade polycrystalline silicon, which is simultaneously multi-phase and polycrystalline [87]. McDonald *et al.* conducted 3D space- and time-resolved experiments *via* both LabDCT and ACT to investigate the dynamics of sintering of micrometer-scale Cu particles [102]. While great strides have been made in technique development and applications, a critical need exists to devise the infrastructure for processing such high-dimensional and multimodal datasets.

To this end, a few software packages have been developed to aid in the processing of reconstructed X-ray images. Here we review the strengths and limitations of a few. Tomopy is a Python-based, open-source framework for the reconstruction and analysis of absorption images in particular [104]. As of this writing, the software has not been extended to support 3DXRD data, which is inherently multi-dimensional. That is, 3DXRD provides orientational information (a vector quantity) for each voxel in the imaging domain. At the other extreme is MTEX, a free MATLAB toolbox for analyzing the crystallographic texture from vectorized orientation data outputted from diffraction based techniques such as electron backscatter diffraction [105]. However, MTEX cannot as yet handle the processing of 3D grain maps. In contrast, Dream.3D is a software package that allows for the construction of customized workflows to analyze 3D orientation data, including serial sectioning, DCT, and HEDM [106]. While Dream.3D has demonstrated success in processing 3DXRD data, it has not been optimized for high dimensional

datasets. Thus, the question remains, “How does one 3D microstructure relate to the next in a dynamic experiment?” To answer this question, we present our efforts in developing a data processing pipeline, *PolyProc*, capable of parsing the full spectrum of 2D, 3D, and further higher dimensional data collected through 3DXRD techniques. With our toolbox it is also possible to “layer” one dataset over another, thereby providing a unified description of the underlying microstructure.

6.2. Experimental Methods

We demonstrate the efficacy of our function package with two full-field (volume) scans that are separated by a short time-interval. In this interval, we apply an external stimulus (heat) to encourage the coarsening of grains in the microstructure. We collect the 3D data through the LabDCT module in a laboratory X-ray microscope (Zeiss Xradia 520 Versa) located at the Michigan Center for Materials Characterization at the University of Michigan. We selected an alloy of composition Al–3.5wt%Cu for subsequent analysis, as it is relatively well characterized and does not attenuate the incident X-ray beam too heavily. The sample was prepared for the first round of imaging by annealing at 485 °C, thereby achieving a fully recrystallized state. Of note is that this temperature is below the solvus temperature (about 491 °C), and thus, we retained second phase θ-Al2Cu particles within the system. Annealing also releases the strain accumulated in the cold-rolled condition. From our experience, strain has the effect of smearing the diffraction spots of polycrystals. This, in turn, introduces difficulties in reconstruction, since it becomes impossible to “untangle” the overlapping diffraction spots belonging to individual grains in the microstructure. Following the annealing, the specimen was imaged through LabDCT, collecting 181 projection images every ~ 2° between 0° and 360° with an exposure time of 400 s per projection. The detector images measure 385 μm of the sample from top to bottom. Due to the nondestructive nature of

LabDCT, we further annealed the same sample for four minutes at the aforementioned temperature (485 °C), inducing the microstructural evolution. The second round of imaging was done with the same scan conditions. The specimen was annealed further and imaged in ACT on the same microscope to acquire the spatial distribution of second phase θ-Al_2Cu particles within the tomographic field-of-view. In the ACT scan, we collected 1600 projections evenly distributed between 0° and 180° with an exposure of 5.3 s. The Cu constituent provided a natural source of attenuation contrast such that the θ-Al2Cu particles could be readily identified *via* ACT.

The LabDCT diffraction patterns were segmented and reconstructed *via* the GrainMapper3D™ software developed by Xnovo Technology ApS. In the reconstruction, the volume is overlaid on a structured grid with side length of 5 μm. Based on the known crystal symmetry and lattice parameters, the equations of diffraction are solved for a subset of spots in order to compute a prospective orientation. Then, the forward simulations calculated by the software are compared against the real grains reflection on the detector. A grain is said to be indexed when a match is found between the reflection observed on the detector and predicted position from the forward simulation. **Figure 6.1** shows superposition of the two. The color of calculated diffraction spot represents the crystallographic orientation of grains that give rise to the various spots. Overall, good agreement is seen between the reconstructed and measured results; the simulated patterns are able to capture not only the position of the spots but also their shapes. The software outputs the high-dimensional data in the hierarchical data format version 5 (HDF5), which was designed for complex data objects. Each voxel in the 3D image domain contains the following attributes: its grain identification, Rodrigues vector (texture components), and completeness value. On the other hand, the ACT dataset was directly reconstructed using the filtered back-projection algorithm employed by the Scout and Scan software on the Zeiss Xradia

520 microscope. Our principal task is to process this high-dimensional and heterogeneous data, as will be described in detail below.

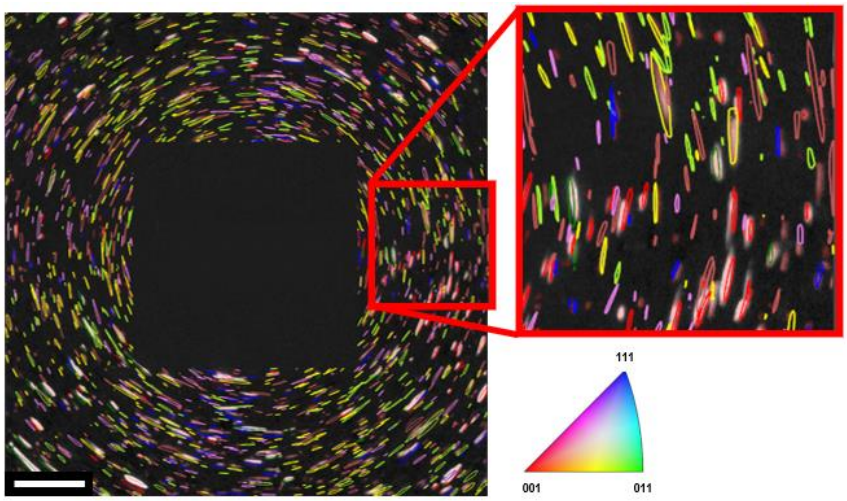

Figure 6.1. Superposition of experimental and calculated diffraction pattern, the latter obtained from forward modelling the reconstruction data. A beam-stop (center) blocked the forward-transmitted beam. Color of calculated spots in the periphery reflects crystallographic orientation of the diffracting grain according to the standard triangle. White scale bar is 1000 μm.

The GrainMapper3D reconstructions are inherently six-dimensional (*i.e.*, 3D space plus 3D orientation). For matrix algebra and plotting, we use the MATLAB R2018a programming language, which provides a high-level technical computing environment. Our toolbox takes advantage of a few different toolkits that are freely distributed through MathWorks, such as MTEX (described above) [105]. MTEX is required to run the pipelines involving data clustering, crystallographic analysis, and grain tracking. Other dependencies are included as utilities within the toolbox.

6.3. Results and Discussion

This section demonstrates integral procedures for processing and analyzing in situ and 3D crystallographic datasets. A typical workflow of the function package is illustrated in **Figure 6.2**, organized in a set of modules that group the algorithms according to their function. In time-dependent studies (like ours), there is likely a misalignment of the scanned domains and/or grain

orientations between consecutive time-steps, causing challenges in data analysis downstream. Thus, after importing the HDF5 data, our workflow starts with the alignment of volume data *via* genetic optimization to define the common scope (intersection volume) for further analysis. Within the defined scope, grain cleanup procedures filter unreliable features such as incorrectly indexed voxels that inevitably appear during data collection. The grains are processed according to three thresholds: angular, volumetric, and completeness. The cleaned data can be visualized in 3D or cross-sectionally in 2D with different color schemes depending on user preference. Data analysis functions provide various capabilities for the statistical analysis of the entire polycrystalline aggregate or a single grain in particular. Additionally, for time-resolved data, our toolbox offers a means of grain tracking *via* combinatorial optimization. We step through each of these modules using the two LabDCT reconstructions as a test case.

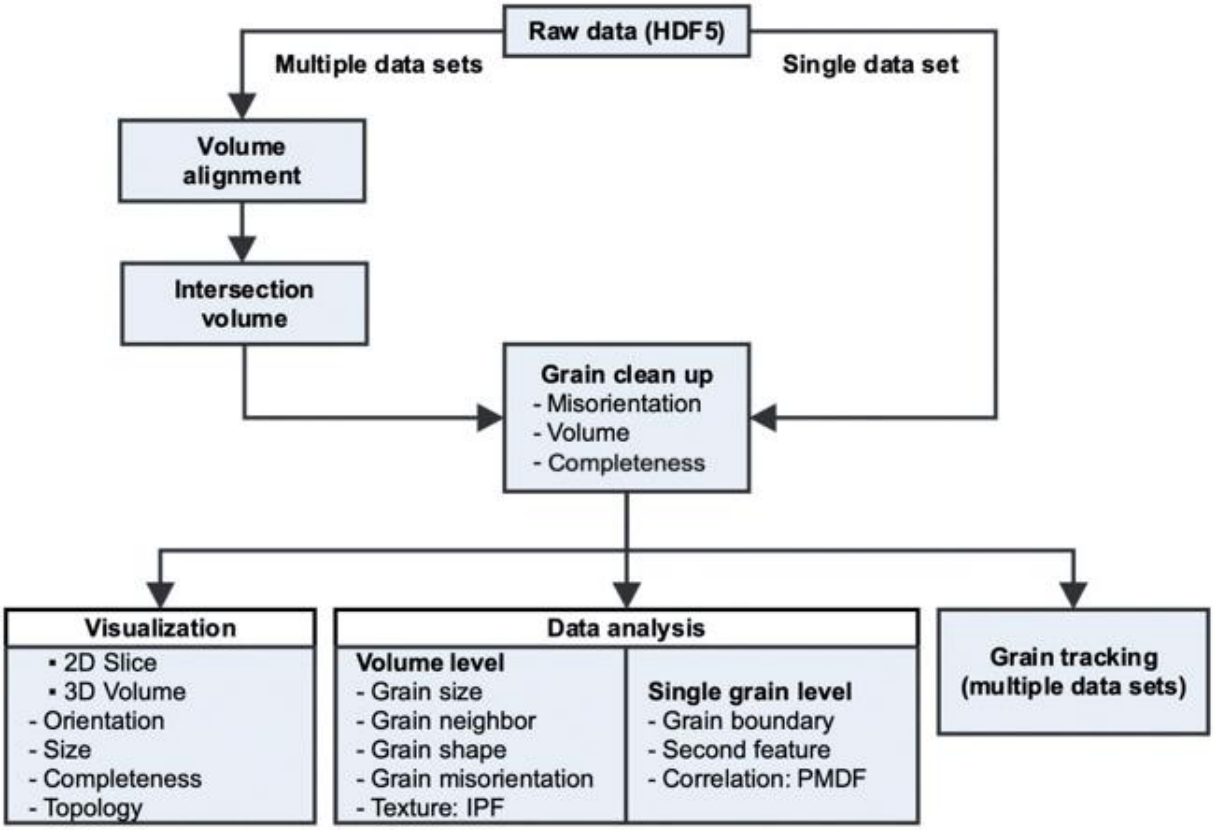

Figure 6.2. Workflow for processing 3D LabDCT data; see text for details.

6.3.1. Data Processing

Volume Alignment

A geometric deviation of sample, including translation and rotation, would be found between two time-steps (denoted t_1 and t_2 hereafter) if the sample was to be repeatedly removed and mounted on its holder. Translation will introduce a spatial drift in corresponding grains between the two datasets. Meanwhile rotation will alter the perceived crystallographic orientation of the grains between time-steps t_1 and t_2. Both transformations will thereby mislead further analysis like grain tracking. Thus, body alignment (registration) of sample volume is the first step of our pipeline.

We solve the registration problem by minimizing the misfit of volume through Genetic

Algorithm (GA). Volume is defined as the set of all pixels within the 3D sample; misfit is the number of voxels not shared between the two volumes t_1 and t_2, over total number of voxels. Six independent parameters are determined during the alignment procedure: three translational vectors (T_x, T_y, T_z) and three rotational angles (R_x, R_y, R_z), assuming a purely isometric transformation. This implies a massive calculation over a 6D space to calculate and compare misfit, if done for all possible transformations. Instead, we achieve a better alignment in a much shorter amount of compute time *via* GA. The detailed operating principle of GA is discussed below. After those six parameters are optimized by GA, a transformation matrix is generated for the alignment of t_2 onto t_1 where t_1 is the reference state. The application of the obtained transformation matrix on scalar data is illustrated in **Figure 6.3a**, where volumes t_1 and t_2 are presented by blue and red color, respectively. Before alignment (top left), a huge misfit is observed. After alignment (top center), not only the outermost contour of sample volume, but also the orientation and location of a pore inside the volume (see arrow), align closely. Subsequently, the shared (intersection) volume is determined (top right), which serves as a "mask" to ensure that all the following comparisons between t_1 and t_2 are carried out under the same region-of-interest.

Based on the Euler rotation matrix described by three rotational angles (R_x, R_y, R_z), the crystallographic orientations of grains are also updated. **Figure 6.3b** shows the registration of grain orientations. Color represents crystallographic orientation parallel to the specimen height (z direction). It can be found that crystallographic orientation of grains becomes similar after updating their Rodrigues vectors. For example, the grains indicated by white arrows are a pair of matching grains. The orientations of those two matched grains are presented by cyan and green color before updating orientations, respectively. Once the Rodrigues vectors are updated, the grain color at t_2 becomes cyan (bottom right), which corresponds closely to the grain at t_1. To quantify

the accuracy of the orientation alignment, we calculated the change of average misorientation of the matching grains between time-steps. As presented in **Figure 6.3c**, before the orientation update, average misorientation angle of the matching grains is 7.56 ± 0.13°; after the update, it decreases to 0.82 ± 0.15°.

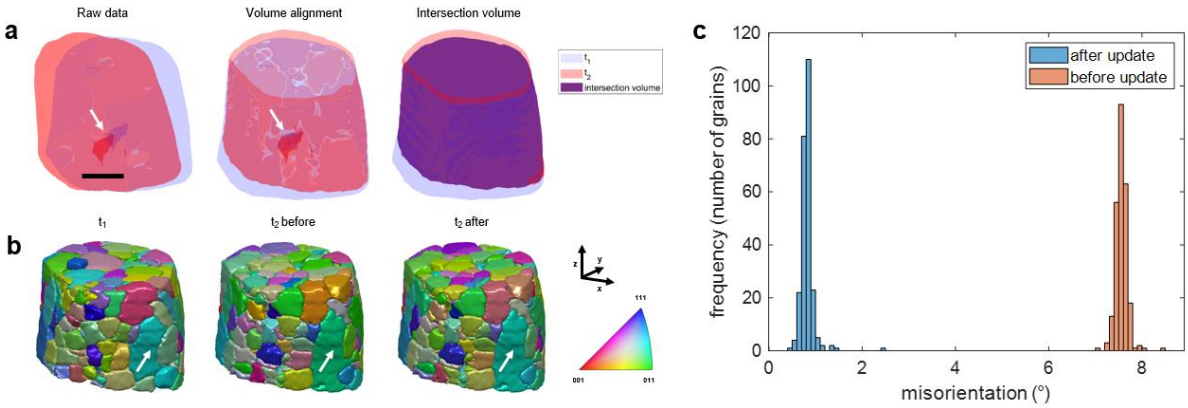

Figure 6.3. Procedures for (a) registering sample volume and defining its intersection; and (b) updating crystallographic orientation of grains based on the rotation angles obtained from volume alignment. Arrows in top and bottom rows point to features that are registered between the datasets t_1 and t_2. Scale-bar measures 100 μm. (c) Quantitative results of crystallographic orientation update based on changes in matching grains.

Since volume alignment is only evaluated by the degree of misfit, it can be formulated as an optimization problem. GA has a few advantages over other optimization engines. For instance, it is generally effective in optimizing a function with many local minima since it does not require a good starting estimate; furthermore, it is quite flexible in that it places no constraint on the form of the objective function [107,108]. Due to these merits, GA has been employed to register 2D and 3D data [108–110]. In this work, GA function from Global Optimization Toolbox of MATLAB is employed [107]. Drawing from Darwin's theory of natural selection, GA begins with a randomly generated set of individuals (rigid transformations in our case) also known as a population at first generation (see **Figure 6.4**). Parallel computation will be utilized to calculate the fitness (here, misfit) between transformed volume at t_2 and volume at t_1. Individuals with relatively lower

misfit would then be selected from the current population, its genome modified and recombined to produce the next generation. We set the maximum number of generations to 25, although this may require some tuning based on the size of the search space. Once the lowest misfit computed lies below the user-specified misfit tolerance during the 25 generations, the algorithm is interrupted in order to output the corresponding six parameters. If the calculated misfit never goes under the threshold, another iteration of GA with 25 generations containing twice the population size is triggered. Larger population size gives more opportunity to reach global minima rather than local minima. Finally, GA outputs the six parameters corresponding to the lowest misfit. As GA is "embarrassingly parallel" and converges to a high-quality solution after only a few generations through a number of bio-inspired operators, the computation time is low, and accuracy of alignment is quite high. In practice, parent selection is done by stochastic universal sampling; mutation *via* gaussian distribution; and crossover through scattered blending. Further details regarding GA can be found in Ref. [107]. In contrast, it is difficult to optimize the accuracy of "brute force" calculations due to the limitation of finite search step size. The accuracy and efficiency were compared on a workstation with Intel(R) Xeon(R) E-2176M CPU core and 64 GB RAM capacity. Between volumes t_1 and t_2, the angular constraints were set to ±7° for each of the three rotational angles (R_x, R_y, R_z) and misfit tolerance of 2%, for both GA and "brute force" comparison approach. The former took 657 s for body alignment with 2.42% of misfit, while the latter took 1175 s with 2.61% misfit. The result indicates that GA can significantly improve the automated registration of 3DXRD data, achieving a better alignment in a much shorter amount of time.

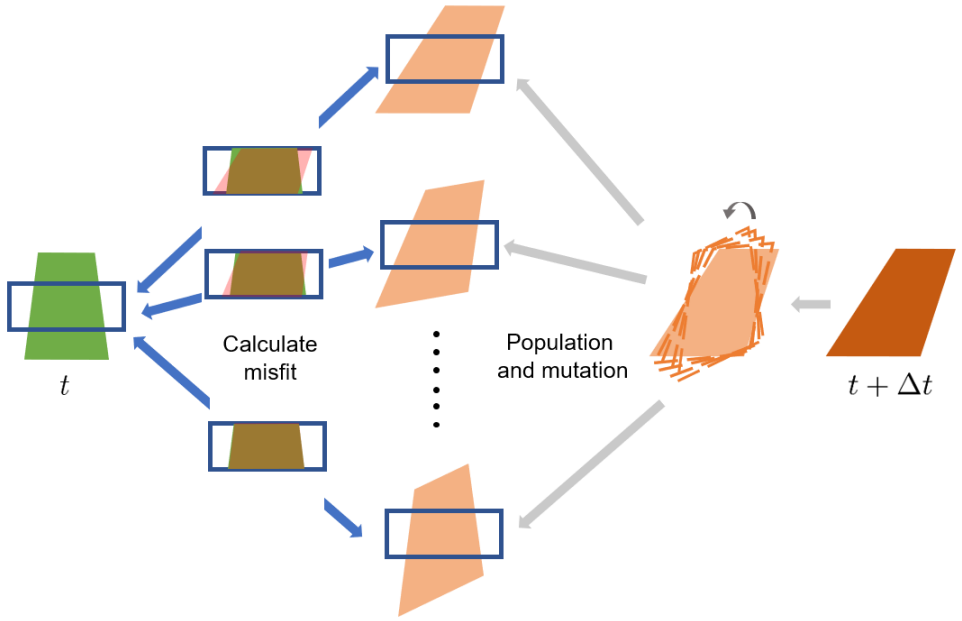

Figure 6.4. Mechanism of automated volume alignment *via* genetic algorithm (GA). Individuals from the later time-step are generated and mutated and their misfit is calculated accordingly. Shown is a single generation of GA. The algorithm proceeds by selecting those individuals with the highest fitness (lowest misfit) for the next generation (not pictured).

Grain Clean Up

The clean-up module aims to align the data based on outputted transformation matrices (from above) and further process them to exclude unreliable features within the intersection volume. Upon importing the raw (*i.e.*, as-collected) 3DXRT data together with alignment matrices and mask array, data outside of masked scope are cropped, and every dimension of data except orientation is transformed to the new frame-of-reference. Since the calculation of crystal orientation is computationally costly — there are $\mathrm{O}(N^3)$ rotations that need to be performed, assuming a mask dimension of N — the Rodrigues vectors are updated only after the average orientation of grain is computed based on clustering voxels with similar orientation. That is, based on a user-defined angular threshold (typically $\leq 1°$), grains with very small misorientation angles are grouped into a single grain. This order of operations greatly reduces computation load without compromising the accuracy of orientational alignments.

After clustering grains and updating the average grain orientations, data is further processed to remove small grains. Any grain composed of fewer voxels than a preset volume threshold is considered as noise and treated as unindexed regions. The rationale behind this procedure is to retain statistically significant grains and not to artificially inflate grain statistics. The volume threshold is determined based on the spatial resolution of the reconstruction data (10 μm for LabDCT). Finally, grains with lower average completeness than a preset completeness threshold are considered as unreliable data and marked as unindexed. Low completeness grains are often located near the edges of the LabDCT aperture, wherein grains may lie partially outside of the illuminated field-of-view. Consequently, their diffraction patterns are partially occluded by the aperture, resulting in a low reconstruction completeness in Forward modeling simulations.

Outputs of this module include basic measurements of the processed grains: grain volume is expressed as total number of voxels; grain orientation as the average Rodrigues vector over all voxels in each grain; grain position as its center-of-volume, considering the Euclidean coordinates of every voxel in the grain. Grain adjacency is also stored in a form of a M by 2 array of neighboring pairs that meet at a grain boundary, where M is the number of unique pairs. Those grains adjacent to the free surfaces of the sample are designated as "exterior" grains and those in the bulk as "interior."

6.3.2. Visualization

The segmented grain surfaces are meshed or represented as a series of triangles and vertices. Triangulation is accomplished *via* MATLAB's built-in Marching Cubes routine. To eliminate any "staircasing" artifacts that occur as a result of the triangulation, we smooth the mesh to better reflect the physical grain shape. In particular, we make use of Laplacian smoothing, which utilizes the normalized curvature operator as weights for smoothing in a direction normal to the mesh

interface. In practice, we apply only a few iterations of mesh smoothing in order to reduce artefacts while preserving the integrity of interface.

Different modes for mesh coloring are available based on user preference. For instance, the grains can be colored according to their crystallographic orientation, topology (*i.e.*, number of grain neighbors), volume, and average completeness. **Figure 6.5** illustrates these different representations of the t_1 volume. It should be noted that average completeness value of many grains is close to 0.45 because reconstruction of this particular dataset was executed with a tolerance level of 0.45, meaning that indexing voxels concluded once a completeness value of 0.45 was achieved. Grains located on the topmost surface of the sample show a lower completeness compared to ones located below because those grains partially lie out of the illuminated field-of-view. The bottom surface of the sample is not shown because it is outside the intersection mask between volumes t_1 and t_2 (see also **Figure 6.3a**). Visualization of individual 2D slices along the specimen z direction is also available under the same color schemes, thereby demonstrating the versatility of our function package in handling different data shapes.

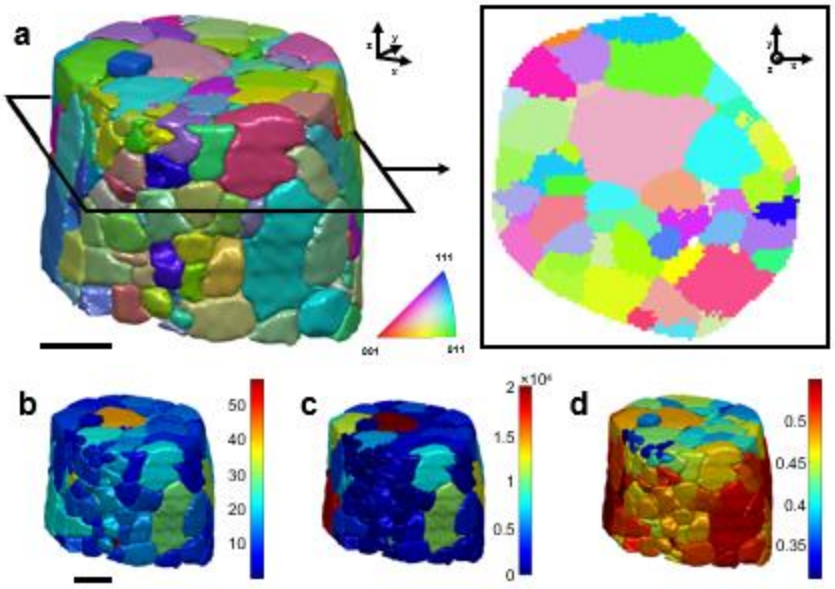

Figure 6.5. Visualization of 3DXRD data in 2D and 3D. Grain color corresponds to (a) crystallographic orientation, (b) number of neighboring grains, (c) grain volume, (d) average completeness of grain. Scale-bar measures 100 μm.

6.3.3. Data Analysis

Simple Metrics

Direct imaging of 3D microstructure allows for the characterization of various indicators of microstructure evolution, including grain size, shape, and topology. These metrics can only be estimated *via* quantitative stereology of planar sections [111]. To our benefit, these parameters can be measured directly from 3DXRD without any averaging or interpolation. In the analysis module, we provide some basic statistics at the grain level. These include

- *Grain volume*, see, *e.g.*, **Figure 6.6a** corresponding to t_1 volume. A wide range of grain sizes is captured in the grain size distribution, from 33 voxels (4.3×10^3 μm^3) to 20,298 voxels (2.5×10^6).
- *Grain topology*, **Figure 6.6b**. An accurate assessment of topology is limited by the finite sample size [112], meaning that the number of neighbors for the "exterior" grains may be

underestimated compared to those in the specimen "interior". To resolve this potential bias, we distinguish between topologies of "interior" versus "exterior" grains.

- *Grain morphology*, **Figure 6.6c**. Sphericity (Ψ) is defined as a ratio of surface area of a sphere having the same volume of a grain to the actual surface area of a grain; that is $\Psi = \frac{\pi^{\frac{1}{3}}(6V_g)^{\frac{2}{3}}}{A_g}$, where where V_g is volume of a grain and A_g is surface area of a grain. The former is outputted from above while the latter is determined as the summation of each triangle area adorning the grain surfaces, $A_g = \sum_{i=1}^{F} A_{tri}^{i}$, where A_{tri}^{i} is the area of triangle i and F is the total number of triangle faces. The area of each triangle is computed as $A_{tri}^{i} = \frac{1}{2}\left\|\vec{e}_{12}^{i} \times \vec{e}_{13}^{i}\right\|$ where $\vec{e}_{jk}^{i}$ is the edge vector from vertex j to k of triangle i. The vast majority of grains at the time-step t_1 show a relatively high compactness ($\Psi \to 1$), which is expected for a recrystallized system.
- *Grain misorientation*, **Figure 6.6d**. Misorientation Δg is formally defined as $\Delta g = g_i g_j^T$ where g_i and g_j are the grain-average orientations (in Rodrigues vectors) determined from the *clean up* module above. The histogram weights in the misorientation distribution are the grain boundary areas, found by summing over all triangle areas along the boundary. We show for comparison the distribution expected for a material with uniformly distributed misorientations. The results for the t_1 data indicate a near-random distribution of grain boundaries.
- *Grain texture*, **Figure 6.6e**. Shown is the inverse pole figure (IPF) of all grains in the t_1 volume. It can be seen that the sample has no obvious texture at this particular time-step.

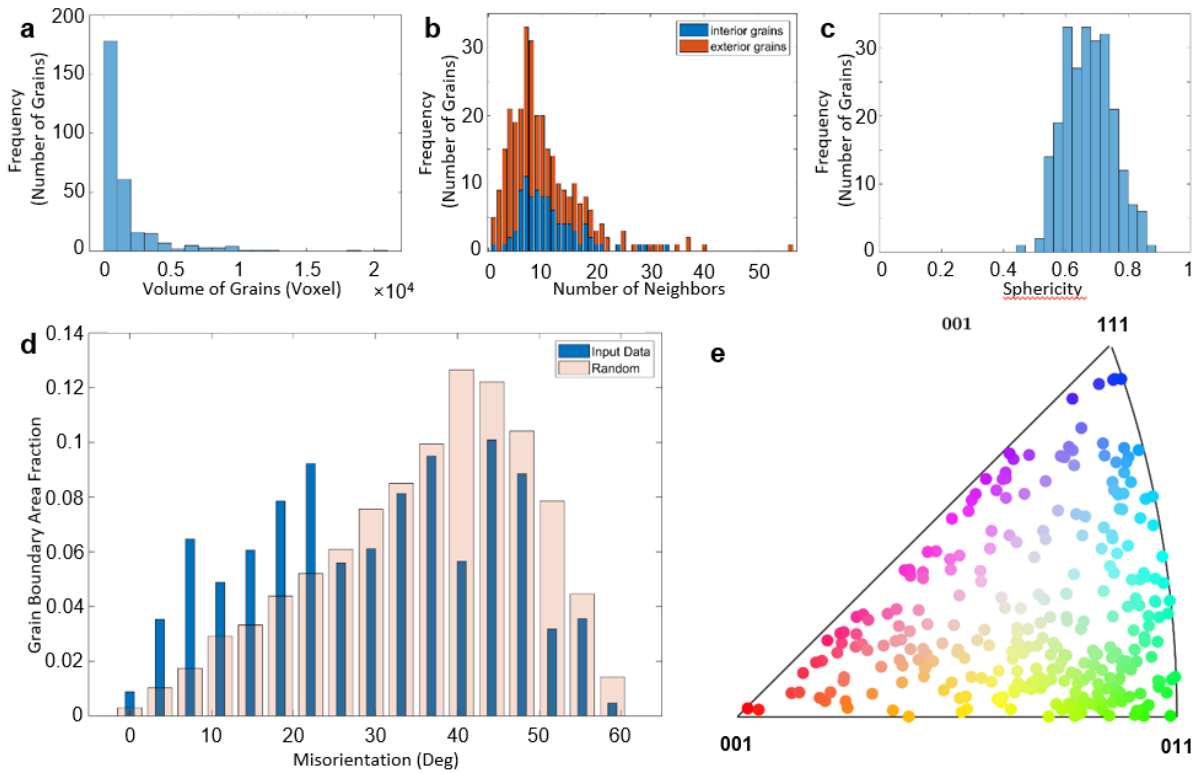

Figure 6.6. Analysis of 267 grains in the microstructure. (a) Grain size distribution, (b) neighbors distribution, (c) sphericity distribution, (d) misorientation distribution (*i.e.*, Mackenzie plot), and (e) inverse pole figure where colors are drawn from the standard triangle. Shown in (d) for comparison is the distribution expected for a material with uniformly distributed misorientations.

Multimodal Analysis

The integration of multiple imaging modalities enables us to investigate correlations between various features, thereby providing an in-depth understanding of the underlying microstructure. For instance, in the *multimodal analysis* module, we correlate the positions of grain boundaries (retrieved *via* LabDCT) to that of secondary features (observed *via* ACT). The ACT data is assumed to be registered to the LabDCT data through application of the functions in the *alignment* module. The secondary features are (in our case) micrometer-scale θ-Al_2Cu particles whose locations in the microstructure are given in form of centroid coordinates. The user may specify a grain-of-interest (GOI) and a distance threshold to then determine which particles in the particle cloud are adjacent to the GOI, and the corresponding grain-to-particle distances. We

visualize the particles within a two-voxel distance threshold in **Figure 6.7a**. To link grain boundaries to secondary features, we have developed a new algorithm, summarized here as follows: (1) for each triangle face along the grain boundaries, we calculate its centroid; next (2) we find the nearest-neighbor distances between the face centroid and particle locations; and (3) if this distance is less than the threshold, we conclude that the particle lies on or sufficiently close to the triangle face. Step (2) above can be accomplished by calculating the Euclidean distance between each particle and each mesh triangle and then organizing the results in ascending order of distance. This approach would necessitate $N \times M$ calculations to correlate particle and grain boundary positions, where N is the number of particles and M the number of mesh triangles that enclose a given grain. Considering that M is on the order of 10^5, and N is also 10^5 (this work), the task of particle classification (as near or far from the boundary) is computationally intensive if done in such an exhaustive manner. To recognize patterns in the locations of particles with respect to grain boundaries, we harness the k nearest neighbors (k-NN) algorithm, a type of "lazy" learning. k-NN lessens the computational load significantly — determining the nearest-neighbor particles in seconds — by using a so-called Kd-tree to narrow the search space. This algorithm was previously implemented in measuring the local velocities of solid-liquid interfaces in dynamic, synchrotron-based CT experiments [113].

Provided that the grain misorientations are known (**Fig. 6.7b**), we can measure the particle associated misorientation distribution (PMDF), among other interrelationships [114]. The PMDF is defined as the fraction of secondary features (here, particles) that are located on or in the vicinity of grain boundaries within a specific range of misorientation angles. It can be seen in **Figure 6.7c** that the distribution of particles does not follow the distribution of grain boundaries, which might be expected if the particle-boundary correlations were truly random (*i.e.*, density of particles per

unit area of boundary is constant).

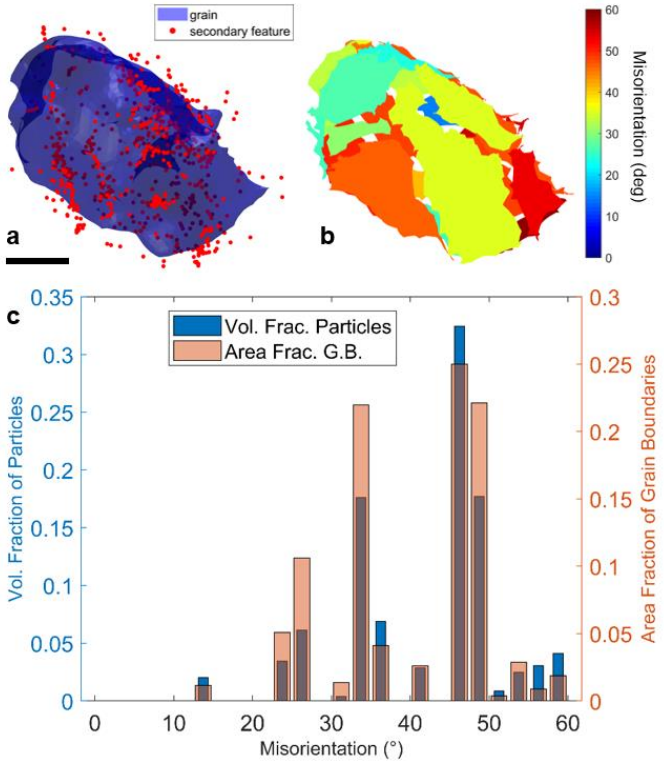

Figure 6.7. Analysis of a single grain according to its (a) adjacency to secondary features (here, θ-Al_2Cu precipitates in red), and (b) misorientation with adjacent grains. Only those particles within two voxels of the grain boundary surfaces are shown. The one voxel "gap" between two given grain faces in (b) arises due to the uncertainty of classifying that voxel to a given face. Scale bar measures 50 μm. (c) Particle-associated misorientation distribution of the same grain. Volume fraction of particles adjacent to grain boundaries is shown in blue, and Mackenzie plot is shown in orange.

6.3.4. Grain Tracking

In this module, we define a mapping between experimental time-steps, allowing for the analysis of individual grains as time progresses. We use two key parameters for grain tracking: crystallographic misorientation and physical distance. The crystallographic orientation of a given grain should not change over time, provided the sample is fully recrystallized, and its location within the microstructure should also not change too drastically. **Figure 6.8** illustrates our approach for grain tracking. Under the above two constraints, we search for a matching grain at

some time-step in the future ($t + \Delta t$) within a local neighborhood of the grain at the current time-step t. The neighborhood is defined as smallest cuboid that encapsulates a grain with a user-defined additional padding (in number of voxels). Any grain included in the cuboidal scope is considered to be within a local neighborhood. For instance, the gray colored region in **Figure 6.8** illustrates the cuboidal scope of grain m with default padding of two voxels. Care must be taken in defining the size of the grain neighborhood since too large a padding may lead to an incorrect grain assignment and too small an extension may fail to contain the matching grain. Any grain that is partially contained in this cuboidal scope at time-step $t + \Delta t$ is labeled as a candidate grain.

For each candidate grain in the neighborhood, we tabulate its distance and misorientation. Distance Δd_{nm} refers to that between the centroid of grain m and centroid of candidate grain n. The maximum (threshold) distance is predetermined as the half-diagonal length of cuboidal neighborhood. Similarly, misorientation angle $\Delta\theta_{nm}$ is that between grain m at time-step t and grain n at time-step $t + \Delta t$. The maximum allowable misorientation (threshold) is a user-defined value. In theory, the misorientation between two datasets should be zero if the sample is perfectly registered and there are no grain rotations. Yet this is often not the case due to slight misalignments between datasets (see **Data Processing**). These two metrics are combined linearly to formulate a cost function J_{nm} associated with the assignment of grain n to grain m,

$$J_{nm} = c\,\Delta d_{nm} + (1 - c)\Delta\theta_{nm} \qquad \textbf{(Equation 6.1)}$$

, where c is a scalar quantity (ranging from zero to one) that reflects the importance of the distance over misorientation criterion. Rohrer uses a similar formulation of the cost function [115]. The problem of grain tracking is then to find the lowest cost way of assigning grains from one time-step to the next. To solve this assignment problem in polynomial time, we employ the Hungarian algorithm (otherwise known as the Kuhn-Munkres algorithm) [116,117]. The algorithm operates

on a cost matrix $\boldsymbol{J} = \{J_{nm}\}_{N\times M}$, and outputs a binary matrix $\boldsymbol{X} = \{x_{\mathrm{nm}}\}_{\mathrm{N\times M}}$ where $x_{nm} = 1$ if and only if the n-th grain at t is assigned to the m-th grain at $t + \Delta t$. The total cost is then found as $\sum_{i=1}^{N}\sum_{j=1}^{M} x_{\mathrm{nm}} J_{nm} \rightarrow \min$. Unlike the typical assignment problem with a square cost matrix (*i.e.*, the matrix dimensions are such that $N = M$), our cost matrix is rectangular ($N < M$) since the total number of grains decreases with time over the course of grain growth. However, the algorithm can be extended to rectangular arrays using the method prescribed by Ref. [117], which we have applied here. Worth mentioning is that the cost element J_{nm} for a non-candidate grain is computed to infinity, preventing the assignment of disappearing grains. Elements for candidate grains are normalized by threshold values to bring orientation and distance parameters into the same scale.

The result of grain tracking *via* Hungarian algorithm approach is evaluated using two performance metrics, matching efficiency and computation time. Matching efficiency represents the percentage of grains that are successfully tracked (assigned), *i.e.*,

$$\text{matching efficiency } (\%) = \frac{\text{number of matched grains at later time step}}{\text{number of total grains at later time step}} \times 100 \qquad \textbf{(Equation 6.2)}$$

Grain tracking between the two LabDCT datasets achieved a ~86% matching efficiency. The remaining ~14% of grains that were not assigned can be mainly attributed to grains that emerged into the tomographic field-of-view. Since the rod specimen is long enough to be considered an open system, "new" grains that were not captured in previous time step may be detected near the top and bottom of the X-ray source aperture. This can be confirmed from **Figure 6.3b** that top layer of $t_2$volume has several new grains that are not observed in previous $t_1$volume.

Hungarian optimization offers distinct advantages over the "brute force" solution to the assignment problem. The latter considers every possible assignment, implying a complexity of $\mathrm{O}(N!)$. To speed up the task at hand, we may elect to iteratively (i) locate a grain neighborhood, (ii) compute costs J_{nm} of all grains in the neighborhood, and (iii) assign matching grains based on

minimum cost; once a matching grain is found we proceed to the next grain in the dataset. However, rather than computing cost matrices $\boldsymbol{J}$ and analyzing the matching problem in a comprehensive manner, this approach sequentially assigns matching grain as it goes through the N grains, causing an inherent bias from the matching order. It is for this reason that the Hungarian algorithm offers a higher matching accuracy and computational efficiency over these brute force methods. On a same workstation with Intel(R) Xeon(R) E-2176M CPU core and 64 GB RAM, grain tracking between datasets with $M = 308$ and $N = 295$ grains *via* Hungarian optimization takes 11.44 seconds with a cuboidal scope padding of two voxels, misorientation threshold of four degrees, and weight factor c of zero. On the other hand, the three-step iterative matching scheme described above takes 15.69 seconds with the same parameters and offers a matching rate of ~85%. Even though the matching efficiency of both methods are comparable, tracking by brute force results a few cases of incorrect assignments for the reasons mentioned above. Even larger data sizes (*e.g.*, fine-grained materials) should widen the performance gap between combinatorial optimization and "brute force" approaches.

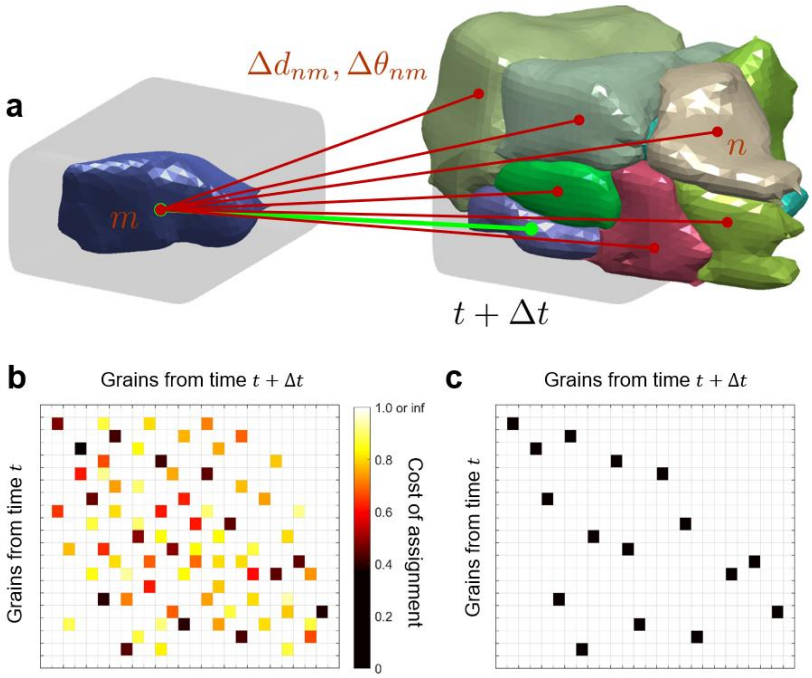

Figure 6.8. (a) Mechanism of grain tracking. For the candidate grains n in the neighborhood of grain m, physical distances Δd_{nm} and misorientation angles $\Delta\theta_{nm}$ are computed. These parameters are combined linearly to give the cost of assignment according to **Eq. 1**. The green line represents the matching grain among other candidate grains (red lines). (b) Schematic of cost matrix $\boldsymbol{J}$, where row and column entries represent grains from time step t and $t + \Delta t$, respectively. Colored entries in each row represent candidate grains at $t + \Delta t$; color scheme indicates cost of assignment. (c) Output binary matrix, $\boldsymbol{X}$, where row and column entries represent grains from time step t and $t + \Delta t$ (as before). Black colored entries are optimized assignments.

6.4. Summary

With the concomitant rise and accessibility of 3D characterization approaches there is an emerging need for processing the multimodal and multidimensional data outputted from such techniques. To this end, we have developed a set of functions to import, process, and analyze 3DXRD datasets of varying dimensions, from 2D to higher dimensions. Through effective computational routines, the toolbox allows us to align and track features in a highly accurate, efficient, and robust manner. For instance, we have achieved a 45% decrease in computation time by registering data *via* Genetic optimization. Similarly, we attained an 86% matching rate between grains in consecutive time-steps, whereas brute force solution to the assignment problem achieved

a similar matching efficiency in 37% longer time. Our package also includes functions to filter out unreliable features of the experimental data, perform basic statistics on the "cleaned" data, and visualize the resultant microstructures. We also offer a solution to correlate and fuse the results from different imaging modalities and/or instruments, *e.g.*, ACT and LabDCT. The full breadth of our toolbox is tested on two datasets of a bulk metallic specimen undergoing grain growth, yet the toolbox is capable of processing a stream of multiple data sets. It is also noteworthy that the toolbox is not strictly limited to metals nor coarsening phenomena, as showcased here. Rather, we expect that our function package will provide a cross-cutting foundation for data processing involving very minimal sample-specific tuning. Potential test cases include studies of crack propagation in polycrystalline materials, embrittlement of grain boundaries, and defects in additively manufactured polycrystals.

Our function package is available as a free and open source MATLAB toolbox and may be downloaded from repository platforms, such as Github (https://github.com/shahaniRG/PolyProc) and MATLAB File Exchange (https://www.mathworks.com/matlabcentral/fileexchange/71829-polyproc). It is open to any party wishing to not only use the codes but also contribute to its vitality.

Chapter 7. Formation and Persistence Mechanism of 'Abnormal' Grains

This chapter is based on the article published in *Acta Materialia* [81], for which I retain the right to include it in this dissertation, provided it is not published commercially. The co-authors are Ning Lu, Nancy Senabulya, Ron Keinan, Nicolas Gueninchault, and Ashwin J Shahani. This work was supported by the Army Research Office Young Investigator Program under award no. W911NF-18-1-0162 and University of Michigan College of Engineering.

7.1. Introduction

In structural materials, grain refinement is an attractive mechanism for optimizing material properties because grain boundaries (GBs) act as barriers for dislocation motion. To this end, second phase particles — which exert drag or pinning pressure [44]— may restrain grain boundary migration in polycrystalline materials. For this reason, the evolution of grain structure in particle-containing systems has been an active area of research, from the 1940s to present day [44,118–124]. Even so, the evolution of the grain network in the presence of particles is far from understood, with a number of competing proposals (*vide infra*). For example, prediction of pinned grain size by Smith–Zener equation generally overestimates, and a number of modifications exist [45].

In general, there are two ways in which grains evolve during coarsening: normal grain growth (NGG) and abnormal grain growth (AGG). In NGG, the grain size follows a normal distribution after primary recrystallization [29,125]. On the other hand, AGG is a discontinuous grain growth event, wherein a few grains "run away" from the normal distribution and grow at much faster rate by consuming other grains. The preferential growth of a few grains in AGG may

be triggered by energetic factors (such as stored strain energy [126–128]) or kinetic factors (such as high mobility grain boundaries [129,130]). Beyond such *intrinsic* reasons for AGG, one must also consider a grain's *external* environment: AGG may occur in a polycrystalline material with a dispersion of second-phase particles [49,131–133] For example, Dennis *et al.* [49] observed AGG following primary recrystallization in Al-3.5wt%Cu alloys, which consist of θ-Al_2Cu particles in an Al matrix. Upon annealing at 485 °C, which is below the solvus temperature of 491 °C, the authors observed a few colossal (200 μm) grains that grew much faster than the others. Since only a weak crystallographic texture was measured in Al-3.5wt%Cu, grain orientation alone cannot explain why AGG occurred.

Our traditional understanding of AGG in the presence of particles is that the particles begin dissolving close to the solvus temperature [134,135]. Due to the smaller particle sizes, the pinning pressure acting on the grain boundaries is reduced and hence the grain boundaries can break free. However, contrary to this metallurgical intuition, simulations show that AGG can indeed occur in pinned microstructures without any such particle dissolution. According to recent work done by Holm *et al*. [133], a few grains can thermally fluctuate from their particle clouds at long incubation times. If the free grain boundaries belong to a grain that is inclined to grow, growth will be sustained since the boundaries of the neighboring grains remain immobile [136]. This counterintuitive result — in which the abnormal grains are much larger than the Zener prediction [44,45] — is termed "particle-assisted abnormal grain growth". It is important to keep in mind that Holm *et al.* assumed that the particle distribution and grain boundary properties are uniform and isotropic. It is unlikely that these assumptions hold true for real materials.

In general, grain growth in a particle-containing system is a delicate balance between the capillary driving pressure, P_d, and the particle pinning pressure, P_z, which can be combined to

yield the volumetric grain growth rate $\Delta V/\Delta t = M(P_d - P_z)$, where M is the grain boundary mobility and t is time. When $P_d = P_z$, the two pressures are equal and opposite, and the grain has reached its limiting size. It can be shown that $P_d \propto \gamma F V^{1/3}$ [137] and $P_Z \propto \gamma n_p$ [44], where γ is the grain boundary energy, F is the number of grain neighbors, $V^{1/3}$ is an integral measure of grain size, and n_p is the number of particles around the grain. Analytical [29,52,138] , computational [42,134,139,140] , and experimental [49,129,131,132] studies demonstrate that grain orientation (texture [129,130]) and grain size advantage [29]contribute significantly to grain growth through the parameters $M\gamma$ and $FV^{1/3}$, respectively. In particular, the influence of grain size on the propagation of abnormal grains has been assessed through "mean field" models [141] which assume a mean matrix (normal) grain size and a uniform distribution of particles [140,141]. Based on such models, a critical size to sustain abnormal grain growth was analytically determined to be about 1.4 times that of the mean grain size. However, these models were not cross-checked on experimental results, likely due to the dearth of 3D and time-resolved information of microstructure evolution.

Indispensable from theoretical advances are new modes of real-time and three-dimensional (3D) characterization, which are required to capture the full microstructural details. For example, laboratory-based 4D X-ray diffraction-contract tomography (LabDCT) has only recently been applied to the study of microstructural evolution [102,103]. Here, we take advantage of new strides in laboratory-based X-ray microscopy, integrating diffraction-contract tomography (LabDCT) and absorption-contrast tomography (ACT) to reveal the interaction between grain boundaries and particles, respectively, in all their complexity. Correlative imaging in the laboratory has opened a new paradigm in physical metallurgy [142,143] and allows us to test the above theories of AGG with great precision. Through this multimodal imaging platform, we characterize the grain

structure evolution and particle distribution in an Al-3.5wt%Cu alloy as a model system. We observe AGG after prolonged annealing *via* LabDCT. Meanwhile, the particle distribution is highly non-uniform, as determined *via* ACT. By combining results from LabDCT and ACT, we find abnormally large grains located in regions with low particle density. That is, a non-uniform distribution of particles can trigger AGG even in initially normal grain structures, for reasons that will be presented and discussed.

7.2. Experimental Methods

7.2.1. Sample Preparation

An ingot of composition Al-3.5wt%Cu was cast *via* vacuum arc melting at the Materials Preparation Center at Ames Laboratory (Ames, IA, USA), using high-purity Al (99.999%) and Cu (99.997%). This sample was selected because its thermo-physical properties are well known and also it does not attenuate the incident X-radiation too heavily. Our subsequent processing steps are based loosely on the prior work of Dennis and Humphreys [49]. That is, the ingot was initially homogenized at 550 °C for 4 hours. Then, it was annealed at 400 °C for 30 min. after 50 % thickness reduction by cold rolling. These treatments lead to a strain-free (*i.e.*, fully recrystallized) microstructure as determined by the diffraction patterns in LabDCT [80]. The annealed sample was machined *via* electric discharge machining (EDM) and further electro-polished in nitric acid-based electrolyte (HNO_3:CH_3OH = 1:2) at −20°C to obtain a thin pillar geometry (~500 μm dia.) for the subsequent X-ray tomographic imaging in the laboratory.

7.2.2. Data Acquisition

The prepared sample was imaged through LabDCT and ACT on a laboratory X-ray microscope (Zeiss Xradia 520 Versa) at the Michigan Center for Materials Characterization at the University of Michigan. The anneal schedule is shown in **Figure 7.1a**. In short, we imaged the

grain evolution in an interrupted manner: that is, the same pillar sample was isothermally annealed at 485 °C and then water-quenched after 0, 22, 42, 67, and 97 min. Of note is that this anneal temperature is below the solvus temperature (491 °C), thereby retaining second-phase θ-Al_2Cu particles in the system. After each of the anneal segments, we conducted a LabDCT scan. LabDCT enabled us to measure the grain structure, including the grain size, shape, orientation, and position. In recent years, the technique has been validated against synchrotron DCT [100] , EBSD, and absorption-contrast tomography [144] all with satisfactory results for grains that are larger than ~20 μm (as in this work). During each LabDCT scan, the detector imaged 385 μm of the pillar sample from top-to-bottom for 0, 22, 42 min. anneal states, and a vertical scope of 1025 μm for the 67, 97 min. anneal states. We increased the field-of-view (FOV) midway through our experiment in order to capture more grains, as the average grain size increased upon annealing. For each tomogram, we collected 181 projection images every ~2° between 0° and 360° with an exposure time of 400 s per projection.

On the same instrument we have access to a second imaging modality, ACT, which we used to characterize the location of second-phase particles in 3D space. Here, the Cu constituent in the θ-Al_2Cu particles provided a natural source of absorption contrast (Cu is heavier than Al). Unfortunately, at a temperature of 485 °C, the observation of particles *via* ACT was hindered by a limited volume fraction of the θ-Al_2Cu phase (~0.3%). In order to observe particles more clearly, we took the following steps at the very end of our experiment (*i.e.*, after 97 min. mark, see **Figure 7.1a**): we ramped down the temperature from 485 °C to 450 °C at a rate of 0.6 °C/min. and held the sample at 450 °C for an additional 30 min., thereby increasing the volume fraction of the θ-Al_2Cu and hence magnifying the particle size (for sake of imaging only). Calculations in TC-PRISMA demonstrate that the particle diameter increased from about 0.4 to 0.7 μm

(**Figure 7.1b**) within this temperature window, thereby allowing us to detect particles against a matrix with higher signal to noise in ACT. The annealed sample with larger particles was imaged in ACT using 1600 projections evenly distributed between 0° and 180° with an exposure of 5.3 s.

This ACT scan was intended to represent the particle distribution of the system throughout the entire anneal schedule. To this end, our calculations (**Figure 7.1c**) revealed that the number of particles does not vary significantly as the temperature is lowered, owing to a very large nucleation barrier above 445 °C. This indicates that this final ramp down in temperature had no discernable effect on the nucleation of *new* particles. That is, the increase in volume fraction between 485 °C and 450 °C was accomplished by growth on *pre-existing* particles. One may also wonder about the coarsening rate of the particles at elevated temperature. We note that particle coarsening should be very slow during isothermal annealing at 485 °C (as it involves long-range transport) and thus only the smallest particles should dissolve into the matrix (due to their higher mean curvatures). Conversely, it is reasonable to expect that that the larger particles that exert the most significant pinning pressures [44] prevail in the sample. Detailed validation of our assumption is provided in the following.

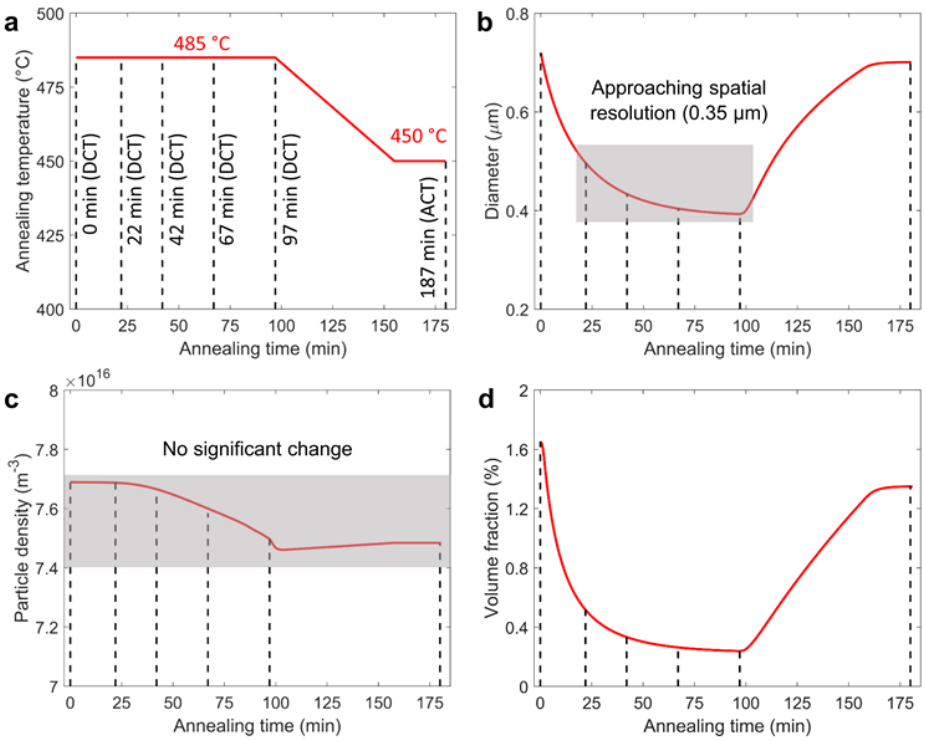

Figure 7.1. Thermodynamic predictions *via* TC-PRISMA of θ-Al_2Cu particle evolution in the Al-3.5wt%Cu system over the course of annealing. (a) Overview of annealing schedule. Variation of (b) particle size (diameter), (c) density, and (d) volume fraction during the annealing process shown in (a). Initial mean grain size was set to 0.7 μm in calculations.

Quantitative Predictions on Particle Behavior

During prolonged annealing at 485 °C, the particles may evolve through coarsening, dissolution, and morphological instability. Yet we believe that these three factors do not significantly influence our analysis of the interaction between particles and grain boundaries.

Firstly, the coarsening rate is too low. We calculated the coarsening rate of θ-Al_2Cu particles at 485 °C based on Lifshitz-Slyozov-Wagner theory [30]. During isothermal and steady-state ripening of a two-phase alloy, the average particle size R evolves with time t according to [2]

$$R^3 - R_0^3 = \frac{8\tilde{D}\gamma\Omega c_{(\infty)}^{eq}}{9kT}t \qquad \textbf{(Equation 7.1)}$$

where $\widetilde{D} = 9 \times 10^{-11}\ m^2/h$ is the bulk diffusion coefficient of component B (Cu) in α phase (Al matrix) [145], $\gamma = 0.456\ J/m^2$ is the interfacial energy between α (Al matrix) and β phase (θ-Al_2Cu) [145], $\Omega = 1.6 \times 10^{-31}\ m^3$ is the atomic volume, $c_{(\infty)}^{eq} = 0.015$ is the solubility B (Cu) in α (Al matrix) for a system with a planar α/β interface, k is the Boltzmann constant, and $T = 758$ K (485 °C) is the annealing temperature.

Based on calculations in TC-PRISMA (**Figure 7.1b**), the mean particle size R_0 is about 0.2 ~ 0.35 µm, after Al and Al_2Cu have achieved their equilibrium volume fractions at 485 °C. Then, using **Equation 7.1**, the maximum particle coarsening ratio $(R - R_0)/R_0$ after $t = 1\ h$ of annealing is determined to be 3.5% when $R_0 = 0.2$µm, *i.e.*, the maximum particle size variation $(R - R_0)$ is about 0.007 µm. Since this value is much smaller than the particle size, isothermal coarsening could be safely neglected.

Secondly, morphological instabilities will not significantly change the centroid position of the particles. The surviving particles may indeed evolve *via* Rayleigh instabilities [146], yet the magnitude of such perturbations is on the order of the particle size. According to calculations (**Figure 7.1b**), the particle size (diameter) is below 1 µm at 485 °C. Importantly, this length-scale is well below the threshold of 15 µm used to identify the local particle density in the vicinity of an individual grain boundary. Thus, slight variations in centroid position on the order of 1 µm will not impact our analysis. For these reasons, our terminal ACT scan can approximately deliver the distribution of second-phase particles throughout the annealing steps.

7.2.3. Data Processing

Reconstruction of LabDCT data was done *via* the GrainMapper 3D™ software developed by Xnovo Technology ApS. Further details are given in Refs.[80,87]. The reconstructed data from Grain Mapper 3D™ was then imported and analyzed using *PolyProc*, a MATLAB-based modular

processing pipeline for X-ray diffraction tomography (**Chapter 6**). The pipeline consists of data alignment (registration), masking, clean up, and grain tracking routines, which are all described in **Chapter 6** using the same Al-3.5wt%Cu alloy sample as a proof-of-concept. Namely, neighboring grains with disorientation less than 1° were clustered into one grain; additionally, grains with size and completeness below user-set thresholds were considered unreliable data and ignored in further steps.

The ACT dataset was reconstructed using the filtered back projection algorithm employed by the Scout and Scan software on the laboratory X-ray microscope. Segmentation by thresholding was relatively straightforward owing to differences in absorption between the θ-Al_2Cu particles and Al matrix. It should be emphasized that only the *centroids* of the particles (and hence, their number density) are physically meaningful quantities following segmentation. This is because the *shapes and sizes* of the particles evolve during isothermal annealing at 485 °C and the subsequent ramp down in temperature, as mentioned before.

7.3. Results and Discussion

7.3.1. Initial Condition

We first characterize the initial state of the sample, prior to isothermal annealing at 485 °C, see **Figure 7.2**. The corresponding LabDCT reconstruction at the 0 min. mark is shown at the far left in **Figure 7.3**. Using this reconstruction of 267 grains, we characterize the initial condition of our sample: the grain size distribution (**Figure 7.2a**) shows approximately log-normal behavior (see fit) and there are no such abnormal grains in system. The average grain size measures 30 μm. We also consider crystallographic properties of the initial state. The measured distribution of GB disorientations is plotted with the theoretical random distribution of GBs in **Figure 7.2b**. Comparison of the two suggests the GB distribution is nearly random, *i.e.*, there are no significant

populations of special high-angle GBs in the sample. In addition, we examine the grain texture of the initial state by constructing an inverse pole figure (IPF) of all grains in initial volume. From **Figure 7.2c** there is no distinct texture developed in the sample at the 0 min. mark.

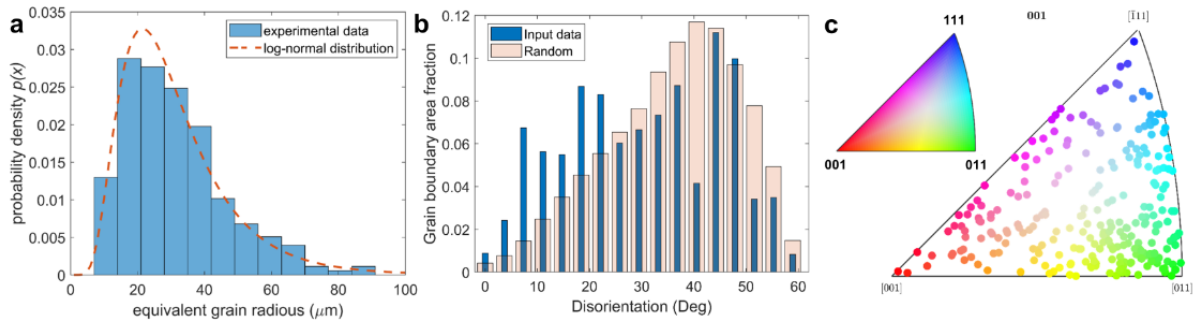

Figure 7.2. Characterization of initial state. Distributions of (a) grain size, (b) GB disorientation (*i.e.*, Mackenzie plot) with a random GB distribution shown for comparison, and (c) grain orientations (*i.e.*, inverse pole figure) with respect to the specimen *z* axis (see **Figure 7.3**), where each point is colored using the standard triangle shown inset.

7.3.2. Grain Evolution

Figure 7.3 provides discrete snapshots of the 3D grain structure at each annealing state. The entire scanned (illuminated) volume is depicted by a translucent blue color. The opaque colors indicate the crystallographic orientation of grains along the specimen *z* direction (see coordinate system). We use this color scheme throughout all figures. Intermittently unindexed regions near the top and bottom of the tomographic FOV are due to grains that are either too small or possess a low completeness level. It should be stated that the reconstructed volume represents an *open system*; that is, it is located in the vertical middle of a long pillar-shaped sample, and thus the grains visualized here are only those grains within the scope of our objective aperture. For this reason, "new" grains can emerge into the tomographic FOV from the top and/or bottom during grain growth. For example, the huge blue grain was not observed before 42 min. but appeared after that. After prolonged annealing (imaging at 97 min. step), this blue grain (abnormal grain) takes up

most of the scope volume. To show more of it, we increased the aperture size at the 67 min. mark. We prove later on that this grain is truly the abnormal grain in the microstructure.

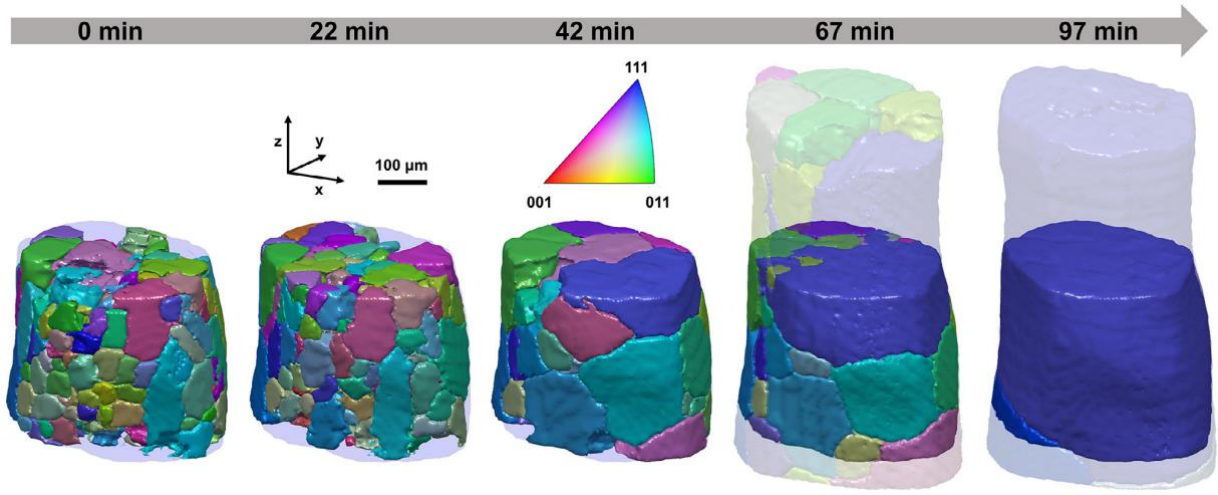

Figure 7.3. Evolution of grain structure in time. LabDCT reconstructions shown after 0, 22, 42, 67, and 97 min. of isothermal annealing at 485 °C. The translucent regions represent the full tomographic FOV, out of which we consider a 3D section (opaque) that has been filtered and aligned. Opaque colors represent grain orientation with respect to the specimen *z* direction (see inset coordinate system and corresponding standard triangle). The specimen belongs to a much longer pillar sample, hence why grains appear into the FOV at the later stages.

The corresponding evolution of the grain size distribution is presented in the form of volume-weighted probability density function (**Figure 7.4)**. Bimodal peaks are developed at later time-steps, consistent with what is expected for AGG. At the 42 min. time-step, part of the blue grain, which becomes abnormally large in the later time steps, is out of our view. That is, the initiation of AGG is not clear from our somewhat limited FOV. In any case, the bimodal distribution of grains size is clearly seen at 67 min. once a significant volume of the abnormal grain is captured. Then, the abnormal grain continues to "run away" from the grain size distribution by consuming smaller grains, resulting a colossal grain that takes up most of the sample volume (*cf.* **Figure 7.3**).

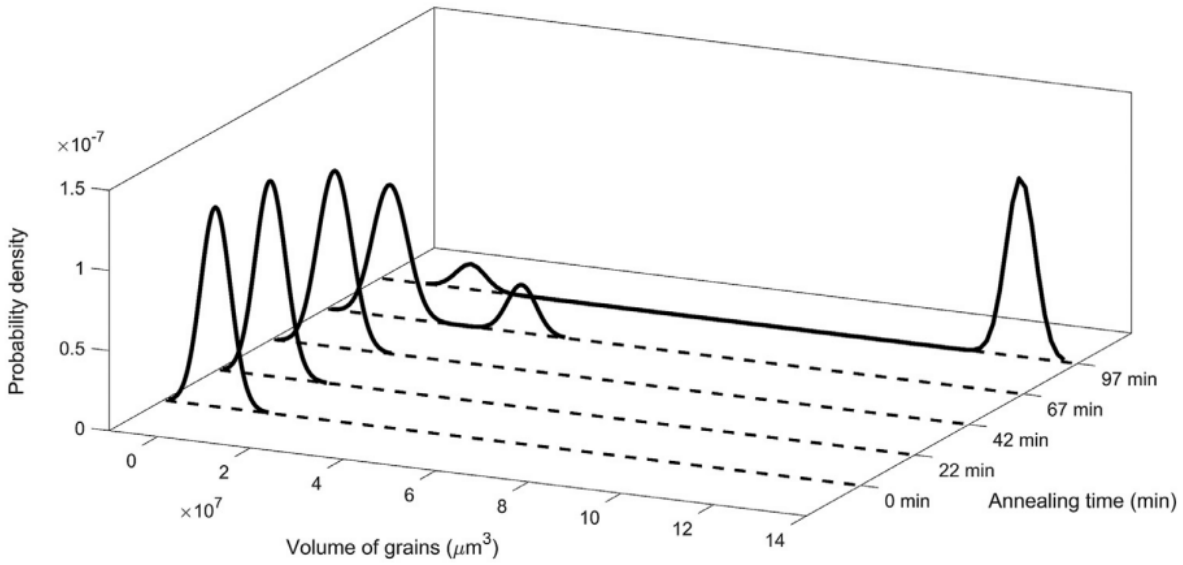

Figure 7.4. Evolution of grain volume in time, plotted as a probability distribution function. The function is not self-similar, showing a bimodal distribution of grain volumes at long times that is consistent with AGG.

We investigate a few properties of the abnormal grain including its shape, at the 67 min. mark. A number of simple metrics can be used to quantify grain morphology: For example, Holm et al. employed circularity to quantify the shapes of 2D grains undergoing grain growth [42]. Circularity is a measure of compactness, *i.e.*, how closely a shape approaches that of a mathematically perfect circle. In 3D, an analogous descriptor would be sphericity. While in principle we can apply such a metric to our collection of grains, it loses its meaning for those grains that touch the sample surfaces — in that case, the measurement of grain shape is biased by the sample geometry. To avoid such complications, we introduce a related descriptor termed convexity, ψ, defined as the ratio of grain boundary area to surface area of smallest convex polygon that can contain the grain. Visual representations of the grain surface area and its convex hull are illustrated in **Figure 7.5** on the right. For the calculation of ψ, we consider only the *interior* GB surfaces and not the *external* sample surfaces. Thus, grains that do not show any "crumpliness" of GB surfaces have $\psi \to 1$; the opposite is true for irregularly shaped grains, *i.e.*, $\psi \to 0$. The distribution of grain

convexity within this range $\psi \in (0,1)$ is correlated to grain size (**Figure 7.5)**. Remarkably, the lowest convexity value (indicative of the most irregular shape) belongs to the abnormally large blue grain. This grain shows a peninsular morphology, in direct contrast to smaller, more convex grains (see insets). Furthermore, the smaller grains are closer to equiaxed morphologies, whereas the larger grains, including the abnormal grain, have more irregular morphologies. Worth noting is that the grain with the second smallest convexity, but relatively small grain size, is one of the neighbors of the abnormal grain (that is, they touch at a grain boundary); this particular grain is encapsulated by the abnormal one. Note that most regions (including those with a peninsular morphology) within the abnormal grain are above the completeness threshold (see **Figure 7.6** for a completeness map). Overall, this result is consistent with the aforementioned study [42] that shows abnormal grains with very low compactness.

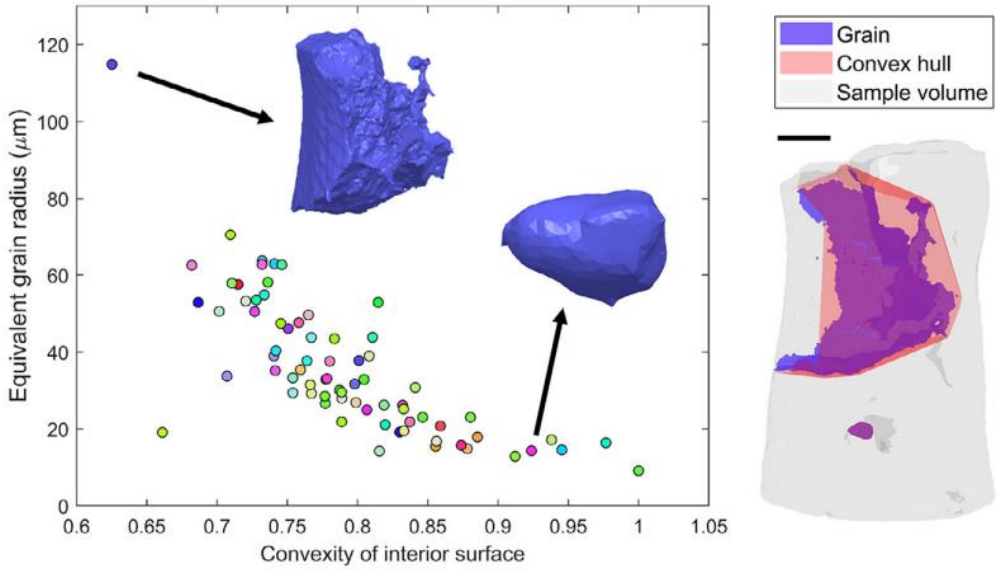

Figure 7.5. Characterization of 3D grain shape, defined as convexity of interior grain surfaces. 73 grains represented at the 67 min. anneal state. An abnormal grain (blue) and one normal grain (pink) are visualized together with their 3D convex hulls (see right). Blue color represents grains and red their convex hulls. Scale-bar on right is 100 μm.

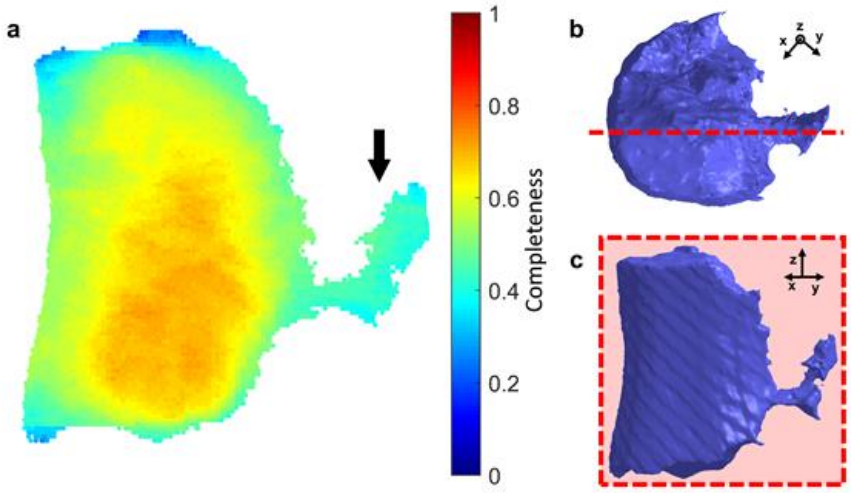

Figure 7.6. Closer look at the abnormally large grain. (a) Cross-sectional view of abnormal grain at the 67 min. time-step, where voxels within the grain are colored according to their completeness value (see colorbar). The average completeness of the peninsular region (arrow) exceeds 0.4. This particular cross-section was retrieved from the three-dimensional microstructure by cutting the abnormal grain along the red plane in (b,c).

7.3.3. Particle Distribution

We investigated the distribution of second phase θ-Al_2Cu particles by ACT, as shown in **Figure 7.7**. The 3D visualization of particle centroids shows a certain degree of non-uniformity in their locations within the bulk **(Figure 7.7a)**. From this particular viewpoint, the middle region of our sample shows a higher density of particles compared to the sides. We quantify the degree of dispersion by using the *k*-nearest-neighbors (*k*-NN) algorithm, which was previously implemented in Refs. [52,113]. In this work, *k*-NN enables determination of the k^{th} nearest-neighbor distance between particles. For example, histograms of particle-to-particle distances corresponding to $k = 1$ and $k = 3$ are shown in **Figure 7.7b**. Interestingly, a nearly bimodal distribution is seen at increasing *k* values, which is qualitatively consistent with the observation in **Figure 7.7a** of separated particle 'rich' and 'poor' regions. This result is further compared to the result of a Poisson point process (**Figure 7.7d**). We find a clear difference between the result of the experimental and the Poisson distribution. As the latter generates particles randomly, the range of

particle spacing is much narrower than the experimental result.

Delving deeper, following the method described by Tong and coworkers [147] , we plot in **Figure 7.7c** the average distance $< d >$ to the k^{th} neighbor particle, against k. The experimental results are shown in red, and the 3D analytical calculation based on a Poisson point process is presented as black dashed line. For relative smaller k (corresponding to local particle distribution), there is an obviously departure from the Poisson distribution. This provides quantitative evidence of a non-random particle distribution: for instance, the neighbors nearest to a given point are located at shorter distances (on average) compared to that of a random distribution. This situation would correspond to two particles that are narrowly separated within the particle-dense region of **Figure 7.7a**. With an increase in k, the average distance $< d >$ is increasingly insensitive to fluctuations in the particle density. The two curves in Fig. 5(c) are indistinct when $< d >$ is greater than ~100 μm.

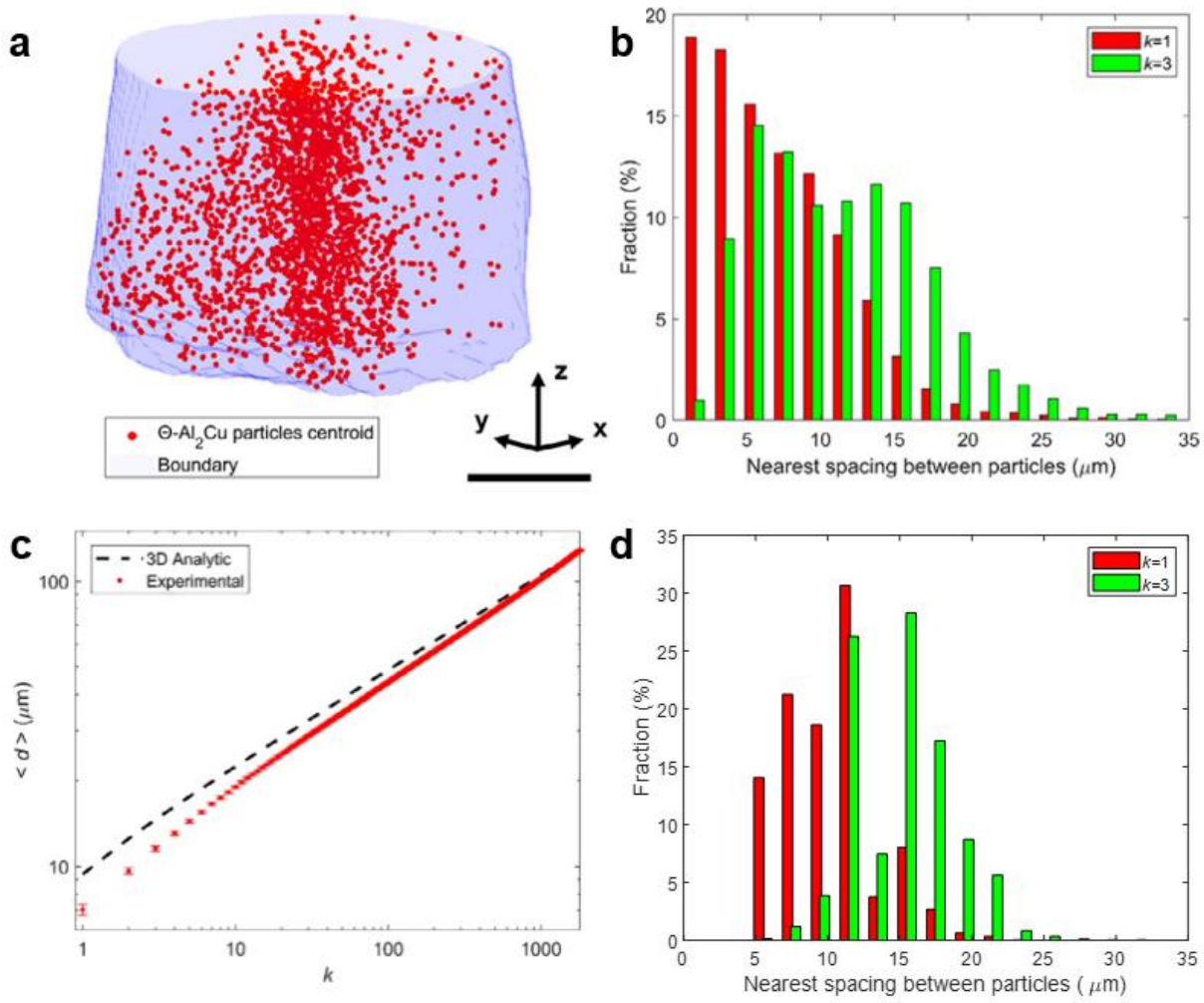

Figure 7.7. Dispersion of second-phase particles. (a) 3D ACT reconstruction. Red specks represent particle centroids and blue surfaces the contours of observed field-of-view. One out of five particles is shown for clarity. Scale bar is 100 μm. (b) Histograms of first ($k = 1$) and third ($k = 3$) nearest-neighbor distances between particles. (c) Average distance <r> between a particle and its kth nearest-neighbor plotted as a function of k (red points). For comparison, a 3D analytical calculation based on Poisson distribution is indicated by black dashed line. (d) Histograms of first ($k = 1$) and third ($k = 3$) nearest-neighbor distances assuming a Poisson distribution.

7.3.4. Multiple Regression Analysis

As mentioned in the **7.1. Introduction**, the magnitude of the grain volume change ΔV is influenced by the five quantities $\{F, V^{1/3}, n_p, M, \text{and } \gamma\}$, out of which the first three parameters can be directly measured. Among these parameters, the product $M\gamma$ can be thought of as an amplification factor for grain growth rate, since all grains have some intrinsic mobility M set by

the grain boundary character and the energy γ is part of both pressure terms (see **7.1. Introduction**). Given that Cu solute would level off the mobility as well as energy of Al GBs [148] at high misorientation and no significant fraction of "special" grain boundaries ($\Sigma 3, \Sigma 7$ and $\Sigma 11$) are observed in the sample nor the abnormal grain in particular[1] , it is reasonable to assume that the product $M\gamma$ scales with the fraction of high-angle GBs, which we denote as H. In what follows, we compute H for each grain locally. Hence, the parameter set can be reduced to $\{F, V^{1/3}, n_p, H\}$ in order to comprehend grain growth phenomena.

To trace the dominant factor for grain growth, we plot in **Figure 7.8** the change in grain volume between 42 to 67 min. annealing states — a period of time within which the abnormal grain first develops its size advantage (see **Figure 7.3**) — as a function of grain size, grain neighbors, particle density around the grain, and fraction of high angle grain boundaries, respectively. These four metrics were all evaluated at the 42 min. mark. The particle *density* here provides more localized information over the particle *number*. The grains that touch the top and bottom of our tomographic FOV were excluded from our analysis of grain topology (**Figure 7.8b**) owing to the fact that we only see a portion of these grains. It can be found that there is no preferred crystallographic orientation of grains that tend to grow or shrink. Interestingly, the first two plots go against theoretical predictions: For instance, according to the Hillert model [29] of grain growth, if the grain size is above some critical (mean) value, grains should grow; conversely, grains shrink when they are smaller than the critical value. This is clearly not true here since the largest grain (~115 μm^3) actually shrinks, see **Figure 7.8a**; presumably it rejoins the log-normal distribution of normal grains [48] at later time-steps. Similarly, according to the Mullins[149] and MacPherson-Srolovitz [150] criteria, grains should grow if they have 14 or more neighbors. Yet

[1] Among the GBs that enclose the abnormal grain, none of them is identified as "special" GBs (*i.e.*, belonging to the set { $\Sigma 3$, $\Sigma 7$ and $\Sigma 11$}) according to the Brandon criterion.

our data reveal a grain with 17 neighbors that experiences a negative growth rate, see **Figure 7.8b**. Of course, what these theories do not consider is the influence of second-phase particles. As shown in **Figure 7.8c**, we observe a larger fluctuation in grain growth *and* shrinkage rates for those grains surrounded by a relatively low particle density. Intuitively, the absence of a pinning pressure will "activate" the dynamical evolution of grain boundaries. Furthermore, not surprisingly, a higher fraction of high-angle GBs brings about a higher mobility and accordingly a larger grain growth or shrinkage rate, see **Figure 7.8d**. This plot indicates that the largest volume change corresponds to grains without low-angle GBs. Worth mentioning is that one grain dramatically outgrows the others (note the breaks on vertical axes), and this grain has relatively low particle density and highest fraction of high-angle GBs.

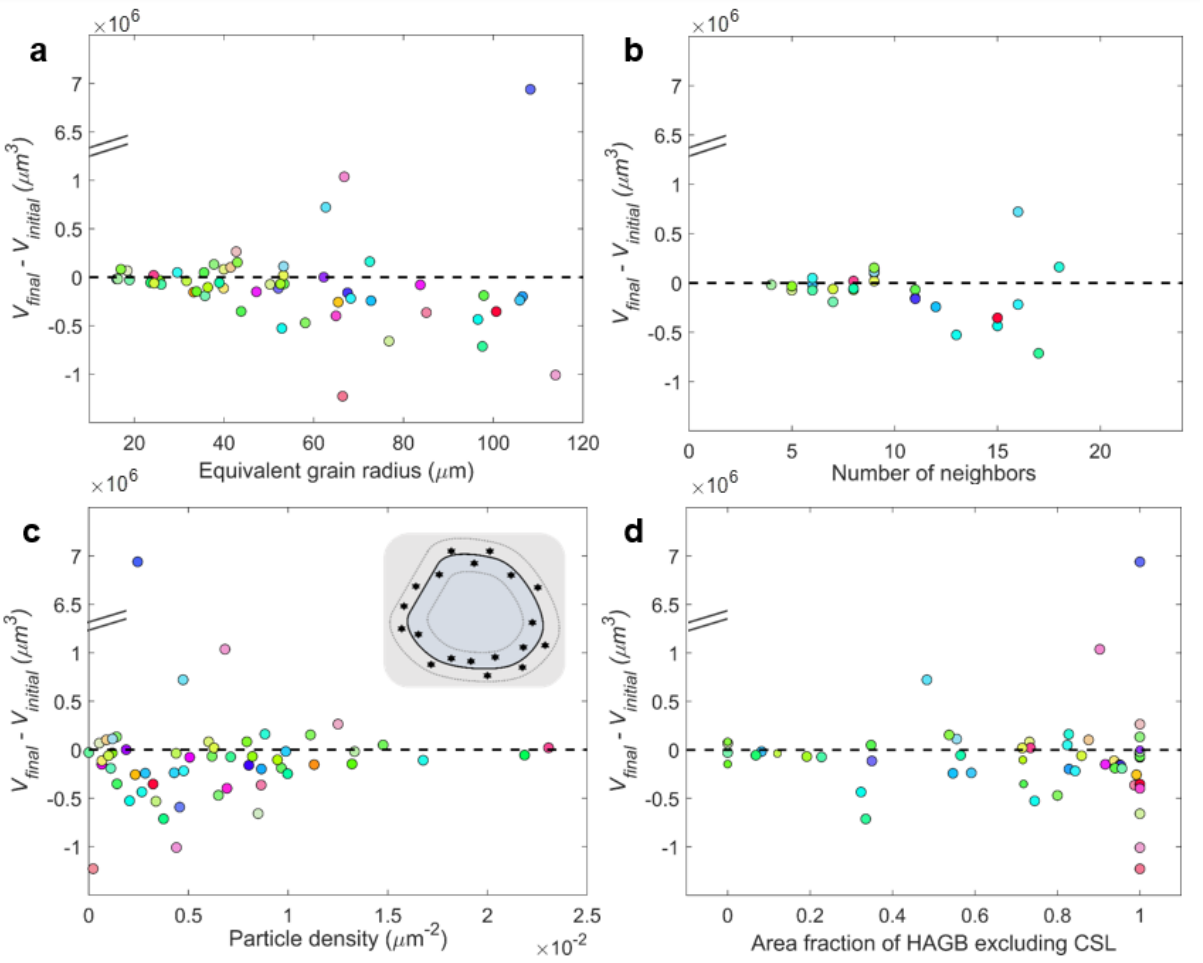

Figure 7.8. Influence of microstructural features on grain growth rates. Correlations of the grain volume change between the 42 min. and 67 min. annealing states with (a) grain size, (b) grain neighbors, (c) particle density around grain, and (d) fraction of high angle grain boundaries at 42 min. The color of data points represents the crystallographic orientation parallel to the specimen z direction using the same standard stereographic triangle from **Fig. 7.3**. Inset on (c) demonstrates how the calculation of particle density was done: we count the number of particles (black dots) within a threshold distance (thin lines) of the grain boundary and divide through by the grain surface area (thick line). Note the vertical axes breaks on all plots.

We seek to quantify the contribution of each microstructural parameter to the volumetric growth rate. To do so, we use a multiple linear regression model to control for the confounding factors listed in **Table 7.1** as potential predictors. Multiple regression bears some similarity to canonical correlation [151,152], with the exception that there is only one dependent variable in the former (here, change in grain volume between 42 and 67 min., represented as ΔV). Note also that the quantities $FV^{1/3}$ and $\mathrm{sgn}(-\Delta V)n_p$ are physically derived from the driving and pinning

pressures (see **7.1. Introduction**) associated with grain growth, respectively. Multiplication of n_p by the sign function $\mathrm{sgn}(-\Delta V)$ ensures that the pinning pressure always opposes the capillary driving pressure. The regression model is of the form $Y = \sum X_i \beta_i$ where Y is the single dependent variable, X_i is the set of dependent variables and β_i is the standardized regression coefficient (*i.e.*, the coefficient of the independent variables when all variables are expressed in the standardized form of z-score). For our analysis, we obtain a multiple R^2 of 0.73 ($p < 0.01$, from a F-test) indicating a good correlation between the independent and dependent variables. [2] The corresponding linear combination of variables is displayed in **Figure 7.9** for each of the data points (individual grains, as before), along with the regression line and a 95% confidence interval. Within the regression model, only the two independent variables involving the pinning pressure $\mathrm{sgn}(-\Delta V)n_p$ are significant predictors ($p < 0.01$, from a t-test) of grain growth rate; they also have among the highest regression coefficients β_i, see **Table 7.1**. To support these results, we conduct dimensional reduction by employing least absolute shrinkage and selection operator (LASSO) regularization. We determine λ that corresponds to the minimum mean squared error from ten-fold cross-validation. The sparse solution *via* LASSO regularization only contains four variables, H, $V^{1/3}$, $\mathrm{sgn}(-\Delta V)n_p$, and $H \times \mathrm{sgn}(-\Delta V)n_p$. MLR with these four variables gives R^2 = 0.6 (*cf.* R^2 = 0.73 for MLR with the full set of 11 variables, see above). To further investigate the significance of each of these four variables, we conduct an ablation study, which excludes one feature at a time to observe performance reduction and determine contribution of the excluded feature (**Figure 7.10**). As expected, a model without $\mathrm{sgn}(-\Delta V)n_p$ shows a greatly reduced R^2, representing poor performance without this particular variable. Additionally, a model without

[2] Using only the first four independent variables listed in **Table 7.1** leads to a weaker correlation (R^2 = 0.33, p = 0.21, from an F-test), see also **Figure 7.10**. This would indicate a discrepancy between the coefficient set X and grain growth rate Y. This motivated us to consider independent variables that were physically derived.

$H \times \text{sgn}(-\Delta V) n_p$ showed the second greatest decrease in R^2 value. The other two variables achieve a comparable result to MLR with all four variables. *Taken altogether, these results point to the strong influence of a grain's external environment* (i.e., the particle cloud) *on its growth rate.* Stated differently, the abnormal grain is selected from a particle-poor region. Given that it has mobile boundaries ($H = 1$), it will readily develop a size advantage over the normal grains.[3] We discuss the implications of these results below.

Table 7.1. Standardized regression coefficients (β_i), level of significance (p), and coefficient of determination (R) for the dependent variable Y (grain volume change) and independent variables X_i.

X_i	β_i	p	R
Residual error	0.08	0.58	N/A
H	−0.38	0.05	−0.06
F	−0.02	0.97	−0.14
$V^{1/3}$	−0.31	0.73	−0.38
n_p	0.40	0.19	−0.07
$FV^{1/3}$	−0.01	0.99	−0.31
$\text{sgn}(-\Delta V) n_p$	−0.86	<0.01	0.66
$H \times F$	0.10	0.83	−0.07
$H \times V^{1/3}$	−1.42	0.14	−0.24
$H \times n_p$	-0.45	0.30	-0.01
$H \times FV^{1/3}$	1.28	0.24	-0.19
$H \times \text{sgn}(-\Delta V) n_p$	1.10	<0.01	0.52

[3] The influence of grain boundary energy and mobility (*intrinsic* parameters) should not be understated. Even if a grain is located in a particle-poor region, it can only grow if its boundaries are sufficiently mobile (*i.e.*, $M\gamma > 0$ or $H > 0$). Conversely, grains with high mobility boundaries may be located in particle-rich regions and thus cannot grow. The importance of both boundary mobility and external environment can be seen through the independent variable $H * \text{sgn}(-\Delta V) n_p$ ($p < 0.01$, from a *t*-test).

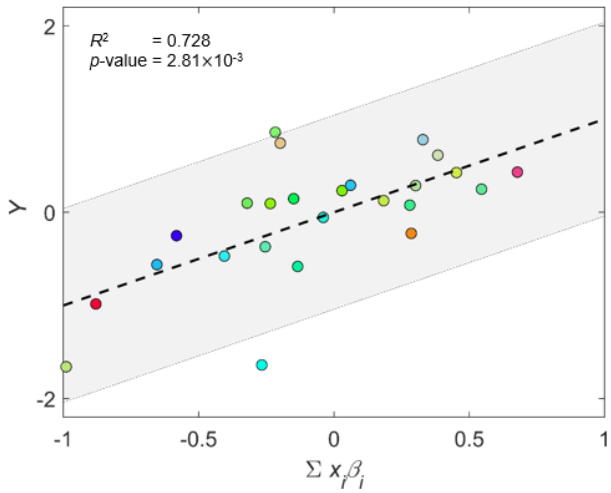

Figure 7.9. Multiple regression analysis, showing Y versus $\sum X_i\beta_i$. The regression line (dashed) and a 95% confidence interval (shaded region) are shown. As before, the color of data points represents the crystallographic orientation parallel to the specimen z direction using the same standard stereographic triangle from **Fig. 7.3**.

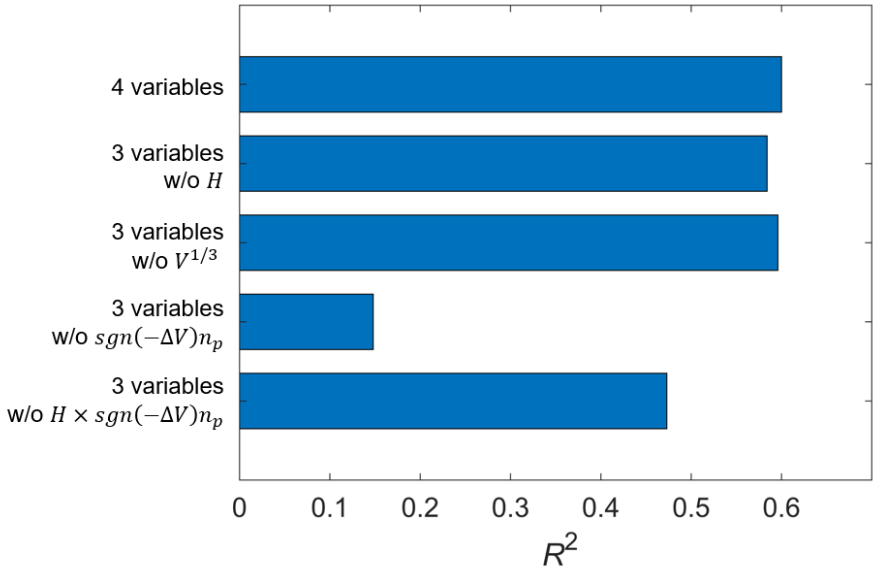

Figure 7.10. Ablation study on dimensionally reduced multiple linear regression model. The model includes four variables, H, $V^{1/3}$, $\mathrm{sgn}(-\Delta V)n_p$, and $H \times \mathrm{sgn}(-\Delta V)n_p$, after LASSO regularization.

7.3.5. Selection of Abnormal Grain

Our multiple regression analysis reveals that the dominant factor governing grain growth is the particle distribution. However, it is still unclear how exactly the local particle distribution influences the selection of the abnormal grain. According to the Zener-Smith criterion [44], the limiting (maximal) grain size is dependent on the local particle distribution when the grain boundaries are fully pinned by particles. Thus, one can infer that the particle distribution is random before annealing at 485 °C (*i.e.*, the 0 min. mark) since the grain size distribution is log-normal (see **Figure 7.4**). During further annealing at 485 °C, the particle distribution becomes non-random as the volume fraction of particles adjusts very quickly to its equilibrium value (from ≳1.6 vol% at 400 °C to 0.3 vol% at 485 °C, see **Figure 7.1**). Even so, the log-normal grain size distribution will persist for a while owing to the fact that the grain growth rate is lower than the particle dissolution rate, as shown in the schematic image of **Figure 7.11a** and the corresponding experimental result of **Figure 7.11d**. That is, there exists a *rate hysteresis* between the evolution of particles and that of GBs. Here, **Figure 7.11d-f** are representative 2D cuts of the LabDCT reconstructions at the 22, 42 and 67 min. time-steps, respectively. Ultimately, the system will strike a new balance between the local grain size and local particle distribution. At this point, the grain size distribution becomes non-random in a way that is consistent with the particle distribution (**Figure 7.11b** and **7.11e**), *i.e.*, larger grains are seen in the regions with a lower volume fraction of particles, and *vice versa*.

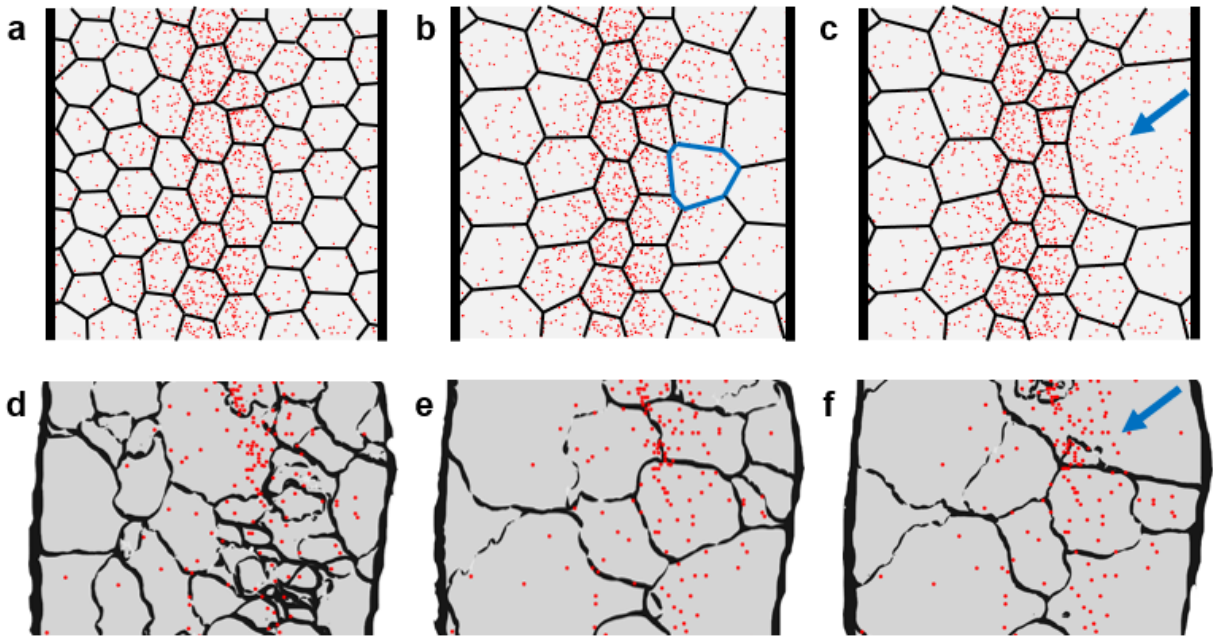

Figure 7.11. Microstructural evolution during isothermal aging at 485 °C. Schematic images are shown at (a) early, (b) intermediate, and (c) late stages of grain growth. Grain boundaries are shown in black and particles in red. The thick black outline on each schematic represents the free surface of the sample. Blue outline in (b) represents a candidate, interior grain. Corresponding cross-sectional images of superimposed ACT and LabDCT data are shown at (d) 22 min. (early), (e) 42 min. (intermediate), and (f) 67 min. (late stages). Blue arrows point to abnormal grains.

According to models of capillarity-driven grain growth [34], the driving pressure for growth is positively correlated to the number of grain neighbors and anti-correlated to the contact (dihedral) angle between grain boundaries (assuming isotropic grain boundaries). It could be imagined that the larger grains — which sit in a lower particle density region — will have more grain neighbors when touching smaller grains. One such large grain is indicated by a blue outline in **Figure 7.11b**. Such a grain can amplify its driving pressure advantage by consuming its neighbors. Subsequently the grain's accumulative driving pressure advantage will propel it towards an abnormal state, as shown in **Figure 7.11c,** and confirmed by experiment in **Figure 7.11f**. The above result and corresponding discussion indicate that particles by themselves are a necessary but insufficient condition for particle-assisted AGG. What is required is a non-random *distribution* of

particles so that grains can develop a size advantage (in the absence of any other intrinsic factors, see **7.1. Introduction**).

Based on the above discussion, it can be concluded that the *grain growth behavior is highly localized and set by the particle distribution*. For example, the expansion of the blue grain may be realized by consuming its larger grain neighbors rather than the smaller grains in its periphery, as the strong pinning pressure induced by the higher particle distribution in the central region will prohibit grain boundary migration. In contrast, a weak pinning pressure induces a growth competition in the left- and right-hand sides (that show a lower particle density). This is consistent with **Figure 7.8** that shows a higher fluctuation in grain volume change for grains with a larger size, more neighbors, and sparse particle density, as those grains are more mobile than all others.

7.3.6. Persistence of Abnormal Grain during Growth

Once the abnormal grain has developed its size advantage, why and how does it parasitically take over the microstructure? Why should it persist through regions of high particle density? Is a critical grain size required for these processes to occur in a cascade? To answer these questions, and especially the latter, we recall from the **7.1. Introduction** that the grain growth rate is determined by a balance between a driving pressure and a retarding pinning pressure. This pinning pressure is assumed to be proportional to the particle distribution. However, the means for evaluating the driving pressure is still somewhat indefinite [52,138]. Recently, a capillarity-driven grain growth model was generalized from 2D [32] to 3D [34,35]. This model showed excellent agreement with experimental results on normal grain growth [36] in a particle-free system. We seek to extend this model to a particle-containing system in order to predict the stability fields associated with AGG in 3D. While in our case the particle distribution is far from uniform, it is nevertheless instructive to consider mean-field approximations as a first-order approach.

By injecting Smith-Zener pinning into the 3D capillarity-driven grain growth model [34,35], we derive the following two growth laws,

$$\frac{dR_{ab}}{dt} = M\gamma\left(\frac{1}{R_n^m} - \frac{1}{R_{ab}} - \frac{1}{2R_0}\right) \quad \textbf{(Equation 7.2)}$$

$$\frac{dR_n^m}{dt} = M\gamma\left(\frac{1}{2R_n^m} - \frac{1}{2R_0}\right) \quad \textbf{(Equation 7.3)}$$

where R_0 is the normal grain size when GBs are pinned by particles; and R_n^m and R_{ab} is the mean size of normal and abnormal grains, respectively. The first equation thus pertains to the growth rate of the abnormal grain and the second to that of the normal grains. In order for AGG to take place, both the absolute and relative growth rate should be greater than zero, *i.e.*, $\frac{dR_{ab}}{dt} > 0$ and $\frac{d}{dt}\left(\frac{R_{ab}}{R_n^m}\right) > 0$. In other words, the abnormal grain should be growing with a positive driving pressure and at a rate that is higher than the normal grains. These two conditions are solved and plotted as solid lines in the "mechanism map" (**Figure 7.12**), wherein the horizontal axis represents the pinning efficiency of the particles and vertical axis the size advantage of the abnormal grain. The inner locus of the two curves represents the characteristic field for which AGG is favorable (see shaded red region). It can be seen that the critical grain size for which the abnormal grain will outgrow its neighbors is $R_{ab}/R_n^m > 2$, which is a little higher than that of aforementioned two models [52,138] (dashed and dot-dashed lines). Even so, the tendency of all models is essentially the same: the required size advantage (R_{ab}/R_n^m) is minimal when the matrix grain boundaries are strongly pinned by second-phase particles (R_n^m/R_0).

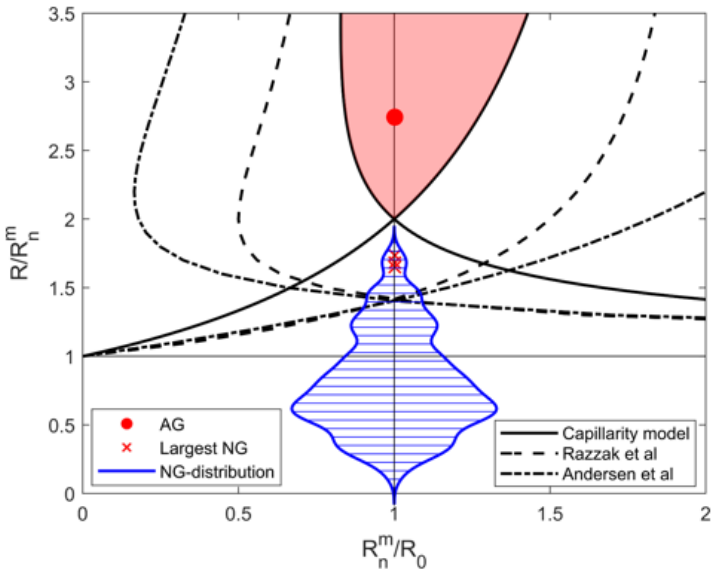

Figure 7.12. Mechanism maps of abnormal grain growth. Superimposed are three different models [52,138] (solid, dashed, and dot-dashed lines) together with experimental results (colored data points) corresponding to the 67 min. annealed state. The abnormal grain is marked by red color and the distribution of normal grains is presented by a symmetric blue outline. The width of this outline along the vertical axis indicates probability density of normal grains.

We can plot our experimental results on **Figure 7.12**, by assuming that the mean normal grain size, R_n^m, does not evolve significantly at the later stages and thus $R_n^m/R_0 = 1$. We show only the data pertaining to the 67 min. time-step as this is right before the abnormal grain consumes the sample volume (see **Figure 7.3**). Consistent with predictions from our mechanism map, the abnormal grain (indicated by red dot) is located in the region wherein abnormal growth is favorable, whereas all normal grains are below this regime. We also indicate the four largest normal grains and observe those grains are located in the NGG region based on our model but in AGG region based on the work by Razzak *et al.* [34] and Andersen *et al.* [52]. As such, the abnormal grain outgrows the normal grains, and eventually engulfs the sample at the 97 min. mark. That the mechanism map is consistent with our experimental observations is remarkable given its underlying assumptions. The simple criterion of $R_{ab}/R_n^m > 2$ is helpful in understanding the importance of size advantage on the persistence of the abnormal grain during grain growth, yet its

applicability is limited to systems with a random distribution of particles, for reasons that are explained below.

To reconcile our experimental data with the model, we incorporate the influence of a gradient in the particle distribution. We consider a one-dimensional (1D) system with continuous gradient in particle distribution and grain size. Since the local particle density determines local grain size, one can expect, in turn, a gradient in grain size once the grains are fully pinned. The corresponding distribution of normal mean grain size R_n^m in 1D space *S* is schematically illustrated in **Figure 13a**. Of note is that R_n^m is never a single value in particle-gradient system as local particle density determines local mean grain size. Let us insert in the distribution an abnormal (ab) candidate grain. It is surrounded by normal grains of size $R_n + \Delta R_n$ and $R_n - \Delta R_n$ on either side, where ΔR_n indicates the departure in local mean grain size away at distance R_{ab}. In this case, we must update the neighbor grain sizes in our expression (**Equation 7.2**) for abnormal grain growth rate:

$$\frac{dR_{ab}}{dt} = M\gamma\left[\frac{1}{2}\left(\frac{1}{R_n+\Delta R_n} + \frac{1}{R_n-\Delta R_n}\right) - \frac{1}{R_{ab}} - \frac{1}{2R_0}\right] \quad \textbf{(Equation 7.4)}$$

To induce AGG, the absolute abnormal grain growth rate would need to be greater than zero, *i.e.*, $\frac{dR_{ab}}{dt} > 0$ under the condition that grain boundaries are fully pinned ($R_n/R_0 = 1$). Thus, we find from Eq. (R1) that the size advantage required for persistent AGG can be expressed as

$$\frac{R_{ab}}{R_n} > \frac{2(1-\delta^2)}{1+\delta^2} \quad \textbf{(Equation 7.5)}$$

where $\delta = \Delta R_n/R_n$. **Figure 7.13b** shows a plot of R_{ab}/R_n against δ. Note the previous "mean field" model assumed $\delta = 0$ and hence $R_{ab}/R_n^m > 2$. In comparison, a non-random particle distribution ($\delta > 0$) relaxes the grain size advantage. That is, an abnormal grain *does not* need to have double the radius of a normal grain to persist in its growth, in systems with gradients in

particle density. For example, the critical grain size to trigger AGG is only R_{ab}/R_n >1.9 when $\delta = 0.15$.

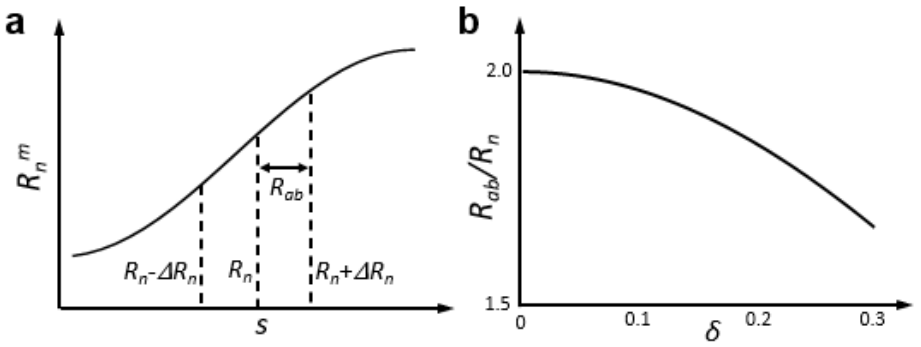

Figure 7.13. Influence of non-random particle distribution on abnormal grain growth. (a) Illustration of local grain size distribution R_n^m in one-dimensional space *S*. R_n is the normal grain size at a certain position and ΔR_n indicates the deviation in grain size away from this position. (b) Plot of critical grain size advantage for AGG (R_{ab}/R_n) *versus* homogeneity parameter $\delta = \Delta R_n/R_n$.

The above analysis indicates *why* the abnormal grain should run away from the grain size distribution, but does not explain *how* it does so. According to DeCost and Holm [42], one possible mechanism is that AGG propagates by a series of fast, localized growth spurts involving high-mobility grain boundaries. These authors investigated the influence of non-uniform boundary mobility on AGG, but their arguments may be interpreted more generally in terms of a non-uniform particle distribution (as in our case). As a result of these localized events, the abnormal grain develops a highly irregular morphology. Our 3D results qualitatively agree with those of simulation: namely, the AG shows the lowest convexity value, representing the most irregular shape among the full set of grains at the 67 min. time-step (see **Figure 7.5**). The low convexity of the abnormal grain stems from its highly peninsular morphology, resembling other abnormal grains seen in computational [42] and experimental studies [42]. The unusual morphology may represent how the abnormal grain propagates through the particle cloud, presumably "exploring"

regions of low particle density. Further confirmation of this route will be left for future work. At present, we are limited by a low temporal resolution between subsequent 3D reconstructions and a limited number of grains (a few hundred). Future developments in the LabDCT technique will enable us to probe larger samples in a shorter amount of time.

7.4. Summary

The phenomenon of AGG in the presence of particles throws into question our conventional wisdom, namely that particles pin the GBs and prevent grain growth from taking place. To better understand the dynamics of this secretive process, we harnessed new strides in laboratory-based 3D X-ray microscopy. Through our multimodal imaging platform, we were able to capture the evolution of grains (*via* LabDCT) and the distribution of particles (*via* ACT) in an Al-Cu alloy. We observed AGG after isothermally annealing our sample below the solvus temperature. Meanwhile, we detected a non-uniform particle distribution with a broad range of inter-particle spacings. By integrating the results of LabDCT and ACT, we determined that the most significant predictor of grain growth rate is the local particle density. That is, larger grains are found in regions of lower particle density and *vice versa*. Once a grain develops a size advantage — that reflects the underlying particle distribution — it may persist to consume the sample volume. We provide some guidelines for when this might occur, based on an analytical model that considers both capillary and pinning pressures. On the whole, we offer a new explanation for AGG in systems with a non-uniform distribution of particles, which is more often the norm and not the exception. The insights gained can be used to identify favorable microstructural environments associated with the initiation of AGG in heterogeneous materials.

Chapter 8. Origin of Non-random Particle Distributions

This chapter is based on the article published in *Metallurgical and Materials Transactions A* [82], for which I retain the right to include it in this dissertation, provided it is not published commercially. The co-authors are Ning Lu and Ashwin J. Shahani. This work was supported by the Army Research Office Young Investigator Program under award no. W911NF-18-1-0162 and University of Michigan College of Engineering.

8.1. Introduction

Control of microstructure is critically important for many physical properties, such as strength and ductility. In other words, modification of microstructure leads to a corresponding variation of materials properties. A well-known example is the Hall-Petch relationship in which yield strength σ_y is related to grain size R of a polycrystal as $\sigma_y \propto R^{-1/2}$ [3,4]. In multi-phase alloys, *e.g.*, particle-containing systems, the grain size is governed in large part by the distribution of second phase particles since the particles exert a pinning pressure on grain boundary migration [44]. Based on the classical Smith-Zener pinning mechanism, grain size is proportional to the particle size r and inversely proportional to phase fraction f as $R \propto r/f$ [44]. Therefore, the distribution of second phases (*i.e.*, their local fractions and local particle sizes) ultimately determines the grain structure and, in turn, the mechanical properties.

In general, grain growth *via* capillarity ($R \propto t^{1/2}$) is faster than coarsening of particles *via* bulk diffusion ($r \propto t^{1/3}$) in the limit of infinite dilution ($f \to 0$) [1,23,30,153]. Therefore, grains adopt their pinned configurations (where the capillary pressure balances the particle pinning

pressure) while particle coarsening becomes a rate limiting step. As the second phase particles continue to coarsen through Ostwald ripening, one may infer that grain structure would evolve *in tandem* during isothermal annealing. That is, the grain size retains a log-normal distribution and smoothly shifts to larger average grain size (the hallmark of normal grain growth) [29,125]. Contrary to this logic, in some cases, discontinuous or AGG events have been observed in particle-containing systems, wherein a few grains "run away" from the log-normal distribution at relatively high temperature, thus generating a bimodal grain distribution [49,131–135,154,155]. The evolution of grain size distribution would, in turn, induce changes in materials properties and may limit the lifetime of the material in-service. In some cases where AGG is particularly severe, the abnormal grain can consume the microstructure, leading to a single crystal [46,156].

In past theoretical treatments, investigators developed ‘mean field’ and statistical models to assess the origins of AGG in particle-containing alloys [29,52,138,157,158]. Typical assumptions are (1) isotropic grain boundary properties; (2) a fixed and random particle distribution throughout annealing; and (3) a correspondingly uniform distribution of grain size after preliminary recrystallization. Under these conditions, a grain can become abnormal if it has a critical size advantage over the other grains. The exact criteria for a grain to obtain this size advantage depend on the dimensionality of the system (2-dimensional (2D) *vs.* 3-dimensional (3D)), among other factors. Even so, these mean field models do not specify *how* to achieve a target grain size advantage in the face of an evolving particle distribution, in order to either initiate or bypass AGG for technological applications.

More recently, Refs. [49,81,133,159] suggested that the grain size advantage might be caused by local thermal fluctuations or non-random particle distributions. Rios [159] proposed that a locally lower pinning pressure adjacent to a large grain can cause it to become unstable and grow

abnormally. In a similar vein, Holm *et al.* [133] showed *via* Monte Carlo Potts simulations that a few grains can thermally fluctuate from the local particle cloud and grow abnormally, even without particle dissolution and coarsening. However, this model was not cross-checked against experiment. On the other hand, AGG may be attributed to a non-random particle distribution. For instance, by taking 2D SEM observations of an Al-3.5wt%Cu alloy, Dennis et al. [49] found a lower fraction of θ-Al_2Cu particles phase at the grain boundaries of the abnormal grain compared to those of the fine matrix grains. Aided by new developments in four-dimensional (*i.e.*, 3D space plus time-resolved) laboratory X-ray microscopy, Lu *et al.* [81] **(Chapter 7)** investigated the particle distribution as well as the grain structure evolution in the same alloy. The results showed that particle distribution was non-random during the course of annealing at temperatures near (but below) the solvus (491 °C). Accordingly, one of grains in the particle-poor regions became abnormally large, eventually accruing a capillary driving pressure that far exceeds that of the other (normal) grains. However, the exact reason for a non-random particle distribution (and hence non-uniform pinning pressure) is still unclear. It should be emphasized that the sample was homogenized at 550 °C for 4 hr. and a random particle distribution was observed prior to isothermal annealing for grain growth [81]. In light of these details, we hypothesize that the transition of the particle distribution from random to non-random takes place upon annealing, and that it is chiefly responsible for the initiation of AGG.

As mentioned above, the two features of the particle distribution that govern grain growth are phase fraction and particle size. Hence, the annealing temperature and time would be key processing variables. In this work, we characterize the particle evolution and grain growth behavior in an Al-3.5wt%Cu alloy as a function of these two parameters. We find the particle distribution is random immediately after preliminary recrystallization but deviates from random with

increasing annealing temperature (below the solvus) and/or increasing annealing time. We quantify the inhomogeneity of particle distribution by borrowing an important measure from the economics of inequality, the Gini coefficient. Interestingly, the transformation from NGG to AGG takes place when the distribution of particles achieves a critical Gini coefficient. This result confirms that a certain degree of inhomogeneity in the spatial arrangement of particles is necessary for AGG to take over. We propose an analytical model to describe the evolution of the particle distribution and its implications to grain growth. Our combined experimental-modelling efforts reveal that even a slight Cu segregation (after homogenization) would lead to a highly non-uniform particle distribution (and AGG) at relatively high temperatures (below the solvus). Conversely, NGG is favored at lower temperatures and shorter times. These results are presented on a TTT diagram that traces the operational window for AGG.

8.2. Experimental Methods

8.2.1 Sample Preparation

An ingot with composition of Al-3.5wt%Cu was acquired from the Materials Preparation Center at Ames Laboratory (Ames, IA, USA). All other impurity elements were less than 0.01wt%. The subsequent processing steps were based on Dennis *et al.*[49] and our prior work [81] (**Chapter 7**). That is, the sample cut from ingot was firstly homogenized at 550 °C for 4 hours. After cold rolling with 50 % thickness reduction, the sample was heat treated at 400 °C for 30 min to induce primary recrystallization. These treatments were assumed to provide a sufficiently random distribution of θ-Al_2Cu particles and an equiaxed and strain-free grain structure.

8.2.2. Characterization

The microstructure of the samples was characterized by SEM in a TESCAN MIRA3 microscope with a field emission gun (FEG), at the Michigan Center for Materials Characterization (MC^2) at the University of Michigan. Elemental dispersions of Al and Cu before and after homogenization were inspected by energy dispersive X-ray spectroscopy (EDS). The grain structure and crystallographic texture right after primary recrystallization were examined by electron backscatter diffraction (EBSD). The samples were mechanically ground and polished for EDS, and further FIB-polished by dual-beam system Helios G4 PFIB UXe for EBSD.

Grain structure evolution throughout further annealing was characterized by backscatter electron (BSE) imaging in an interrupted manner. That is, the prepared samples were isothermally annealed at 445, 465, 475, 485, 490 °C and then air-cooled after 0, 10, 20, 35, 55, 80 min. After each of anneal segments, the grain structure and particle distribution were measured (*vide infra*). Altogether, we collected a total of 78 images at different (temperature, time) coordinates.

8.2.3. Data Processing

In what follows, we focus on the evolution of particles and their spatial inhomogeneity, since our past work [81] **(Chapter 7)** indicates that the local particle density determines grain growth rates. Measurements of various microstructural features (*e.g.*, grain size, number of neighbors, local particle density, *etc.*) and their contributions to AGG are given in Ref. [81] **(Chapter 7)**. Here, we quantify the spatial inhomogeneity of the particles from each image. Taking the example of the BSE image collected after annealing at 475 °C for 35 min. (**Figure 8.1a**), wherein the discrete white specks represent Al_2Cu particles, we assess the inhomogeneity of particle distribution by a convenient single index known as the Gini coefficient [160,161]. Formally, the Gini coefficient measures the extent to which the distribution of particles across

spatial units deviates from uniformity. If the unit size is large (low granularity), then a *random* distribution converges to a *uniform* distribution [162,163]. To measure the Gini coefficient, we must first transfer the discrete data of particle positions to a quasi-continuous distribution (that shows the normalized probability density of particles, see **Figure 8.1b**) through kernel density estimation. Physically, the estimated probability density reflects the spatially averaged fraction of θ-Al_2Cu phase. For clearer illustration, one out of every five particles is also rendered as white specks in **Figure 8.1b**. Regions with higher probability density (yellow) show a correspondingly higher number of white specks (particles), which demonstrates a consistent mapping between the discrete particle data and the probability density function. Of note is that we take into account the particle size as a weighting factor during estimation since the pinning pressure is proportional to particle size (see **8.1. Introduction**). Based on the improved Sheather-Jones method [164] — a 'nonparametric' method that does not require an underlying model for the data — we determined the optimized bandwidth as 4-6 times the average area per observed particle occupied, with an output grid of 64×64. The corresponding Gini coefficient (see below) of the particle distribution (**Figure 8.1c**) is in the range of 0.35-0.38, which suggests that it is not very sensitive to bandwidth selection. In the following analysis, we use a bandwidth with 6 times the average area to process all images and make impartial comparisons.

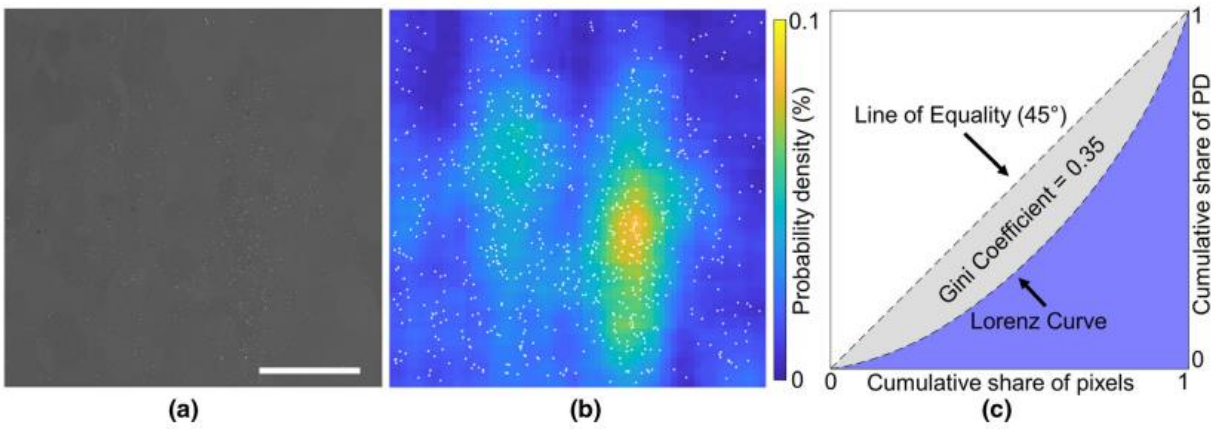

Figure 8.1. *Estimation of Gini coefficient associated with the distribution of particles.* (a) SEM/BSE image of sample annealed at 475 °C for 35 min. Scale bar measures 200 μm. (b) Corresponding (normalized) probability density of particles. One of five particles' centroids are presented by white specks. (c) Calculation of Gini coefficient based on (b). The 'PD' in the ordinate refers to the probability density of particles. See text for details.

After we estimate the quasi-continuous distribution, we then assess the degree of inhomogeneity in the distribution of particles by computing the dimensionless Gini coefficient. The metric was originally intended to represent the income distribution of residents and is the most widely used measure of economic inequality. Somewhat analogously, we treat each pixel after kernel density estimation as isolated spatial unit (*resident*) and its pixel value as its expected particle density (*income*). The Gini coefficient is graphically represented through the so-called Lorenz curve L, which is found by plotting the cumulative percentile of pixels on the abscissa against cumulative probability density on the ordinate, as shown in **Figure 8.1c**. Mathematically, the Lorenz curve is calculated as $L(i/n) = \sum_1^i p(i)$, where $p(i)$ is the normalized probability density of the i^{th} pixel sorted in increasing order and n ($64 \times 64 = 4096$) is the total number of pixels in the image. Then, the Gini coefficient G is computed as double the area (grey) between the Lorenz curve and the line of equality (which strikes the origin at a 45° angle), or $G = 2(1/2 - \sum_1^n L(i/n)\,/n)$. It can be seen that G ranges from 0 to 1, with the limits 0 and 1 representing a

uniform distribution (under low measurement granularity) and complete segregation of particles, respectively. For the particle distribution shown in **Figure 8.1a**, $G = 0.35$.

8.3. Results and Discussion

8.3.1. Elemental Distributions before and after Homogenization

Given that element Cu is indispensable for precipitation of θ-Al_2Cu particles (which consist of ~50wt%Cu), it is logical to infer that particle distribution is dominated by the local Cu dispersion. Homogenization for 4 hr. at 550 °C (above solvus) is conducted to realize a reasonably uniform Cu dispersion prior to particle precipitation. To verify this effect, we characterize the sample before and after homogenization *via* SEM, as shown in **Figure 8.2**. Before homogenization, typical eutectic features can be observed in the interdendritic regions (*e.g.*, lamellae of θ-Al_2Cu phase, as shown in top half of **Figure 8.2a**). The corresponding EDS analysis (bottom half of **Figure 8.2a**) confirms that the Cu constituent is concentrated in the θ-Al_2Cu phase (green), which suggests a highly non-uniform Cu dispersion due to chemical segregation. After the homogenization treatment, the dendritic structure disappears, and the BSE image becomes featureless (see upper half of **Figure 8.2b**). Due to interdiffusion, there is no obvious Cu segregation based on preliminary EDS analysis (bottom half of **Figure 8.2b**). To illustrate the Cu dispersion more clearly, we plot in **Figure 8.2c** the ratio of Cu to Al counts (photons of Cu Kα radiation to that of Al Kα radiation). Slight fluctuations in the count ratio indicate a relatively weak Cu segregation. This is consistent with our metallurgical intuition that it is impossible to achieve a uniform Cu dispersion even after annealing for a finite amount of time. For example, assuming instantaneous, localized sources in infinite media [2], the concentration c of diffusant (here, Cu) in one-dimensional (1D) space S at some time t is $c(S,t) = \frac{n_d}{(\pi D t)^{1/2}} e^{-S^2/(4Dt)}$, where n_d is the

total mass of diffusant (Cu) and D is the bulk diffusivity of diffusant in the matrix (for Cu in Al at 550 °C, 540 μm^2/hour [145]). After $t = 4$ hr. of annealing, we estimate the range of Cu segregation to be about 50%. Although this value is higher than our experimental observation — likely due to the departure of the initial condition from the *Dirac* function — it still indicates the residual segregation of elemental Cu following homogenization.

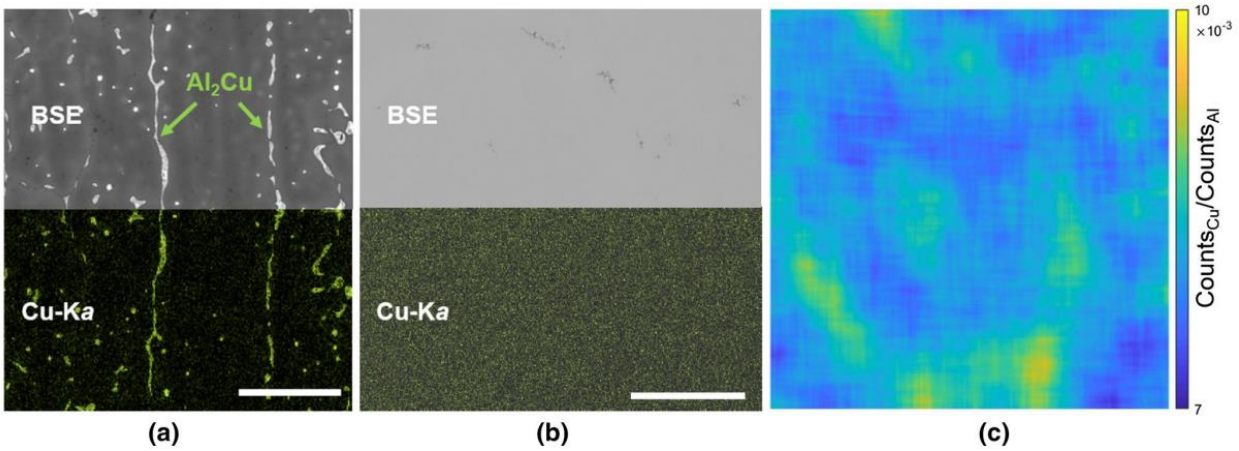

Figure 8.2. Chemical distributions before and after homogenization. (*a*) SEM/BSE image of cast ingot (top half), with element map (counts) of Cu (bottom half). (*b*) SEM/BSE image of sample after 4 hr. homogenization at 550 °C (top half), with element map (counts) of Cu (bottom half). (*c*) Ratio of the counts of Cu (Kα) to that of Al (Kα), corresponding to image (*b*). Scale-bars in (*a*) and (*b*) measure 200 and 500 μm, respectively.

8.3.2. Microstructure after Primary Recrystallization

After confirming the near-uniform Cu dispersion after homogenization, the sample was cold-rolled and subsequently heat treated at 400 °C for 30 min. for precipitation and recrystallization. Then, we examined the particle distribution and grain structure by BSE and EBSD, respectively. A clearly random particle distribution is shown in BSE image (**Figure 8.3a**). No obvious agglomeration nor abnormally large particles can be seen (see inset). The average nearest-neighbor distance between particles is ~2-3 μm. The grain map retrieved from EBSD (**Figure 8.3b**) indicates an equiaxed grain structure is achieved after primary recrystallization. In

addition, a nearly random distribution of orientations confirms that no preferred texture is developed after recrystallization. We note that past studies with similarly prepared samples demonstrate also a weak crystallographic texture. Namely, in our own previous investigation [81] – **Chapter 7**, which involves the same ingot as well as sample preparation procedure, we characterized the crystallography of 267 individual grains in 3D and confirmed that no obvious texture was developed in our sample during annealing **(Figure 7.2)**.

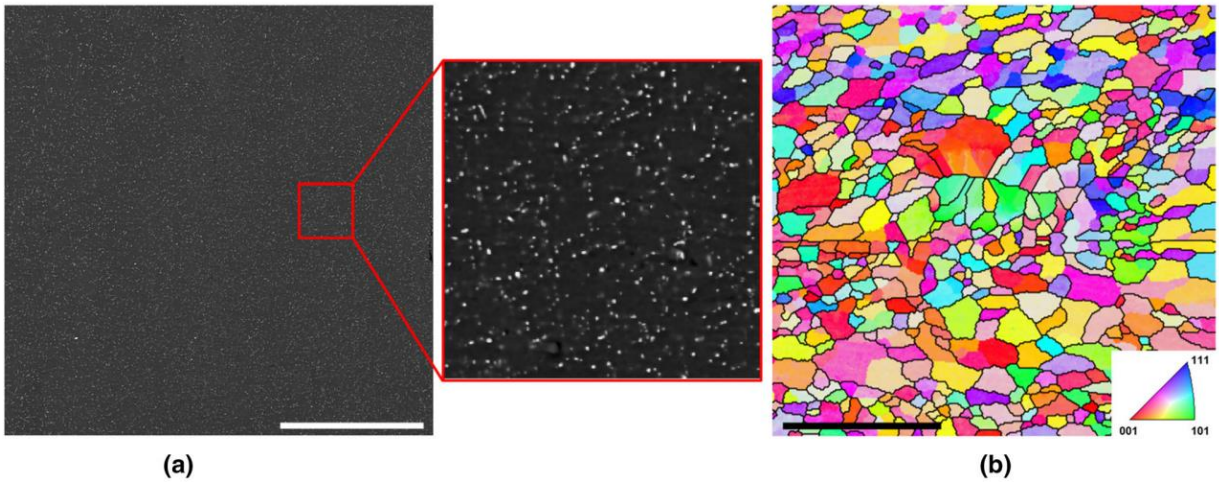

Figure 8.3. Particle distribution and grain structure after cold-rolling and annealing at 400 °C for 30 min. (a) SEM/BSE images. White specks are θ-Al_2Cu particles (see inset for a magnified view). (b) SEM/EBSD grain map. Colors indicate crystallographic orientations of grains along the normal vector of page. All scale-bars measure 200 μm.

8.3.3. Evolution of Particle Distribution upon Annealing

After recrystallization, the samples are subject to heat treatment at various annealing temperatures and annealing times, the effect of which is to alter both the phase fraction and particle size, and consequently the particle distribution. Examples of particle distributions at various conditions are shown in **Figure 8.4**. More specifically, the sequence of images in **Figure 8.4a** shows the evolution of the particle distribution upon isothermal annealing at 485 °C for 0, 10 and

20 min. As expected, the particle density is significantly reduced owing to dissolution. Interestingly, however, this particle dissolution is non-uniform across the sample since particles preferentially disappear in some regions as opposed to others, leading to a highly non-random distribution. The inhomogeneity in the particle distribution persists upon further annealing at 485 °C due to slow coarsening rate of particles (**Figure 8.5**). On the other hand, by varying the annealing temperature (465, 475 and 485 °C) and holding the annealing time fixed at 35 min. (**Figure 8.4b**), we recognize a clear transition toward a non-random distribution of particles. Generally, the particle distribution becomes highly heterogeneous at long times and/or high temperatures, the reasons for which are discussed in subsequent sections.

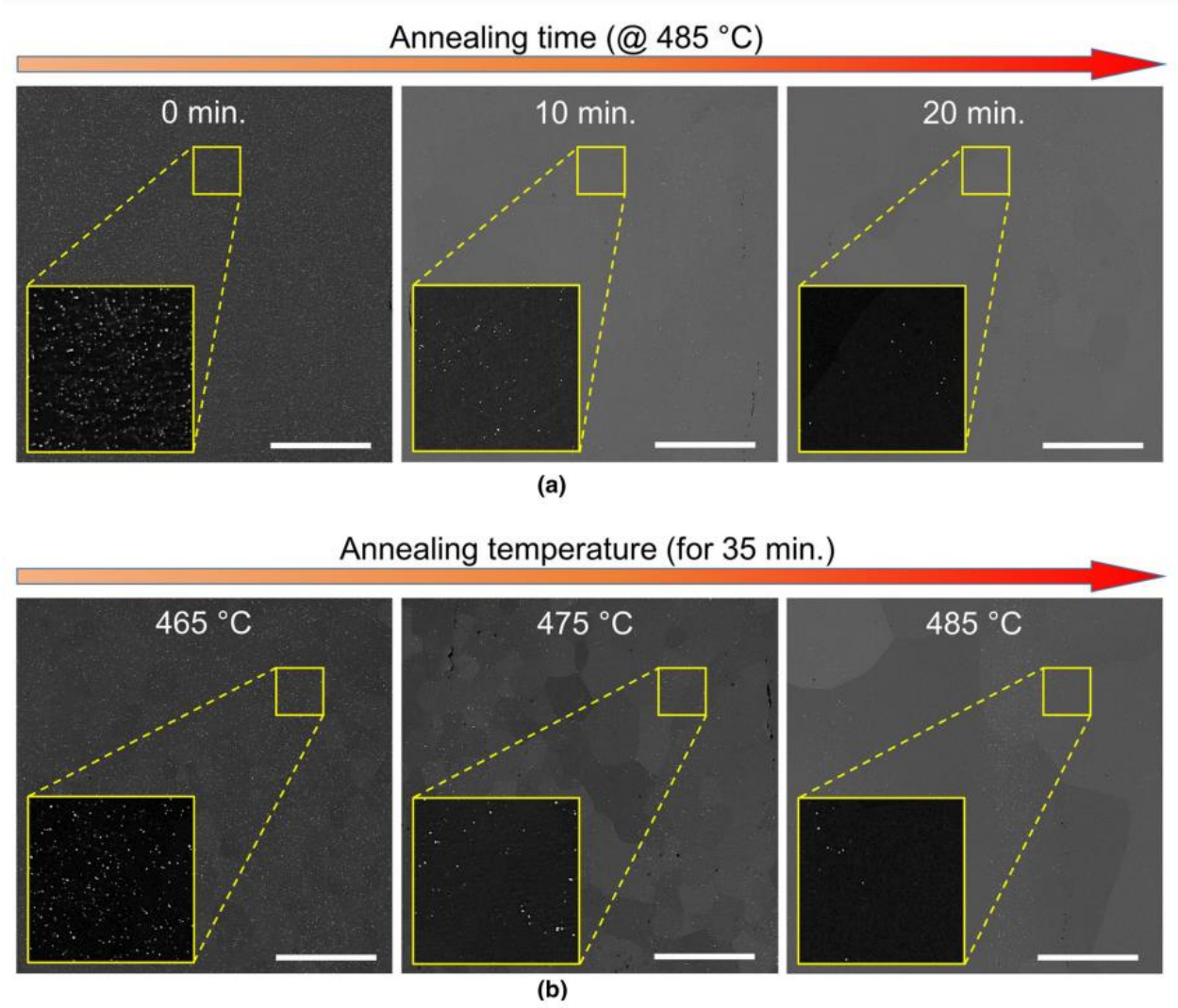

Figure 8.4. Examples of particle distribution at various annealing temperatures and times. (a) SEM/BSE images of Al-Cu alloy annealed isothermally at 485 °C for 0-, 10- and 20-min. White specks are θ-Al_2Cu particles (see insets). (b) SEM/BSE images at temperatures of 465, 475 and 485 °C after 35 min. All scale-bars measure 200 μm.

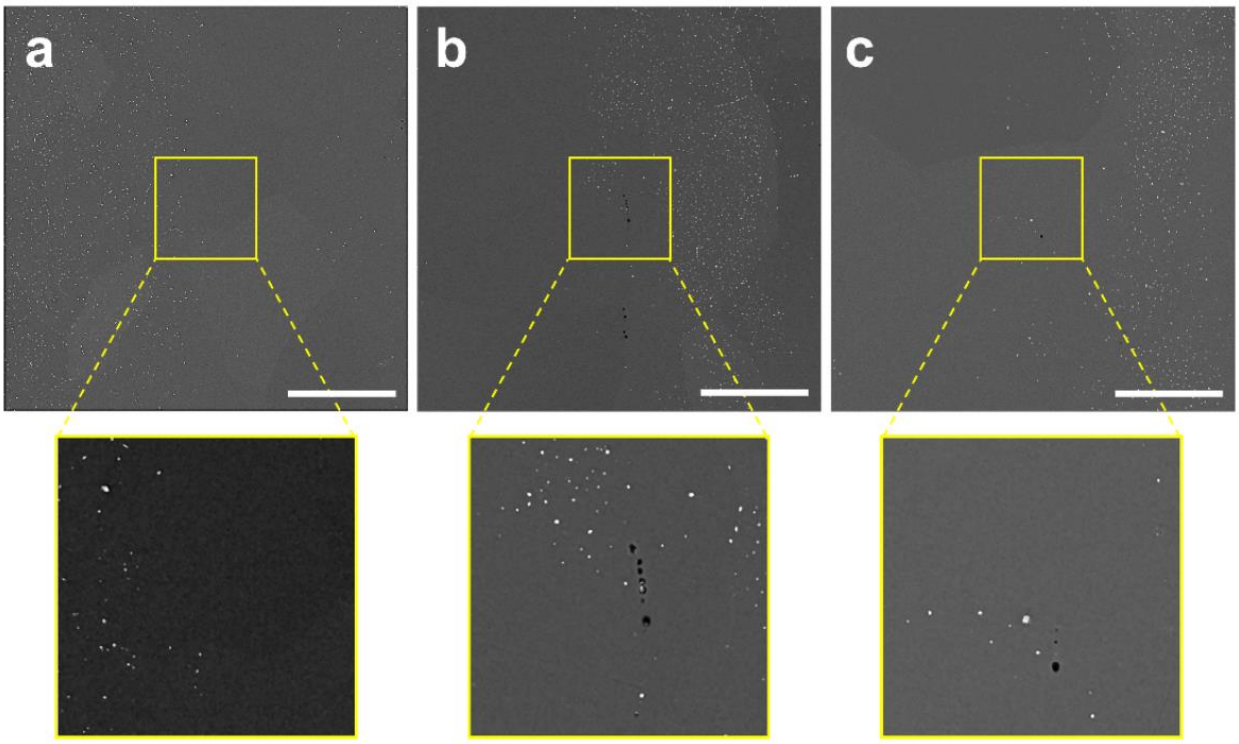

Figure 8.5. Examples of particle distribution at annealing temperature of 485 °C for longer times. (a through c) SEM/BSE images collected after 35-, 55-, and 80-min. White specks are θ-Al_2Cu particles (see insets). All scale-bars measure 200 μm.

To describe and compare the particle distribution across all annealing steps, we quantify the inhomogeneity of particle distribution using the Gini coefficient G (see **Section 8.2.3**). The variation of G as a function of annealing time and temperature is displayed in **Figure 8.6**. It should be noted that filled/open symbols represent calculated G values from experiments (**Figure 8.5**); we employ third-order polynomial fitting to extrapolate between our measurements (color-bar). The result shows that when the annealing temperature is lower than 470 °C, the particle distribution retains the incipient Gini coefficient ($G < 0.2$) irrespective of annealing time. At temperatures higher than 470 °C, G varies dramatically over the course of annealing, increasing significantly before 20 min. and then increasing only slightly after that, which might be explained by rapid dissolution followed by a more gradual coarsening of particles, respectively. The highest Gini coefficient ($G \cong 0.6$) associated with a highly non-random particle distribution can be found at

485 °C after 20 min. It is important to mention that G decreases in the sample annealed at 490 °C for 35 min ($G \cong 0.3$). We confirmed that this behavior is due to severe particle dissolution as the temperature approaches the solvus (491 °C). Since the Gini coefficient reflects the inequality among individuals (here, pixels), severe dissolution will let the particle-rich regions be in the minority. That is, most pixels are devoid of particles and thus show a similar behavior. Consequently, the average area per particle occupied increases with the reduction in particle number (see **Section 8.2.3**). Thereby the bandwidth for kernel density estimation increases dramatically, thus reducing the Gini coefficient.

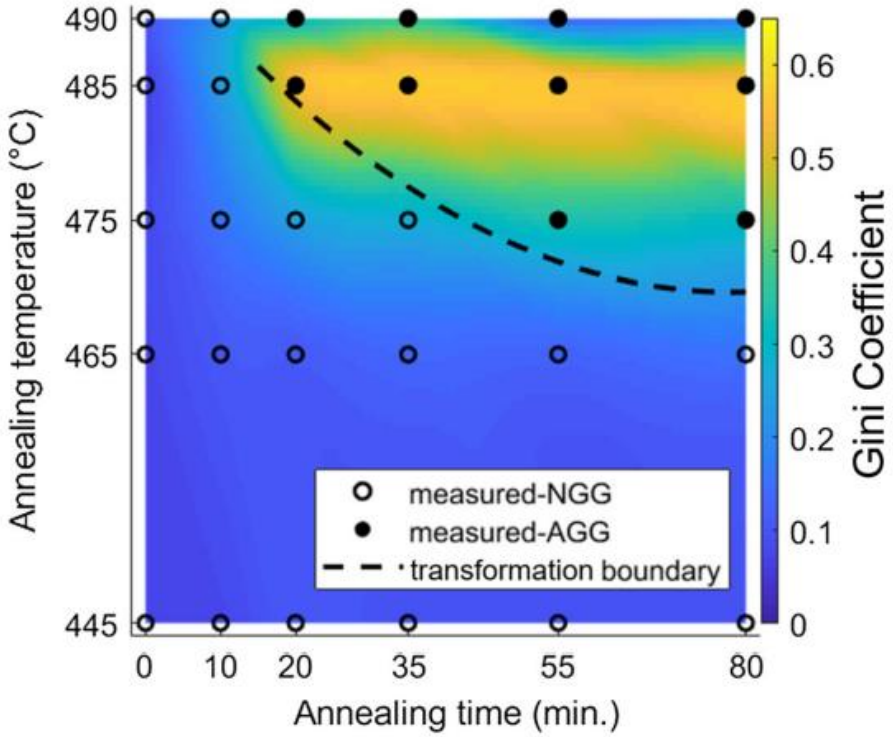

Figure 8.6. Variation of Gini coefficient (associated with the particle distribution) with annealing temperature and time (TTT diagram). Symbols indicate where we measured particle distributions and grain structures (filled: AGG, open: NGG). Data points were fit to a third-degree polynomial, see color-bar. Yellow regions indicate inhomogeneity ($G \geq 0.65$) and dark blue the converse. Dashed line represents the transformation boundary between NGG and AGG.

Of note is that the non-random particle distribution here does not originate from deformation. In previous studies[1,165,166], investigators report the segregation of particles to

'bands' in Al alloys after cold rolling, where the bands lie *parallel* to the rolling direction. While we indeed perform cold rolling, the particle-rich band is roughly *perpendicular* to the rolling direction in our case (see **Figure 8.7**), suggesting the particle distribution is not influenced too strongly by extrinsic factors such as deformation.

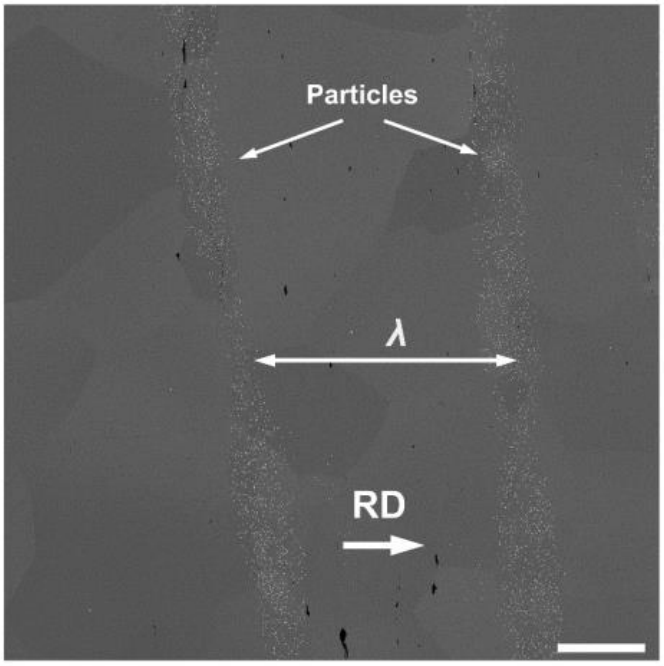

Figure 8.7. Extended scope of particle observation at annealing temperature of 485 °C for 80 min., showing particle rich bands. RD indicates rolling direction and λ the spacing between the bands. Scale-bar measures 200 μm

8.3.4. Transformation in Grain Growth Behavior

The consensus in the metallurgical community is that second phase particles restrict grain growth by pinning the grain boundaries. What is much less recognized is the impact of the *evolving particle distribution* on grain growth. Examples of NGG and AGG are shown in **Figure 8.8**. In **Figure 8.8a-d**, we provide both the grain structure captured by SEM/BSE (inset) as well as the corresponding grain size distribution (outset). Furthermore, we plot probability density functions of the grain size in **Figure 8.8d**. As discussed in **8.1. Introduction**, we can distinguish grain

growth behavior by considering the shape of the grain size distribution: unimodal for NGG and bimodal for AGG [167]. With this criteria in mind, **Figure 8.8a-b** reveal the typical NGG behavior after 20 and 35 min. of annealing. However, after 55 min. of annealing (see **Figure 8.8c**), a few colossal grains appear, transforming the grain size distribution to a bimodal shape (indicative of AGG, see **Figure 8.8d**). These three inset images of grain structure were obtained by filtering and adjusting the contrast of the raw BSE images to reveal the grain structure.

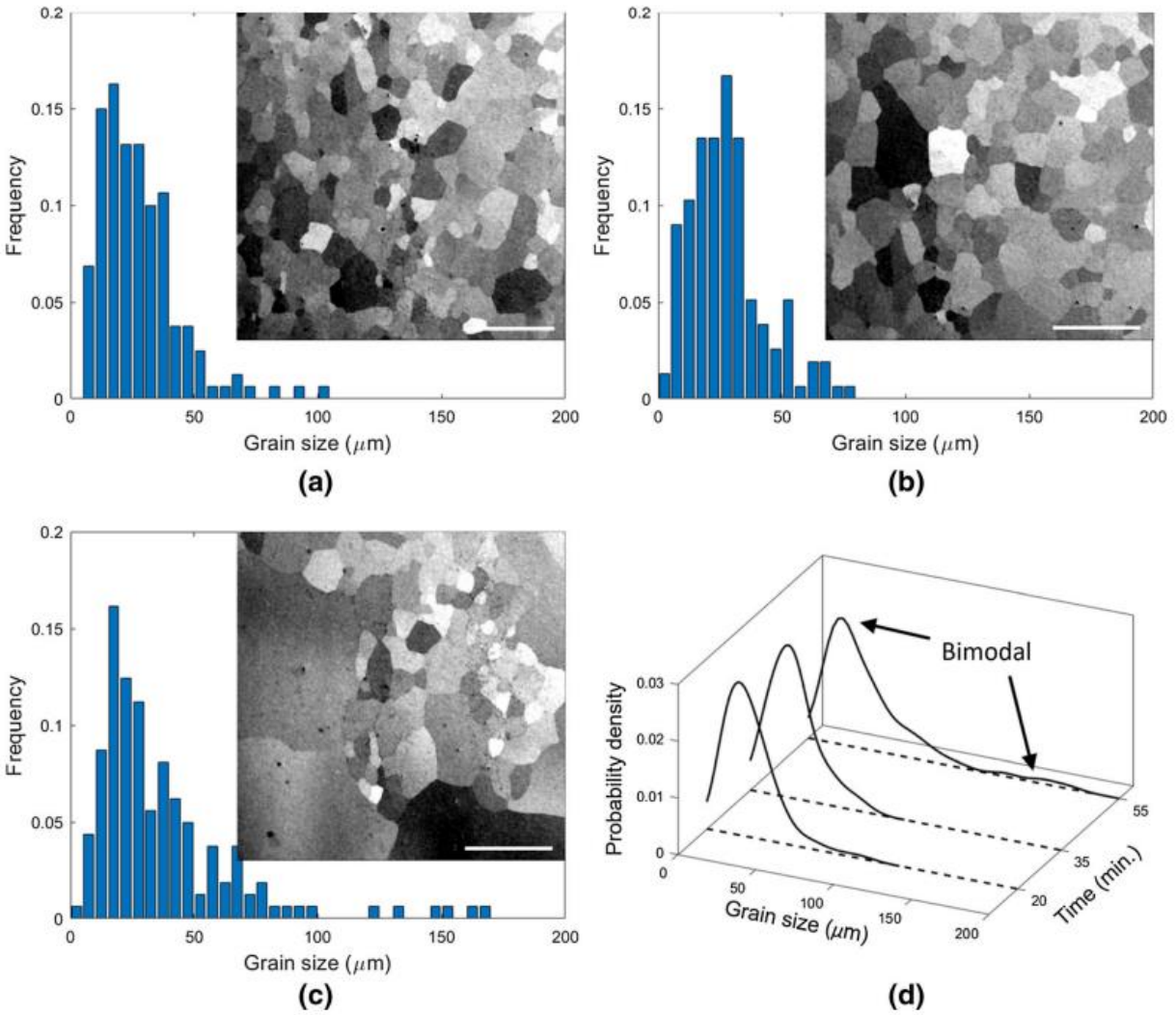

Figure 8.8. Evolution of grain growth behavior upon annealing. (*a-c*) Representative grain structures obtained by SEM/BSE (inset) and corresponding grain size distributions (outset) after annealing at 475 °C for 20, 35, and 55 min, respectively. Scale-bars: 200 μm. (*d*) Probability density functions of grain size corresponding to (*a-c*).

To trace the underlying relationship between the distribution of particles and the mode of grain growth, we superimpose in **Figure 8.6** the binary classification of grain structure (AGG or NGG) on the bivariate (temperature *vs.* time) distribution of Gini coefficients. We observe AGG in 10 annealing states (marked by filled symbols), whereas the remainder show NGG (open symbols). Interestingly, AGG occurs only when the particle distribution achieves a certain or critical degree of inhomogeneity ($G > 0.2$). Based on this result, we draw a rough boundary on

Figure 8.6, which represents the onset of AGG (*i.e.*, the runaway of a few grains from the grain size distribution). By doing so, we uncover a time-temperature-(structural) transformation (TTT) diagram that identifies the stability fields of NGG and AGG. This information helps to anticipate the grain growth behavior (whether it is NGG or AGG) at a given annealing state (temperature and time), and ultimately, to control granular microstructure through thermal processing.

8.3.5. Influence of Cu Segregation on Particle Dispersion

Based on the above analysis, we find that the transformation of grain growth behavior from NGG to AGG is associated with the transition of particle distribution from random to non-random. This is consistent with our previous 3D observations pertaining to an Al-3.5wt%Cu alloy [81] **(Chapter 7)**. With these results in mind, we draw our attention to the question of what is the mechanism by which the particle distribution becomes highly non-random?

At a given temperature and composition, mass fractions f of the two phases (α-Al and θ-Al_2Cu) can be determined from the Al-Cu phase diagram [168], reprinted in **Figure 8.9a**. According to the lever rule [169], they are calculated as $f_\alpha = \frac{l_\alpha}{l_\alpha + l_\theta}$ and $f_\theta = \frac{l_\theta}{l_\alpha + l_\theta}$, respectively. Here, l_θ is the length of the green line, or the difference of mass fraction of Cu in α phase and the alloy. Similarly, l_a is the length of red line, or the difference of mass fraction of Cu in the alloy and θ phase. To account for the spatial fluctuation in Cu concentration after homogenization (see **Section 8.3.1**), herein we introduce a term Δl that specifies the local deviation of Cu from the nominal 3.5wt%, as shown in **Figure 8.9a**. It can be either negative or positive depending on whether the region is locally Cu sparse or dense. Accordingly, we update the above expressions to $f_\alpha = \frac{l_\alpha - \Delta l}{l_\alpha + l_\theta}$ and $f_\theta = \frac{l_\theta + \Delta l}{l_a + l_\theta}$.

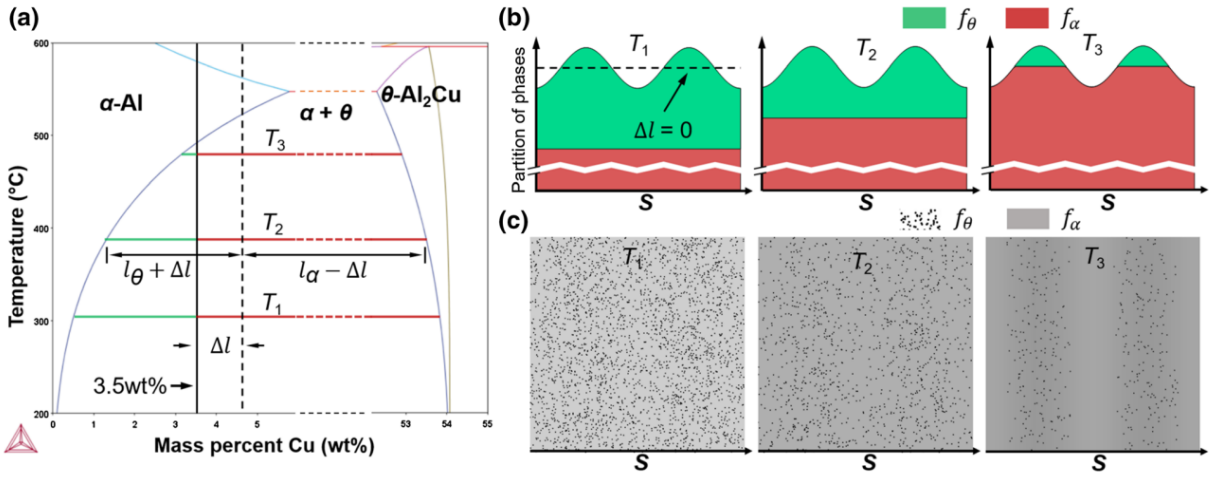

Figure 8.9. Influence of Cu segregation on particle distribution. (*a*) Phase diagram of Al-Cu. Deviation of Cu concentration from the nominal value is indicated by Δl. See text for details. (*b*) Schematic illustrations of partitioning of θ-Al_2Cu and α-Al at three temperatures ($T_1 < T_2 < T_3$), along a 1D domain S. (*c*) Illustrations of particle distribution at the same temperatures as in (*b*), now in a quasi-1D domain S. Note axis breaks on (a-b).

In our case, since Δl ($\ll 3.5$wt%) is much smaller than l_α ($\sim$50wt%), the variation of mass fraction of α matrix f_α is insensitive to Δl. Therefore, the effect of Cu segregation (Δl) could be neglected and ultimately f_α is only dependent on annealing temperature:

$$f_\alpha \approx \frac{l_\alpha}{l_\alpha + l_\theta} \qquad \textbf{(Equation 8.1)}$$

On the other hand, for f_θ, Δl would be non-negligible as it is comparable in magnitude to l_θ. This is especially true when l_θ tends to zero as the annealing temperature approaches the solvus. In order to better clarify the influence of Δl on f_θ, we rewrite the latter as $f_\theta = \frac{l_\theta}{l_\alpha + l_\theta} + \frac{\Delta l}{l_\alpha + l_\theta}$. The first term on the right-hand-side is solely impacted by the annealing temperature (similar to the above discussion). Meanwhile, the second term is the contribution associated with Cu segregation. As before, we can neglect l_θ (< 3.5 wt%), given that it is hardly comparable to l_α ($\sim$50 wt%). Therefore, the mass fraction of θ-Al_2Cu phase could be simplified as

$$f_\theta \approx \frac{l_\theta}{l_\alpha + l_\theta} + \frac{\Delta l}{l_\alpha}$$ (**Equation 8.2**)

Because of the nearly fixed constitution of Cu in θ-Al_2Cu, l_α is roughly a constant. That is, f_θ consists of a standard, temperature-dependent term (the first one) and a temperature-independent term (the second). We emphasize again that the above simplifications are only for sake of understanding the influence of residual Cu segregation on phase partition (although the sum of the mass fraction of those two phases ($f_\alpha + f_\theta$) never yields unity).

Following **Equations 8.1-2**, we illustrate in **Figure 8.9b** the phase partition at elevated temperatures ($T_1 < T_2 < T_3$) in the two-phase regime. Phase fractions of θ-Al_2Cu and α-Al are represented by the relative heights of the green and red domains, respectively, in 1D space *S*. The Cu segregation parameter Δl (as well as $\Delta l/l_\alpha$) are expected to follow a sinusoidal profile based on homogenization theory [170]. Note again that the amplitude of the fluctuation in θ-Al_2Cu phase fraction, $\Delta l/l_\alpha$, retains the same value at various temperatures. Of course, the profile would be flat ($\Delta l = 0$) for a perfectly homogeneous (uniform) dispersion of Cu, as indicated by black dashed line in the top left panel of **Figure 8.9b**. With increasing temperature, the length of the green line (l_θ) is gradually reduced, as shown in **Figure 8.9a**. Accordingly, a smaller fraction of θ-Al_2Cu phase would be predicted at equilibrium (see **Figure8.9b**). When the annealing temperature approaches the solvus (T_3), regions that sit in relatively Cu poor regions are now totally devoid of the θ-Al_2Cu phase. Furthermore, the θ-Al_2Cu phase fraction f_θ is related to particle density n_v as $n_v \propto f_\theta/v_p$ (where v_p is the particle volume). We would thus expect a corresponding non-random particle density at relatively higher temperatures assuming a constant particle size, as shown schematically in **Figure 8.9c**. The trends conveyed by the illustrations in **Figure 8.9c** match our experimental results in **Figure 8.4b**. Namely, we observe a highly non-random particle distribution

at high temperatures. Although the influence of Cu segregation on phase dispersion is negligible at lower temperatures, its impact is greatly magnified when approaching the solvus from below.

The discussion above is strictly based on thermodynamic arguments with the assumption of infinitely fast dissolution. In reality, dissolution takes time, with the dissolved fraction g being inversely proportional to the initial, local phase fraction f_θ^0, assuming it is diffusion-limited and there is no overlap of solutal fields [171]: $g = \frac{\sqrt{2Dt}}{f_\theta^0 \lambda} \frac{(x^{\alpha/\theta} - x^m)}{(x^\theta - x^m)}$, where D is the diffusivity of Cu in α-Al, t is dissolution time, λ is the spacing between Cu segregates, $x^{\alpha/\theta}$ is the Cu concentration in the matrix at the α/θ interface (as long as the θ-Al_2Cu is not completely dissolved), x^θ is the Cu concentration in θ-Al_2Cu and x^m is the initial Cu concentration in α-Al (far from the α/θ interface). Given the minor fluctuation of Cu concentration of the sample (**Figure 8.2b**), the dissolution rates across the sample will not strongly impact the results of our above discussion (*i.e.*, the dividing line between the red and green regions in **Figure 8.9b** should be nearly flat). If we assume a constant rate of dissolution, we should expect the particle distribution to evolve from random to non-random upon isothermal annealing at elevated temperatures (right below the solvus), as the system moves toward an equilibrium phase fraction of θ-Al_2Cu. We confirm this behavior in **Figure 8.5a**.

We find also that thermal fluctuations are inconsequential at the scale of our experimental data. Thermal fluctuations are thought to lead to compositional fluctuations such that some pockets of the sample are thermodynamically favored to undergo precipitation to θ-Al_2Cu, and likewise other pockets undergo dissolution. From fluctuation theory, fluctuations in composition may be approximated as a Gaussian probability distribution function. Following Landau and Lifshitz [172,173], we calculated the variance of Cu concentration $\langle(\Delta c)^2\rangle$ as $\langle(\Delta c)^2\rangle = \frac{k_B T}{N\left(\frac{\partial \mu}{\partial c}\right)_{P,T}}$, where T

is temperature (465-490 °C), k_B is Boltzmann constant, N is the total number of atoms in a single pixel and $\left(\frac{\partial \mu}{\partial c}\right)_{P,T}$ is the first derivative of the chemical potential of α-Al with respect to 3.5wt% of Cu evaluated at constant pressure (1 atm) and temperature. Assuming a pixel size of ~10^2 μm^2 (used in calculating the Gini coefficient) and estimating the chemical potential as a function of Cu concentration *via* Thermo-Calc, we estimate the variance in Cu concentration $\langle(\Delta c)^2\rangle$ to be less than 10^{-15} within the temperature range given above. Since it is not comparable to the average Cu concentration, thermal fluctuations play a very minor role (compared to residual segregation) and thus we do not consider it further in our analysis.

8.3.6. Strategies to Prevent AGG

The above results suggest that in order to restrict the occurrence of AGG, we should understand the origins of a non-uniform Cu dispersion. To this end, we investigate the evolution of the Cu dispersion prior to isothermal annealing. After solidification, equiaxed grains are found in the center of the casting while columnar grains radiate from the chilled surfaces. Although our sample is prepared by conventional casting, the thickness of our button-shaped ingot (~1.5 cm) is much smaller than its diameter (~5 cm). As a result of the limited thickness and hence the steep temperature gradient normal to the top/bottom surfaces (relative to the solidification rate), a columnar growth morphology is produced, as illustrated in the upper panel of **Figure 8.10a**. This is confirmed by our observation of a columnar grain structure in **Figure 8.2a**. The θ-Al_2Cu phase is mainly dispersed in the interdendritic regions, as presented in the bottom panel of **Figure 8.10a**. After homogenization above the solvus, the Cu species dissolves from θ-Al_2Cu phase and diffuses into α-Al phase. As a result, the Cu-rich (or -poor) regions have a periodicity of λ (see **Figure 8.10b**), which is equivalent to the primary dendrite arm spacing from **Figure 8.10a**.

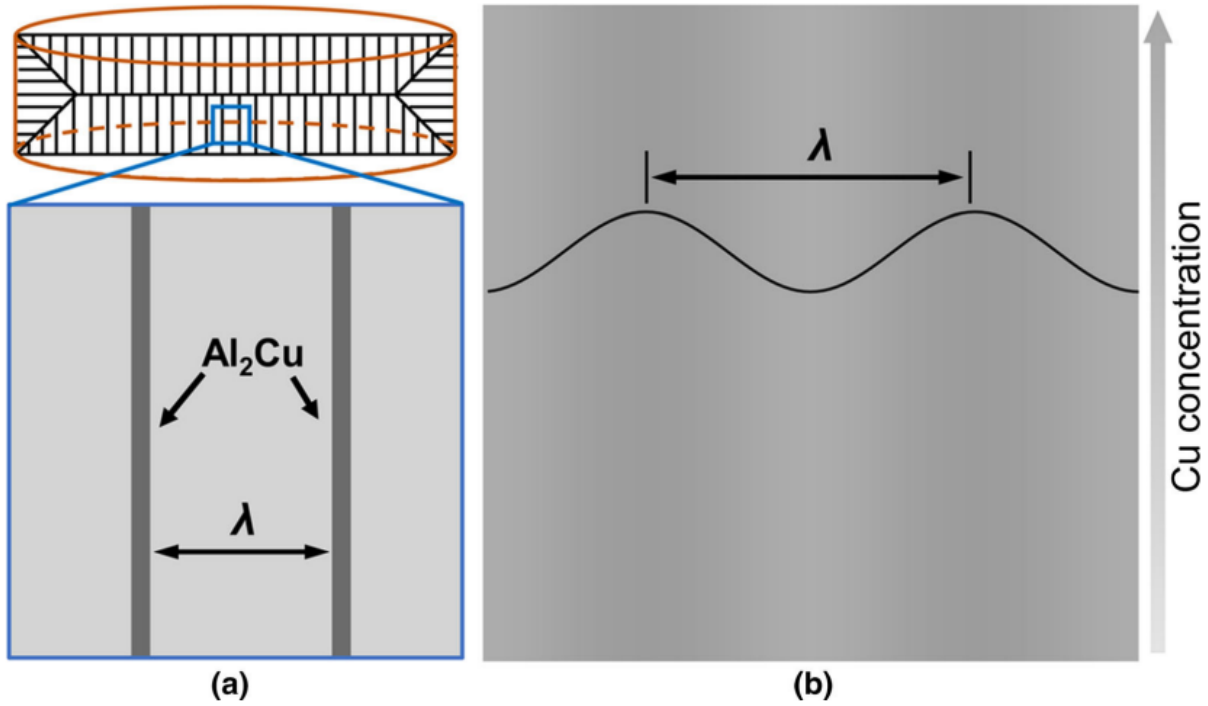

Figure 8.10. Influence of processing history on Cu distribution. (a) Cast microstructure consists of columnar grains, where θ-Al_2Cu is mainly found in interdendritic regions (dark gray). (b) Cu distribution following homogenization.

To further illustrate the behavior of Cu segregation/homogenization, we mathematically express the mass fraction to be a sinusoidal function [170] given by

$$f_\theta(S) = a + b \sin\left(S\frac{\pi}{\lambda} - \frac{\pi}{2}\right) \qquad \textbf{(Equation 8.3)}$$

where a represents the mass fraction of θ-Al_2Cu phase without Cu segregation ($\Delta l = 0$), b indicates the amplitude of the fluctuation ($\Delta l / l_a$) and λ is the spacing between Cu segregates. A prolonged homogenization is also expected to flatten the gradients in Cu distribution (decrease in b). Annealing for relatively short durations (for a few hours) will lead to a highly non-uniform θ-Al_2Cu phase distribution when approaching solvus from below, as shown in **Figure 8.11a**. On the contrary, an even longer homogenization treatment will reduce the Cu segregation and hence the fluctuation of θ-Al_2Cu phase distribution, see **Figure 8.11b**. However, a totally uniform Cu

dispersion ($G = 0$) would require an infinite amount of time and thus a non-uniform phase distribution ($G > 0$) is inevitable. Even so, adjustments made to the homogenization treatment would help lower the possibility of AGG by decreasing the amplitude of the non-random particle distribution.

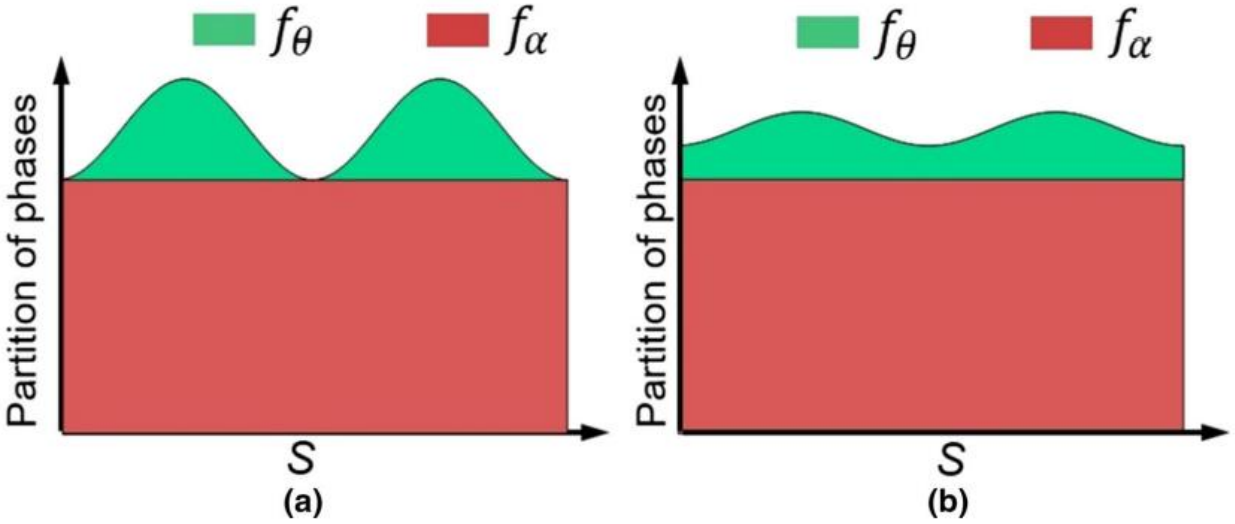

Figure 8.11. Influence of homogenization time on θ-Al_2Cu phase distribution. (*a*, *b*) Schematic partitioning of θ-Al_2Cu and α-Al phase after relatively short and long homogenization treatments and further annealing.

6.4. Conclusions

In this work, we investigate the evolution of second phase particles and their role in provoking abnormal grain growth (AGG) in Al-3.5wt%Cu alloy. To uncover the connection between the particles and the grains, we map the θ-Al_2Cu particle distributions and grain growth behaviors as a function of annealing temperature and time. We use the Gini coefficient G to quantify and compare the inhomogeneity of particle distributions across the various annealing states. At relatively high temperatures (but below the solvus) and at long annealing times, we observe a highly non-random particle distribution ($G > 0.2 - 0.3$) and a concomitant AGG. With

this information, we construct a temperature-time-(structural) transformation (TTT) diagram that can be used by researchers to anticipate the grain growth behavior at a given annealing state.

To rationalize the above trends, we determine the source of the non-random particle distribution to be residual Cu segregation after homogenization. That is, the spatial fluctuations in Cu and/or θ-Al_2Cu are amplified at elevated temperature and upon prolonged annealing. The insights gained can be used to predict the onset of AGG by monitoring the Gini coefficient associated with the particle distribution. Based on our analysis, we propose a few strategies to decrease G and thus mitigate the occurrence of AGG.

Chapter 9. Percolation Behavior of Three-dimensional Grain Boundary Networks

This chapter is based on the article in peer review as of August 2022 [83], for which I retain the right to include it in this dissertation, provided it is not published commercially. The co-authors are Konnor Walter, Hrishikesh Bale, and Ashwin J. Shahani. This work was supported by the Army Research Office Young Investigator Program under award no. W911NF-18-1-0162.

9.1. Introduction

As early as 1948, C.S. Smith defined the topology of the materials world [44]. Solid materials like polycrystalline metals can be partitioned into space-filling grains with faces (*grain boundaries* or GBs), edges (*triple junctions* or TJs) and vertices (*quadruple nodes* or QNs), see also **Chapter 3**. For topologically stable 3D structures, Smith showed that three GBs meet at a TJ edge and four TJs meet at a QN. The importance of such planar and linear defects on materials performance is worth reviewing, below.

GBs in a polycrystal provide faster diffusion paths (orders of magnitude greater diffusivities) compared to the intragranular lattice, due to the excess free volume and enhanced atomic mobility [174–176]. The distribution and character of GBs have long been known to play a critical role in many intergranular failure events, including corrosion [14,58,59,177–179], cracking [16,180–183], and liquid metal embrittlement [20,21]. For example, low-angle GBs tend to be less susceptible to grain boundary sliding [184] and coincidence-site lattice (CSL) GBs have shown a resistivity to crack propagation [185]. Consequently, the field of grain boundary engineering has sought to prevent those intergranular failure events by increasing the density of

failure-resistant GBs. On the other hand, it has been consistently claimed that susceptibility to failure depends not only on the *identity* of individual GBs, but also the *connectivity* between them [14–19]. Damage accumulates in a material when a connected pathway of failure-susceptible (*i.e.*, sensitized) GBs span the material. A detailed understanding of the underlying structure of the GB network is therefore warranted.

To this end, bond percolation describes the behavior of a large system, the elements of which are randomly interconnected *via* bonds [62,63]. Since it provides a natural description of connectivity, the network of GBs can be analyzed within the framework of bond percolation theory wherein the 'bonds' represent the GBs. Some bonds are 'open' (or failure-susceptible, in this case) while others are 'closed' (or failure-resistant and immune). At a critical fraction of open bonds, termed the percolation threshold, there exists a continuous path of open bonds that travels infinitely far. Stated differently, the percolation threshold is the bond occupancy at which the network connectivity changes from short- to long-range [186]. Wells and coworkers [187] were the first to investigate the complex structures and percolation thresholds of synthetic, 3D GB networks. More recently, Schuh and coworkers modelled the grains as space-filling tetrakaidecahedra and compared their results on the connectivity of GBs against standard percolation theory [64–66]. Ultimately, they found that the GB network can be characterized using the same scaling laws and critical exponents as of percolation theory, *i.e.*, it is in the same universality class as random percolation. Even so, the percolation threshold is system-specific and dependent on the underlying topology of the GB network [64]. It is thus an open question if the percolation threshold measured by Schuh and coworkers on an ensemble of 14-sided grains is necessarily relevant to real materials that possess a broad distribution of grain topologies (*vide infra*). In fact, prototypical shapes like Kelvin's tetrakaidekahedra and the Weaire-Phelan cell are rarely observed [188]. To the best of

our knowledge, there have been no direct tests to confirm the results of their idealized simulations nor any other idealized model studies using different space-filling polyhedrons.

Damage can propagate in a 3D polycrystal not only along the GBs, but also along the three-grain intersection lines, or TJs. Such linear defects are diffusional short-circuits even with respect to the GBs [189–191]. The influence of TJ diffusion becomes increasingly evident in nanomaterials where the density of TJs per unit volume is substantial. Many studies reported unusually high grain boundary diffusivity for nanocrystalline materials compared to conventional grain boundary diffusivity [68–73], and Chen and Schuh quantitatively explained the anomaly by accounting for the high diffusivity of TJs [74]. It stands to reason, then, that the TJ lines are the key network-forming elements of the bond percolation problem. However, we have limited understanding of TJ network and its connectivity in real 3D materials, aside from some preliminary remarks in Ref. [192]. It remains to be determined how the percolation threshold of TJs relates to that of the GBs and also to idealized lattice structures [67].

These questions remain unanswered *via* experiment due to the dearth of (i) *3D* and (ii) *large-scale* microstructural data. Firstly, since percolation is a measure of connectivity, the percolation threshold varies with the dimensionality of the system [61–63]. As Ref. [186] explains, in 2D the formation of a percolating cluster of GBs (or TJs) blocks the spanning of any other cluster, while in 3D a cluster may "go around" a spanning cluster and simultaneous percolation is achievable. Secondly, smaller datasets will intuitively lead to artificially lower percolation thresholds than that of an infinite system, as noted also by Ref. [193]. For these two reasons, measuring percolation thresholds by microscopy on limited fields-of-view is an ineffectual pursuit.

Motivated by new developments in non-destructive, high-throughput laboratory-based materials characterization, we analyze 3D microstructure in the lens of percolation theory.

Specifically, we probe *via* X-ray diffraction-contrast tomography (LabDCT) a total of 1,869 grains and 10,265 GBs in an Al-3.5wt%Cu alloy as a model system. Recent developments in crystallographic grain reconstructions and advanced adaptive scanning modes for large volume scanning within the LabDCT module provide unprecedented access to the location, shape, and crystallography of these features within large samples with true sample representativeness. Optimizations of reconstruction algorithms permit mapping massive volumes for significantly larger grain statistics in reasonable timeframes without the need of demanding computational resources.[4] The large-scale 3D microstructure and the scaling laws of random percolation enable us to quantify the percolation threshold in the limit of an infinite GB network size and compare to theory. We find self-consistent percolation thresholds using different metrics. We further confirm agreement between the results from our 3D experiments and those from simulations by Schuh and coworkers [66] if grain topology is normalized. In addition, we investigate percolation of TJs for the first time and further compare to that of GBs as well as idealized lattice structures. We identify the origin of discrepancy between TJ and GB connectivity from a specific type of isomerism of QN. We show that there exists also a significant difference between the TJ network and the idealized diamond lattice that is explained by a spatial correlation of TJs and a hyper-coordination of nodes. These results force a reconsideration of some long-standing assumptions while validating others regarding the percolation behavior of polycrystalline materials.

[4] For example, the volume reconstruction of ~2000 grains takes about three days on a Windows workstation with 128GB RAM, Dual Intel Xeon Silver 4114, 2.2 GHz processors with 40 cores.

9.2. Experimental Methods

9.2.1. Sample Preparation

Broadly, our experimental procedure follows that of Refs. [80,81], described already in **Chapters 7**. An ingot of composition Al-3.5wt%Cu was cast *via* vacuum arc remelting at Ames Laboratory (Ames, IA, USA), using high-purity Al (99.999%) and Cu (99.997%). After homogenization at 550 °C for four hours, the sample was subject to cold rolling to reduce its thickness by 50 %. Then, it was annealed at 400 °C for 30 min. These treatments resulted in a fully recrystallized microstructure, but not necessarily a steady-state configuration of grains (*vide infra*). The specimen was prepared into a rectangular shape ($1 \times 2 \times 6$ mm) by electric discharge machining for 3D X-ray imaging in the laboratory.

9.2.2. Data Acquisition

After cutting it to size, the specimen was imaged using the Diffraction Contrast Tomography module (LabDCT) on a laboratory X-ray microscope (ZEISS Xradia 620 Versa with LabDCT Pro). The entire sample was scanned by rastering a small X-ray illumination area (achieved using a fine 250 µm × 750 µm aperture) over the large sample. The acquisition sequence is user selectable to suit the sample geometry and consists of moving the sample position (x, y, z) and rotation (θ) stages in fine increments after acquiring diffraction patterns at each position using the flat panel detector of the X-ray microscope. For the current sample the helical phyllotaxis acquisition mode was used which is best suited for smaller 'matchstick' sized samples. A total of 8500 raw diffraction images were collected with an exposure time of 25 s per projection to cover the entire sample. Thus, the entire data acquisition took approximately a few days. The source-to-sample and sample-to-detector distances were 14 mm and 425 mm respectively producing a projection geometry for acquisition of diffraction data.

9.2.3. Data Processing

We reconstructed the X-ray images into a 3D crystallographic microstructure using the grain reconstruction software (GrainMapper3D version 3.1, Xnovo Technology ApS, Koge, Denmark), described elsewhere [80,81,87]. The reconstructed microstructure was further filtered and analyzed using *PolyProc* freeware [80], a MATLAB-based modular data processing framework for 3D x-ray diffraction (3DXRD) data **(Chapter 6)**. In this work, we utilize mainly the grain clean-up routine therein. Namely, we cluster into grains provided they have misorientation less than 1°. Following this procedure, we screen the remaining grains and digitally remove the ones we deem unreliable if they are under the thresholds completeness (0.2). Details on our data processing pipeline can be found in Ref. [80] - **(Chapter 6)**. We further excluded the outer-most regions of the sample since it contains un-indexed 'voids' after the clean-up routine, thereby disturbing the connectivity of GBs. The final 3D microstructure contains 1,869 grains and 10,265 GBs, as mentioned previously.

To invoke percolation theory, we require a binary classification of grain boundaries (*e.g.*, open or closed bonds in the classical description of bond percolation). Gertsman and Tangri have shown that there is no loss of generality in dividing the GBs into two categories when considering their propensity to failure [16], which justifies the following binary classification. That is, we label GBs in the processed LabDCT reconstruction as either high-angle random (HAR) or non-HAR, the latter of which includes low-angle random (LAR) and coincident site lattice (CSL) boundaries. In general, HAR boundaries are less ordered than non-HAR boundaries and therefore possess higher GB energies [1,40,194,195]. It follows that they are generally more susceptible to failure by, *e.g.*, liquid metal embrittlement [21,101]. To distinguish between the two classes of GBs, we use a generalization of the Brandon criterion [76]

$$\Delta\theta_{max} = \theta_0 \Sigma^{-n} \quad \textbf{(Equation 9.1)}$$

where $\Delta\theta_{max}$ is an allowable angular deviation to a given CSL type (characterized by Σ number) and $\theta_0 = 15°$ is a constant of angular limit for low-angle or $\Sigma = 1$ GBs. We examine only $\Sigma \leq 49$. Historically, n can take on different values such as $\frac{1}{2}$ [76], $\frac{2}{3}$ [77], $\frac{5}{6}$ [78], or 1 [79]. In this work, we treat n as an adjustable parameter. The greater the value of n the more restrictive the criterion for CSL in **Equation 9.1**, and hence the higher the number fraction p of HAR GBs in the microstructure and also the more likely it is that the HAR GBs percolate. **Figure 9.1** plots n against p for a subvolume of the sample so considered. Bearing this relationship in mind, our procedure is as follows: For a given value of n, we identify the largest cluster of HAR GBs. We compute the order parameter, P, defined as the number fraction of HAR boundaries that belong to this cluster. We also check to see if the system percolates, *i.e.*, whether the largest cluster of HAR GBs spans the imaged FOV in one or all three principal directions. We then repeat our calculations for different values of $n \in [0,1]$. The procedure allows to investigate how the network of HAR GBs evolves with just a single 3D dataset. Ref. [193] use a similar approach, albeit for a 2D dataset.

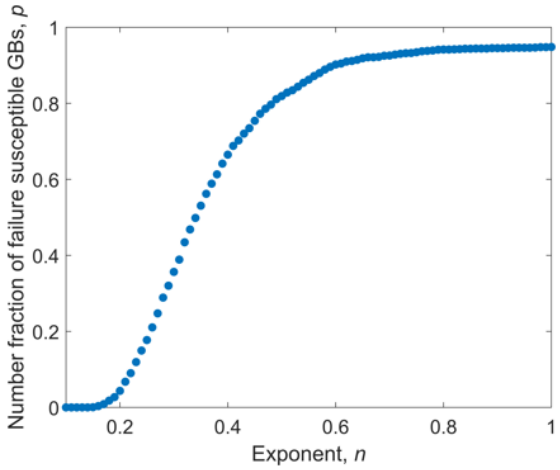

Figure 9.1. Illustration of relationship between exponent, *n*, and the number fraction of HAR GBs, *p*.

Figure 9.2 illustrates how P increases upon increasing the concentration (by number) of HAR boundaries, p, in one of the largest cubic-shaped subvolumes (side length of 600 μm) out of the entire reconstructed microstructure. The inset images provide a few 3D snapshots of the largest connected cluster of HAR boundaries in the sample (see opaque orange colors) and its evolution with p. It is only until p reaches ~0.2 that P starts to rise significantly. The inset image corresponding to the datapoint $p = 0.29$ illustrates how the largest connected cluster of HAR boundaries spans or percolates all three principal directions. We also observe that p never reaches a value of 1, but rather terminates at ~0.95. This is because the microstructure contains a non-negligible number fraction (0.05) of LAR GBs. Such GBs have a misorientation angle below 15° and are thus non-HAR boundaries regardless of the exponent n in **Equation 9.1**. We note that this observation stands for other figures with p in the abscissa. The critical (denoted with a c in subscript) value of $p_c = 0.29$ obtained here for percolation of HAR GBs in all three directions does not represent an intrinsic percolation threshold as percolation is defined on an infinite lattice.

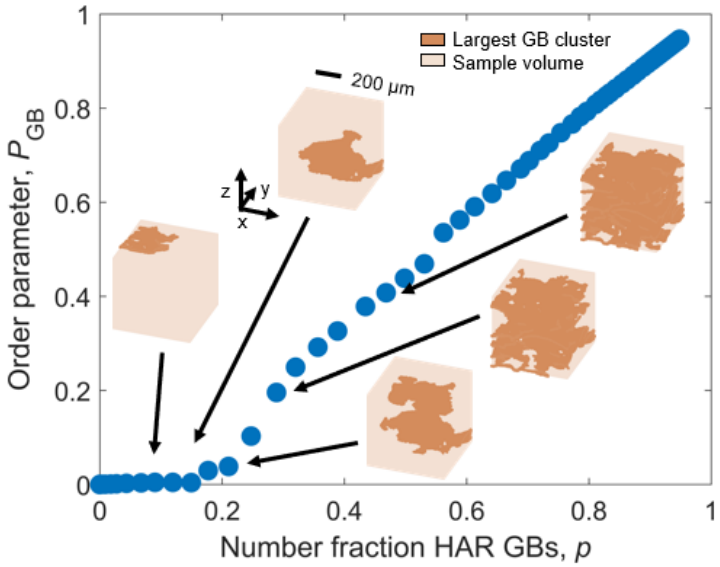

Figure 9.2. The order parameter, P, versus the number fraction of failure-susceptible or open grain boundaries, p. Insets illustrate 3D microstructures in translucent orange color with the largest connected cluster of HAR GBs in opaque orange color, at designated values of p.

9.2.4. Key Functions of Percolation Theory

Finite-size scaling allows us to circumvent the limitation of a finite sample size by computing an intrinsic percolation threshold p_c from measured quantities as a function of sample size L [61,62]. In this work, we utilize two functions for scaling analysis. The first is the order parameter P (defined previously), which scales with L at the percolation threshold $p = p_c$ as

$$P(p_c, L) \propto L^{-\frac{\beta}{\nu}} \quad \textbf{(Equation 9.2)}$$

where β and ν are critical exponents that depend only on the dimensionality of the system; in 3D, they are 0.418 and 0.876, respectively [61]. It should be emphasized that Frary and Schuh have already demonstrated the suitability of these universal constants on grain boundary networks [64]. On a plot of $\ln P$ versus $\ln L$, then, the above function is linear with a slope $n(L)$, given by

$$n(L) = \frac{d(\ln P)}{d(\ln L)}\Big|_{p_c} = -\frac{\beta}{\nu} \quad \textbf{(Equation 9.3)}$$

Therefore, the percolation threshold in the infinite or thermodynamic limit can be found by determining at which value of p the slope $n(L)$ attains a value of $-\frac{\beta}{\nu} = -0.477$.

The second function of relevance here is the percolation probability (so-called crossing probability [196,197]), Π, defined as the probability of percolation across a sample in all three principal directions ($\Pi^{(3)}$). This definition prevents any potential bias caused by anisotropic grain shapes. For an infinitely large sample, Π is a step function with $\Pi(p < p_c) = 0$ and $\Pi(p > p_c) = 1$. On the other hand, for finite-sized samples, the step is diffuse and Π behaves instead as an 'S-shaped' curve with an inflection point [198], as Π now becomes the fraction of percolating subvolumes (described below) in an ensemble at a particular value of p. The point of inflection, denoted p_{max}, where the change in Π with p is maximum, converges to p_c as

$$(p_{max} - p_c) \propto L^{-\frac{1}{\nu}}$$ (**Equation 9.4**)

Likewise, the parameter p_{av}, which represents here the average fraction of HAR GBs in the largest connected cluster that completes a percolation path for the first time, is defined as

$$p_{av} = \int_0^1 p(\frac{d\Pi}{dp})dp$$ (**Equation 9.5**)

The scaling of p_{av} is similar to p_{max}, *i.e.*,

$$(p_{av} - p_c) \propto L^{-\frac{1}{\nu}}$$ (**Equation 9.6**)

To carry out a scaling analysis, we divided the entire imaged FOV into ensembles of cubic subvolumes with side length $L = 3, 4, 5, \ldots 10$ (in units of multiples of the mean grain size, 60 μm, expressed as an equivalent diameter). Each subvolume is unique in the sense that there are no overlaps with neighboring subvolumes; they also contain at least three grains ($L \geq 3$) with less than 5% of free space (un-indexed voxels). From each ensemble of subvolumes at a given p, we determined the two parameters P and Π. To improve the resolution of the latter, we fit the discrete data-points to a smooth, 'S'-shaped curve with an inflection point p_{max} [198],

$$\Pi(p) = 1 - \left[1 + \exp\left(\frac{p - p_{max}}{\alpha}\right)\right]^{-1}$$ (**Equation 9.7**)

where α is a fitting parameter that determines the width of the step in $\Pi(p)$.

9.3. Results and Discussion

9.3.1. Characterization of GBs, TJs, and QNs

We first characterize the microstructure of the 3D sample, visualized in its entirety in **Figure 9.3**. Grains are rendered semi-opaque in order to peer into the network of GBs and colored based on their crystallographic orientations with respect to the specimen $\hat{z}$ direction. As the texture of the microstructure is known to influence the extent of crystallographic constraints at both triple junctions (*e.g.*, combination rule, a first-order constraint) and quadruple nodes (a second-order

constraint), and hence also the percolation behavior [66,199–201], we examine first the orientation distribution function. From the inverse pole figure shown in **Figure 9.3**, there is weak texture in the microstructure, as we would also predict from past reports [49,81].

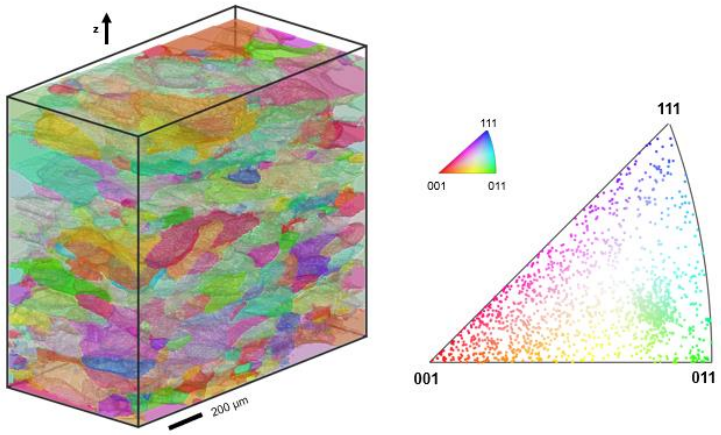

Figure 9.3. LabDCT reconstruction of the full sample with microtexture analysis using an inverse pole figure with respect to the specimen $\hat{z}$ axis. Grains are plotted translucently to reveal GBs. The colors of grains represent crystallographic orientations with respect to the specimen $\hat{z}$ direction (see inset coordinate system and corresponding standard triangle). Each data point on the inverse pole figure is a grain that is colored using the standard triangle shown in the standard triangle inset.

Next, we analyze the topology of the GB network by obtaining statistics on the numbers of first nearest neighbors of each grain, see **Figure. 9.4**. We do so by building a region adjacency graph [87] of the grain map in order to find a set of neighbors of each grain within the sample. Only interior grains are considered here because grains on the free surfaces of the sample can deflate the nearest neighbor statistics. Our analysis reveals an average of 12.10 nearest neighbors per interior grain. We corroborate our result against other computational [202–204], experimental [36,205–210], and analytical [211] studies, all of which show a qualitatively similar behavior in distribution of grain neighbors (**Table 9.1**). This similarity may be understood by noting that the grain size distribution is usually log-normal [29,36,207,210]. It follows that the grain topology, which is strongly correlated to the grain size through the Lewis law [50], can be described with the *same* log-normal distribution. Clearly, a lattice wherein each grain has exactly 14 neighbors

does not exist in reality. Despite the similarity in general shape of the distribution, our result shows a greater skewness (mode skewness of 0.81 *vs.* 0.07 for Ref. [211]). This can be an indication that our sample has not reached a steady-state growth phase as mentioned previously; rather, it is still in transient period that precedes normal grain growth [202,203].

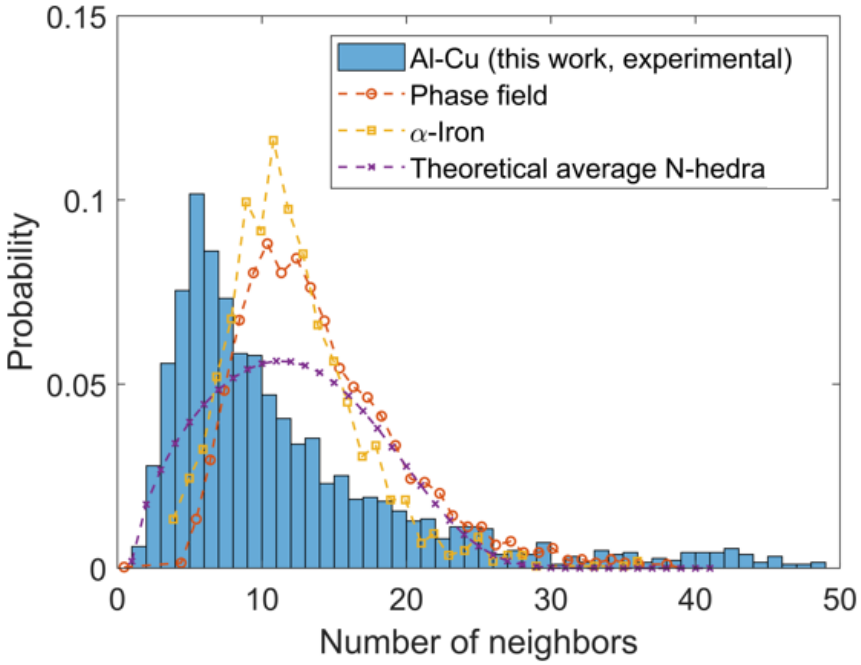

Figure 9.4. Distribution of the number of nearest neighbor grains (or faces) per interior grain obtained from our experimental microstructure. Superimposed are distributions from different simulated [204], experimental [206], and analytical [211] microstructures for comparison.

Table 9.1. Average number of nearest neighbors of various 3D microstructures.

	Nearest neighbors	**Reference**
Theoretical microstructure		
Average N-hedra	11.98	[211]
3D experimental microstructure		
Al-Cu	12.10 (±6.67)	this work
α Fe	12.1-12.8	[207,210]
β Cu-Zn	11.8	[206]
α Ti	14.2	[208]
β Ti	13.7	[36]
IN100 alloy	12.9	[209]
316L alloy	9.5-11.2	[205]
Simulated microstructure		
Phase field	13.7	[204]
Surface evolver	13.5	[202]
Monte Carlo	12.85	[203]

We turn our attention to linear defects, namely the TJs that are formed by the intersection of three GBs in 3D space. In practice, we identify them directly from the region adjacency graph. TJs realize four different types based on the number of failure-susceptible, HAR GBs that meet at the TJ. Following Ref. [66], the notation J_i indicates a TJ consisting of $0 \leq i \leq 3$ HAR GBs. We characterize the triple junction distribution (TJD), which illustrates the number fraction of different TJs with respect to the number fraction of failure-susceptible HAR GBs, p, in one of the largest cubic-shaped subvolumes, see **Figure 9.5**. The subvolume contains 428 grains, 2,122 GBs, and 3,930 TJs. The reason for investigating a subvolume instead of the entire microstructure is to employ the same criterion of TJ percolation (clusters spanning all three principal directions) for fair comparison with GB percolation, in a later discussion. As was alluded to previously, crystallographic, first-order constraints are known to influence the TJD by maintaining consistency of grain orientations around the TJ [199–201]. Yet in our case, the TJD shows good agreement to a random assignment of GBs, which can be calculated using the Bernoulli distribution as

$$J_i = \binom{3}{i} p^i (1-p)^{3-i} \qquad \textbf{(Equation 9.8)}$$

The compliance of our data with **Equation 9.8** indicates a weak influence of first-order crystallographic constraints on the shape of the TJD. From the four different types of TJs depicted in **Figure 9.5**, we combine them into two groups in order to investigate percolation behavior of TJ network (**Sec. 9.2.3**). As an *ansatz*, we take TJs of character J_0 to be "closed" bonds, and those TJs with at least one failure-susceptible HAR GBs (J_1, J_2, and J_3) to be "open" bonds available for percolation.

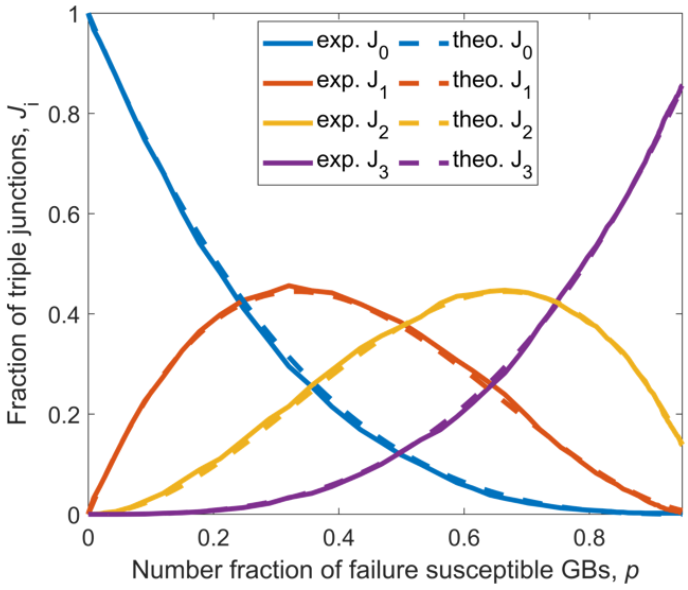

Figure 9.5. The triple junction distribution (TJD) for the experimental microstructure (solid line) compared to that predicted by a random assemblage of GBs (**Equation 9.8**, dashed line).

QNs are points in 3D space where four grains, six GBs, and four TJs meet. **Figure 9.6** shows a schematic of an idealized QN in 3D space with four different grains labeled as G_i ($i = 1, 2, 3$ and 4), and a corresponding topological map [66]. The latter is an illustration of the QN topology, wherein the lines represent GBs, and the vertices represent TJs. To illustrate how the microstructure can be represented by such a map, examples of a GB and a TJ are colored correspondingly: that is, a GB between G_2 and G_3 is colored in green and a TJ by G_1, G_3, and G_4

is colored in red in both **Figure 9.6a-b**. In what follows, thick lines indicate open GBs and thin ones the converse.

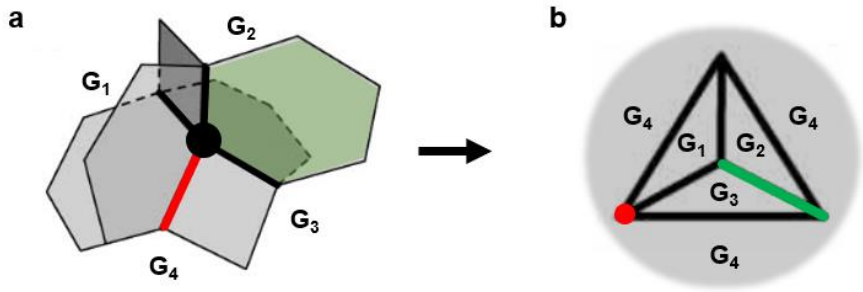

Figure 9.6. (a) Schematic of an idealized QN with six associated GBs (gray faces) and four associated TJs (bold lines) in 3D. (b) Topological map of the same QN. One matching GB and TJ are colored in red and green, respectively. Reprinted and adapted with permission from [66].

These point defects can be distinguished based on the number of failure-susceptible (HAR) GBs and open ($J_1, J_2,$ and J_3) TJs. We note that, unlike TJs, classification of QNs must involve two criteria, namely, the composition of GBs and TJs, to differentiate configurational isomers that QNs exhibit [66]. The notation Q_{ij} (adapted from Ref. [66]) accounts for both effects and completely specifies the identity of the QN, where the first index $0 \leq i \leq 6$ refers to the number of open or failure-susceptible GBs and the second index $0 \leq j \leq 4$ to the number of open TJs. By this definition, the nine unique types of QNs are shown *via* topological maps in the insets of **Figure 9.7**. For each, we examine at the outset the quadruple node distribution (QND), which specifies the number fraction of the given QN with respect to the number fraction of failure-susceptible GBs, p, for the same cubic-shaped subvolume analyzed above. The influence of crystallographic constraints is known to extend to the QND [66]. That said, we find a good agreement of the experimentally assessed QNDs to random assignment of GBs, which can be calculated as

$$Q_{ij} = \Omega_{ij}\, p^i (1-p)^{6-i} \qquad \textbf{(Equation 9.9)}$$

where Ω_{ij} is the number of configurational isomers for each QN, which we find to be 1, 6, 12, 3, 4, 16, 15, 6, and 1 for Ω_{00}, Ω_{12}, Ω_{23}, Ω_{24}, Ω_{33}, Ω_{34}, Ω_{44}, Ω_{54}, and Ω_{66}, respectively. Ultimately, second-order crystallographic constraints only weakly impact the QNDs in this study.

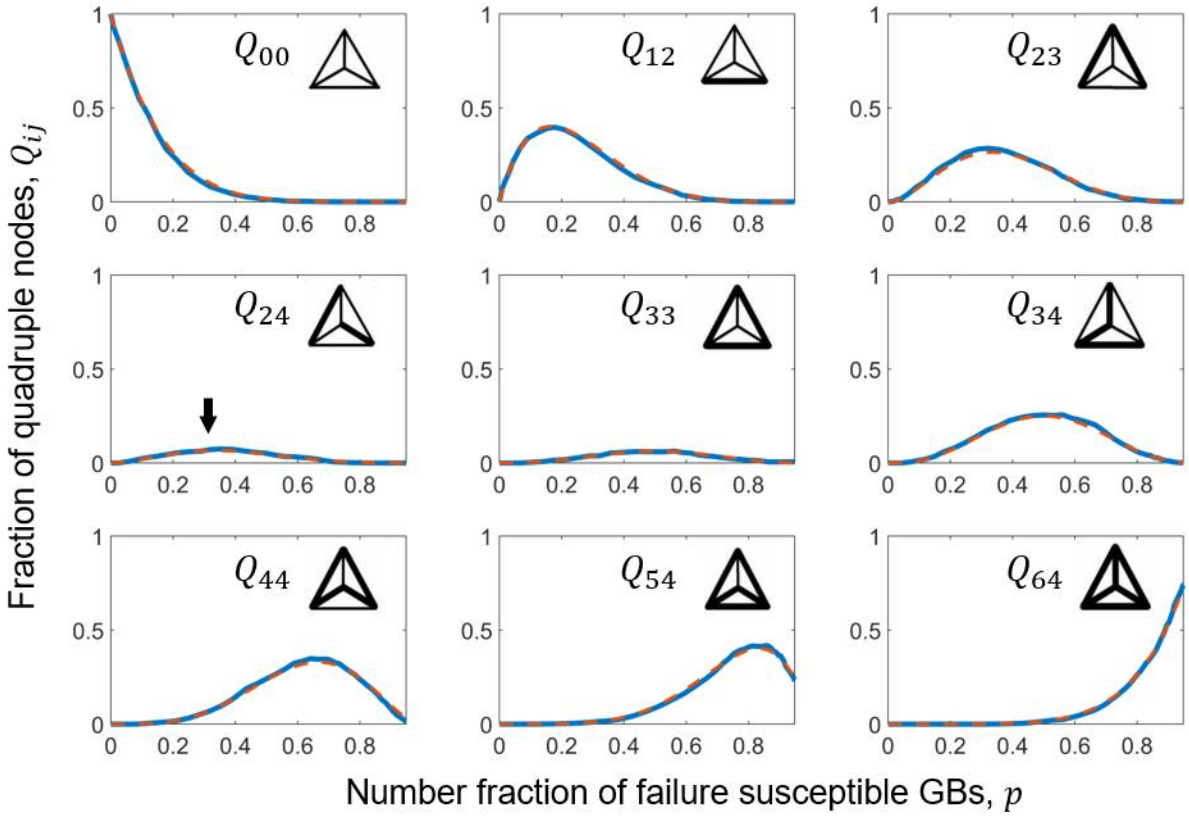

Figure 9.7. The quadruple node distribution (QND) for the experimental microstructure (solid line) compared to that predicted by a random assemblage of GBs (**Equation 9.9**, dashed line). Topological diagrams are shown inset for the nine unique types of QNs, denoted Q_{ij}.

9.3.2. Calculation of GB p_c and Comparison to Simulation

In **Figure 9.8**, we plot the ensemble-averaged $P(p, L)$ over all subvolumes as a function of p. As expected, we observe a slower increase in $P(p, L)$ with increasing L in low p region, see inset. This is because the formation of a connected cluster of HAR GBs becomes easier for smaller L. Using the data in **Figure 9.8a**, we plot $n(L)$ in order to estimate p_c *via* **Equation 9.3**, see blue

curve in **Figure 9.8b**. The grey-colored band bounded by dotted line represents the connection of error bars from each data point. Linear interpolation allows us to estimate p_c of the GB network as 0.222 (0.162, 0.273), at which point the bold line at $-\frac{\beta}{\nu} = -0.477$ intersects the blue $n(L)$ curve. Relatively large errors are expected for low p as the calculation of $n(L)$ is more readily perturbed by outliers.

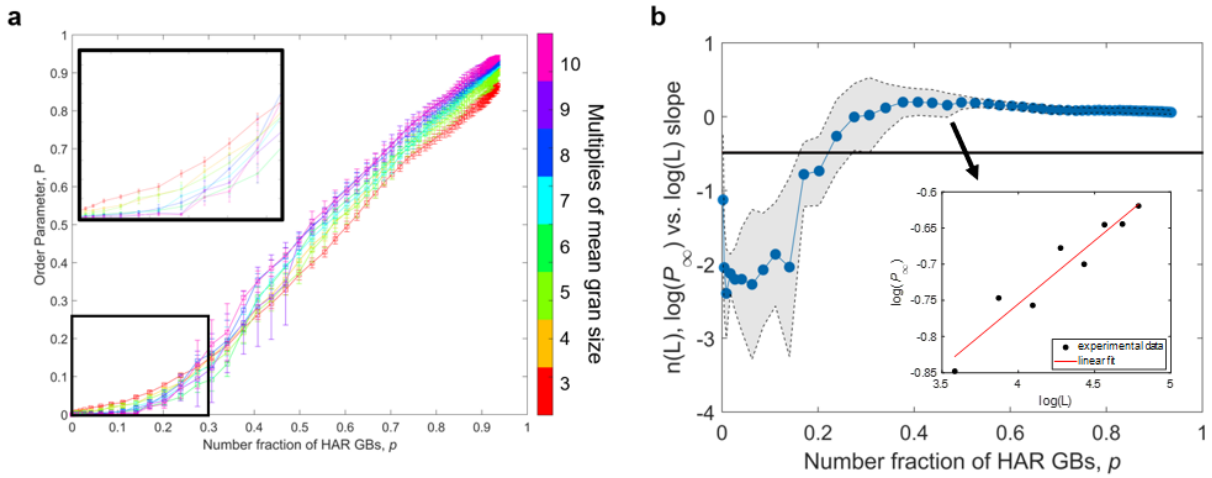

Figure 9.8. Order parameter, P, and estimated value of percolation threshold, p_c. (a) Ensemble averaged $P(p, L)$ from subvolumes with weighted average error bar. Errors reflect standard deviation in P from multiple subvolumes. Inset illustrates an enlarged plot of low p region. (b) Estimation of p_c derived from the power law scaling of P, according to **Equation 9.3**. Blue curve represents change in $n(L)$ based on data presented in (a). See inset of (b) for the calculation of a single n value (arrow). Grey colored band bounded by dotted line represents the connection of error bars from each data point. Black horizontal line represents $n(L) = -\frac{\beta}{\nu} = -0.477$.

In **Figure 9.9**, we fit **Equation 9.7** to the ensemble averaged $\Pi(p, L)$, by assessing the presence of a percolating pathway in each subvolume. Of note is that error bars are absent here because $\Pi(p, L)$ for each subvolume is either 0 (not percolating) or 1 (percolating). In an ideal lattice, plots of $\Pi(p, L)$ versus p for different domain sizes L should share a common intersection point at p_c [196,197,212]. However, we observe here a spread of the intersection points in the range of 0.25 to 0.4. This is mainly due to the finite size of the 3D dataset. Nevertheless, from

these $\Pi(p, \mathrm{L})$ curves, we calculate p_{max} and p_{av} and plot them against $L^{-\frac{1}{\nu}}$, see **Figure 9.9b-c**. The red lines represent a linear interpolation of points with 95% confidence interval (grey colored region). From the scaling relations in **Equations. 9.4 & 9.6**, p_c can be found when $L^{-\frac{1}{\nu}}$ approaches to 0 or $L \to \infty$. We find p_c of 0.200 ± 0.072 and 0.287 ± 0.068 from **Figure 9.9b-c**, respectively.

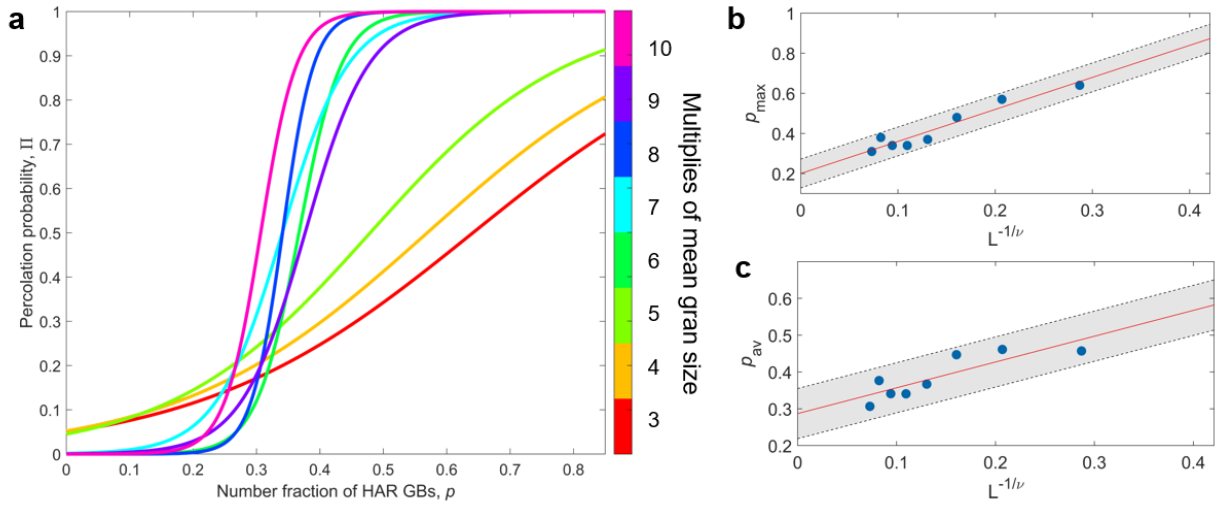

Figure 9.9. Percolation probability, Π, and estimated value of percolation threshold, p_c. (a) Fitted curve of ensemble averaged $\Pi(p, L)$ from subvolumes, see also **Equation 9.7**. (b-c) Estimation of p_c derived from the finite scaling of (b) p_{max} (**Equation 9.4**) and (c) p_{av} (**Equation 9.6**) with respect to $L^{-1/\nu}$ where L is in units of multiples of mean grain size. The red lines represent a linear interpolation of points with 95% confidence interval (grey band bounded by dotted line). Intercepts with the ordinate give p_c from (b) p_{max} (0.200 ± 0.072) and (c) p_{av} (0.287 ± 0.068).

Table 9.2 summarizes three estimates of p_c from the different parameters and their scaling laws. As these three values are all based on valid scaling relations with no superiority, we take the average of them and propagate errors to obtain $p_c = 0.236 \pm 0.039$. This value represents the percolation threshold of an infinite GB network. To confirm whether our p_c is reasonable, we compare it to simulation [66]. From their system of tetrakaidekahedral grains, they found $p_c = 0.225$ with deviation of about 0.07 depending on the crystallographic texture. Of note is that this value of p_c is within the standard deviation of our experimentally measured p_c value.

Table 9.2. GB percolation thresholds, p_c, from different 3D microstructures and methods. For the simulated microstructure, p_c from Ref. [66] is further normalized based on a procedure used in Ref. [213], as further elaborated on in the main text. For our experimental microstructure, p_c is estimated from different parameters and their scaling laws.

Analysis method	**Percolation threshold (p_c)**	**Reference**
Theoretical microstructure		
Tetrakaidecahedra	0.225	[66]
Normalized by nearest neighbors	0.220	[213]
3D experimental microstructure		
Finite-size scaling – averaged	0.236 (0.197,0.275)	this work
Finite-size scaling – order parameter	0.222 (0.162, 0.273)	this work
Finite-size scaling – p_{max}	0.200 (0.129, 0.272)	this work
Finite-size scaling – p_{av}	0.287 (0.219, 0.355)	this work

Even so, direct comparison between the two measurements is not fair since the topological characteristics are different. Recall that our experimental dataset shows a wide and skewed distribution of nearest neighbor grains (**Figure 9.4**), whereas the synthetic microstructure by the Frary and Schuh [64] would show a Dirac delta function at 14 nearest grains. To bring the simulation result closer to experiment, we employ the topological correction suggested by Fullwood and coworkers [213]. That is, we must add, on average, $14.33 - 14 = 0.33$ HAR GBs per grain, where 14.33 is again the average number of grain neighbors in the experimental dataset (**Figure 9.4**). This would represent a number fraction of $\frac{0.33}{14} = 0.024$ HAR GBs in the simulated microstructure that should further contribute to the percolation process. Consequently, we would expect that $\frac{0.225}{1+0.024} = 0.220$ of the remaining bonds are open to arrive at the percolation threshold, following the same logic in Ref. [213]. This value still shows consistent agreement with our experimental estimation of p_c. Intuitively, percolation is made more easier if we increase the number of grain neighbors as there are greater number of HAR GB pathways that span the system. Of note is that we conducted the same exercise with a Poisson-Voronoi microstructure and confirmed a higher percolation threshold compared to our experimental results (even *after*

normalization). Intuitively, the disagreement makes sense as the Poisson-Voronoi structure corresponds to the nucleation of recrystallization [214], not grain growth.

Based on the preceding analysis, we postulate that the *average* grain topology plays critical role on the percolation threshold of the GB network. Nevertheless, we should caution that the experimental microstructure considered here have a relatively weak crystallographic texture and an approximately log-normal distribution of grain size. We leave for future work the 3D assessment of other types of granular microstructures (*e.g.*, those with a strong texture and/or bimodal distribution of grain size, characteristic of abnormal grain growth [81,215]).

9.3.3. Comparison of GB and Trijunction p_c

Next, we seek to identify the relationship between GB and trijunction percolation behaviors. As such, we investigate the connectivity of triple junctions (TJs) in one of the largest cubic-shaped subvolumes instead of the entire microstructure; this is to leverage the same criterion for percolation (spanning all three principal directions, as described in **Sec. 9.2.4**), so that we can make an impartial comparison between GB and TJ connectivities. We analyze this same subvolume in the following analysis, with attention to the TJ network. Within the subvolume, we observed the structure of the TJ network as we vary the number fraction of failure-susceptible GBs, p, just as we did for the GB connectivity analysis (*cf.* **Sec. 9.3.3**). To ensure the connectivity of TJs that are separated by around one voxel due to experimental uncertainty in LabDCT, we performed a morphological closing operation [86] on the TJ network.[5]

Figure 9.10 illustrates the evolution of TJ connectivity upon increasing the number fraction of failure-susceptible GBs (the effect of which is to "open" TJs accordingly; see upper and lower

[5] If we assume a binary classification of TJs (open and closed, see **Sec. 9.3.1**), the connectivity of GBs must entail that of TJs since a HAGB maintains at least J_1 along its perimeter. Thus, empirically, we confirm that the *minimum-sized* structuring element that guarantees TJ connectivity along with the GB connectivity to be a cube of $3 \times 3 \times 3$ voxels.

labels of abscissa on **Figure 9.10** for the explicit relationship between the number fractions of open GBs and open TJs). Similar to **Figure 9.2**, the inset images provide a few 3D snapshots of the largest connected cluster of open TJs at various p values. Starting from the first inset image corresponding to a low fraction of failure-susceptible GBs, we clearly observe the formation of open TJ rings or loops since all TJs must open along the perimeter of a HAR GB. This particular topological structure will be discussed later. For now, we can see that the TJs percolate for a particular number fraction of failure-susceptible GBs, p_c = 0.247 (the third inset image), which is a lower threshold compared to GB percolation p_c = 0.289 (again, for the same subvolume so considered). While the order parameter, P, becomes almost linear after percolation in **Figure 9.2**, here in **Figure 9.10** the number fraction of open TJs in the largest cluster plateaus after reaching percolation. This is because all possible TJs in the network open *before* all possible GBs become failure susceptible.

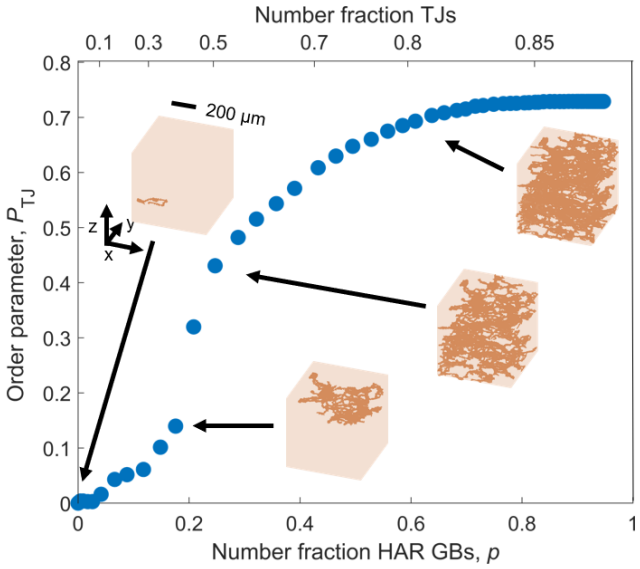

Figure 9.10. The number fraction of open TJs in the largest connected cluster *versus* the number fraction of failure susceptible grain boundaries, p (bottom abscissa) and the number fraction of open TJs, p' (top abscissa). Insets illustrate the microstructural domain in a translucent orange color with the largest connected cluster of open TJs in opaque orange color.

To investigate in detail the source of the difference between TJ and GB connectivity, we plot connected clusters of GBs at the GB percolation threshold (which, in terms of the number fraction of failure susceptible GBs, is p = 0.289) together with connected clusters of TJs at the same p value, see **Figure 9.11a**. The network of percolating GBs (in green) does not match that of the percolating TJs (in red). Namely, the latter spreads into regions of the domain that consist of non-percolating GBs (in teal). See, for example, the black-boxed region, which is magnified in **Figure 9.11b**. Where the open TJ cluster extends beyond the open GB cluster, we find the root of this discrepancy to be a specific type of QN, namely Q_{24}, two of which can be found (as black dots) in the magnified image. This particular QN involves two failure-susceptible GBs (first index) with all four TJs being open bonds (second index). More specifically, at Q_{24}, two failure-susceptible GB planes meet at a single point in 3D space while all four TJ lines are open bonds of character J_1. At Q_{24}, then, the connectivity of TJs is necessarily guaranteed while that of GBs is not. This result is especially notable given that the small number fraction of Q_{24} at GB percolation (6.4%, see the arrow in **Figure 9.7**) leads to a dramatic (15.7%) difference in percolation behavior of GBs and TJs. The locations of these QNs in the microstructure thus plays a dominant role.

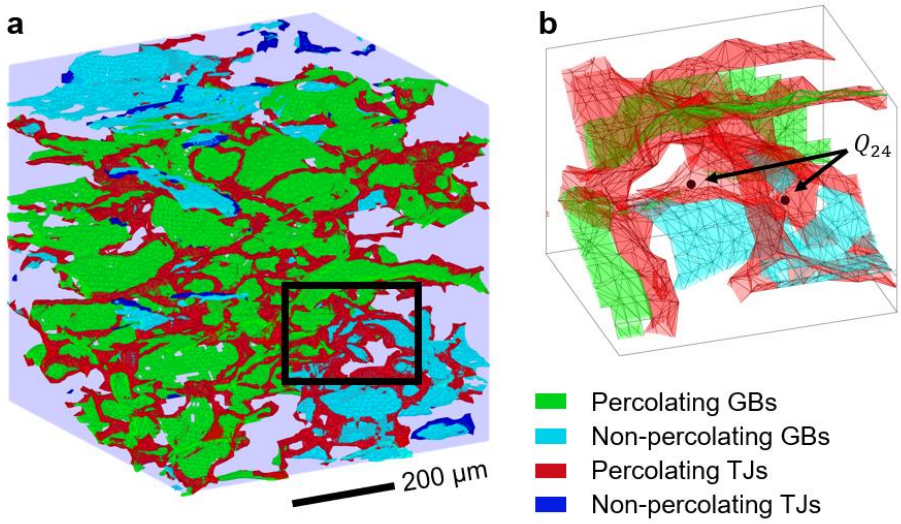

Figure 9.11. (a) 3D visualization of GB and TJ clusters within one of the largest cubic-shaped subvolumes at GB percolation (where the number fraction of failure susceptible GBs p = 0. 289). Green- and cyan-colored faces represent the GBs, which are either in the largest connected cluster (green) or not (cyan). Red- and blue-colored lines represent the TJs, which are either in the largest connected cluster (red) or not (blue). Black dots in inset (b) are an isomerism of QN, namely, Q_{24}.

9.3.4. Comparison of Trijunction p_c to Idealized Lattices

The connectivity of TJs in a microstructure is thought to share a similarity to bond percolation in 3D lattice structures [67]. The diamond cubic structure is tetrahedrally coordinated, which means that each atom has four bonds ($z = 4$). In a similar sense, QNs are connected to four TJs, by definition. Motivated by this simple analogy, we investigate whether the connectivity of TJs can truly be explained by that of idealized lattice structures. Since bond percolation thresholds of lattice structures are typically expressed in terms of the number fraction of bonds, we put our own results on the same plane of analysis: that is, we convert the number fraction of failure susceptible GBs into the number fraction of open TJs. In doing so, we find p_c' = 0.506, where the $'$ notation indicates that the percolation threshold is written in terms of the number fraction of open TJs. In comparison, the bond percolation threshold of the diamond lattice is p_c' = 0.389 [216–222].

The distinction in the two thresholds is surprising and thus warrants further consideration. We begin by reviewing the key assumptions of the percolation problem: (i) the bonds or lines are

opened at random, with some probability p', and (ii) the coordination of nodes is strictly four for the diamond lattice. Are these two assumptions fulfilled in our data?

To account for factor (i), we open each TJ in the microstructure at random, independent of its underlying crystallography (that is, we do not invoke the Brandon criterion described in **Sec. 9.2.3**). We reiterate that we focus on the same largest cubic-shaped subvolume, as before.[6] From the random assignment of TJs, we observe percolation in all three principal directions at $p_c' = 0.240 \pm 0.026$. This value is the averaged result of twenty randomized trials, and the small error reflects a relatively consistent percolation threshold. On the other hand, from above, we find $p_c' = 0.506$ when we use a crystallographic assignment of TJs. Thus, the system requires almost *twice* as many TJs to reach the percolation threshold given crystallographic constraints.[5] This can be understood as follows: with a crystallographic assignment, TJs must open along the perimeter of HAR GBs, forming a ring/loop, see inset of **Figure 9.12a**. That is, the TJs that form the ring structure must be at least of character J_1. On the other hand, a random assignment of open TJs shows no such spatial correlations, see inset of **Figure 9.12b**. To quantify the spatial distributions of open TJs in both cases, we calculate for each TJ the mean distance to its nearest-neighbor TJ.[7] Examples are shown in **Figure 9.12a-b** at $p' = 0.069$ for crystallographic and random assignments, respectively. As expected, the distribution is compressed towards the origin in the former case, since TJs neighbor each other along the ring. In the case of random assignment, however, the TJs are separated from their nearest neighbors over relatively greater distances. We next compare the average values of these two distributions *vs.* p', see **Figure 9.12c**. With

[6] We perform a study of bond percolation on a diamond lattice, which is of comparable size to the experimental subvolume (same order of magnitude in the number of TJs and QNs). Since the averaged result of twenty randomized trials is 0.43±0.01, *i.e.*, only ~10% different from that of an infinite lattice, we confirm that the finite size of the data alone cannot reconcile the discrepancy in percolation thresholds between the TJ and diamond lattices.

[7] That is, for each voxel i (out of n total) along an open TJ, we find using the k nearest neighbors algorithm [237] the distance x_i to a voxel on the nearest open TJ. The average of the measurements becomes the mean distance $\bar{x}$ between TJs, *i.e.*, $\bar{x} = (1/n)\sum_i^n x_i$.

increasing p', the average distances of both cases become very similar to each other as the open TJs become densely populated in the volume. In this limit, a TJ on the HAR GB ring may be just as close to a TJ off the ring as one that is on it. However, the differences between two cases become more pronounced as $p' \to 0$. Indeed, for a random assignment, TJ percolation occurs at $p'_c = 0.240 \pm 0.026$, wherein the difference in average distances is still substantial (91.3%, evaluated from **Figure 9.12c**). For this reason, we postulate that the spatial clustering of TJs under crystallographic constraints leads to a significantly reduced p'_c. While such constraints do not modify appreciably the *number fractions* of the four classes of TJs in our case (**Figure 9.5**), they do influence their *spatial distributions*.

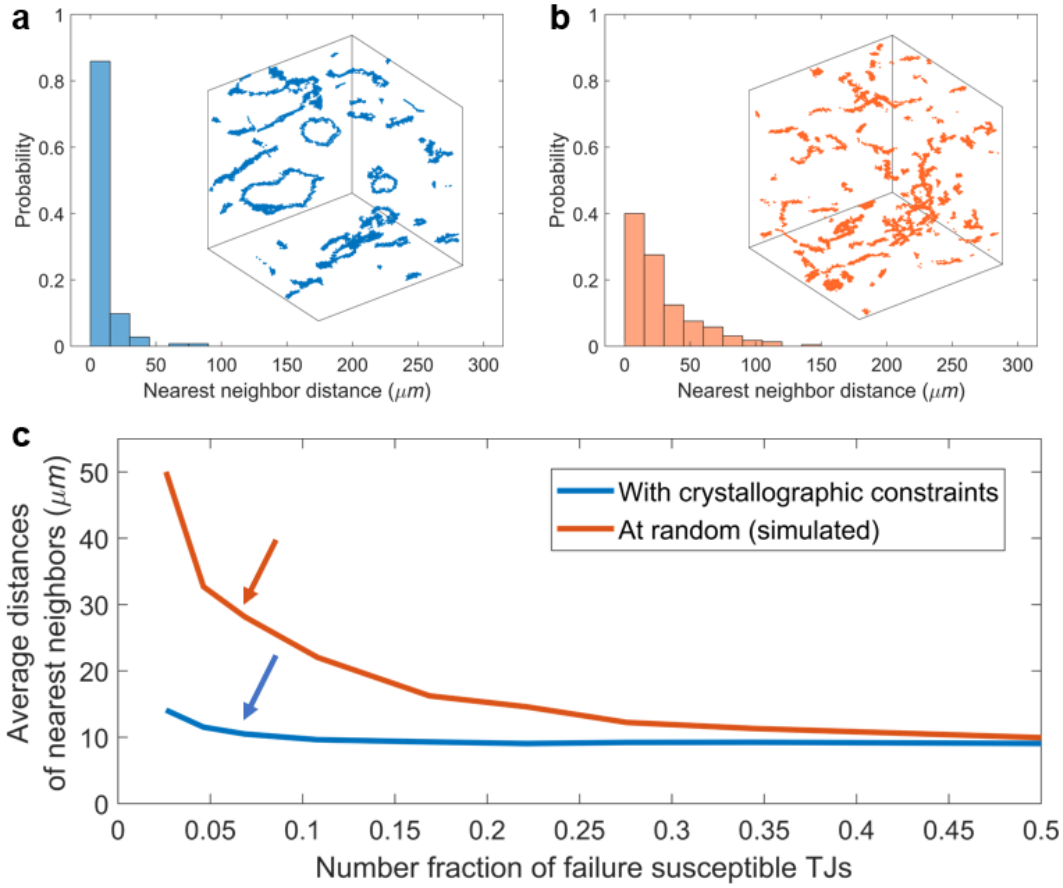

Figure 9.12. Quantification of spatial distribution of TJ in 3D, by calculating for each TJ the mean distance to its first nearest neighbor TJ. (a, b) Histograms of the mean distances when $p_c' = 0.069$ (a) with crystallographic and (b) random assignment of TJs. (c) Average of the mean distances over different number fraction of TJs, p'. Arrows indicate where (a) and (b) were evaluated.

Correcting for assumption (i) still does not bring us any closer to replicating the percolation behavior of the idealized lattice (from above: $p_c' = 0.240 \pm 0.026$ *vs.* for diamond: p_c' = 0.389). Thus, we examine assumption (ii) next. As the coordination number *z* plays critical role in bond percolation [67,223], we evaluate the connectivity of nodes in the microstructure. To find high coordinated nodes, we use a 3 × 3 × 3 kernel and search the subvolume for regions where four or more grains are found within this locality. We then look at permutations of each recorded instance and remove entries from the list if they either match one of the permutations, or if an entry with fewer grains matches a trimmed permutation of a larger cluster. This results in an identification of

937 unique clusters. To confirm our results, we then use the region adjacency graph to determine which grains are touching; with this approach, we are able to identify 663 unique clusters. This discrepancy can be attributed to the search kernel including grains that are separated by a single voxel, whereas those grain pairings would be absent on the adjacency graph. We justify using the larger node count for further analysis due the established gaps in TJ connectivity (**Sec. 9.3.3**) that was repaired by morphological closing. Ultimately, we confirm an unusually wide distribution of node coordination (**Figure 9.13**). Thermodynamically, nodes with greater than or less than four TJs are unstable [1]. We rationalize their existence by noting that several QNs are clustered in small regions (on the order of 5 μm, approaching the resolution limit of LabDCT), thereby behaving like a single large node with a higher coordination number. An example of such a cluster is shown in the inset of **Figure 9.13**. Five different grains meet each other, resulting in multiple QNs that are located close together, *i.e.*, with a one voxel TJ "bridge" between them.

Regarding the substructure of the node clusters, we observe 204 Q_{24} nodes among total 3,427 QNs within the subvolume, for $p = 0.289$. That said, not all the Q_{24} nodes contribute to the discrepancy in percolation thresholds between the GB and TJ networks. Those Q_{24} nodes within a cluster are highly interconnected (**Figure 9.14**) and thus less likely to lead to a difference between connectivity of GBs and TJs. Only 54 of the Q_{24} nodes present in the subvolume are isolated, *i.e.*, not part of any node clusters (**Figure 9.15**). Such 'isolated' Q_{24} sit on a unique path for percolation, leaving no other path available around the chokepoint that the Q_{24} creates. This can be seen in **Figure 9.11** where the cyan HAGB cluster is found in a corner with no alternate routes for percolation within the subvolume-of-interest.

Kinetically, it is not unreasonable to treat the clusters as single entities since the diffusion lengths between the component QNs are negligibly small (relative to the bulk microstructure).

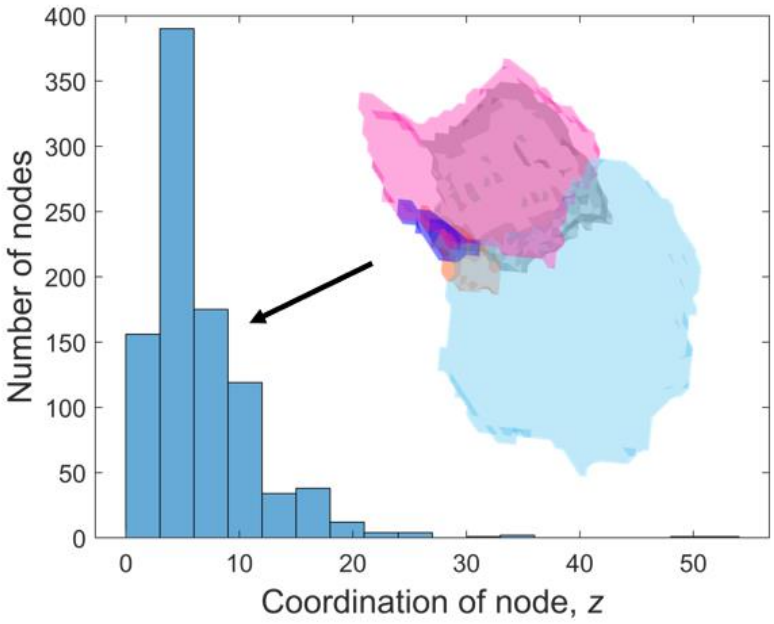

Figure 9.13. Distribution of node coordination z (expressed in terms of the number of TJs; for a diamond lattice, $z = 4$). Inset shows an example of a node with five different grains and nine TJs (the latter is not depicted). Grains are colored randomly for better contrast between them.

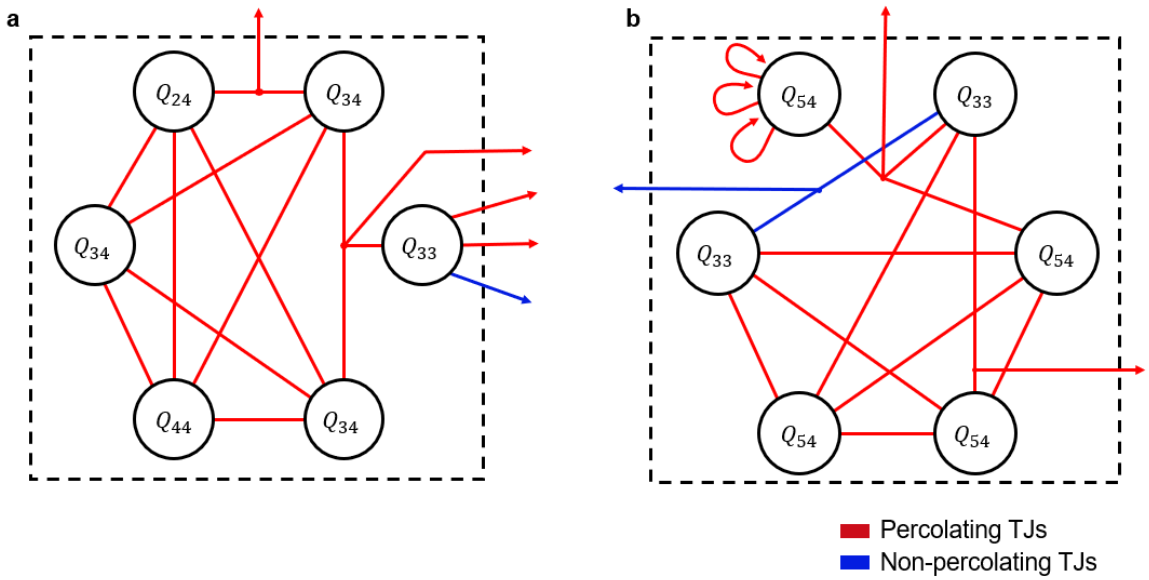

Figure 9.14. Topological maps for node clusters, retrieved from experimental data: (a) $z > 4$ and (b) $z < 4$. Black circles represent QNs, the character of which is labeled inside the circles. Lines represent TJs, which are either percolating (red) or not (blue), at $p = 0.289$. Boundary of cluster is indicated by dashed line. (a) shows a cluster of QNs with z of 5 as shown by five TJs are leaving the cluster boundary, thus serving as a source of higher-order connectivity. It contains examples of TJs being connected to *more than two* QNs (see horizontal red line between nodes Q_{24} and Q_{34}), which can occur if, *e.g.*, there exist small grains along the TJ line. (b) shows a cluster of QNs with z of 3 as indicated by the three TJs that leave the cluster boundary. It contains an example of TJs that are connected strictly to one QN (see around node Q_{54}), leading to a lower connectivity.

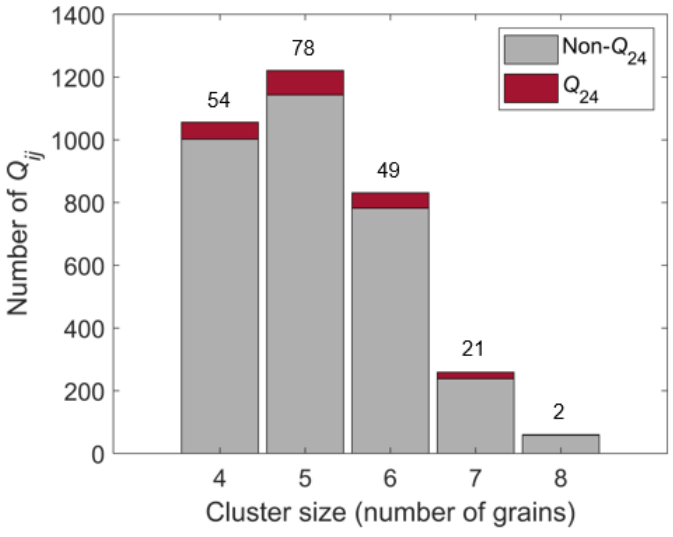

Figure 9.15. Number of Q_{24} in context of total number of QNs at percolation. The "special" Q_{24}, which result in differences in percolation between GB and TJs (**Sec. 3.3**), belong to *isolated* four-grain clusters. Conversely, the GBs that intercept Q_{24} nodes within the *larger* clusters are likely to "turn on" anyway due to the high degree of interconnectivity within the cluster.

Accordingly, if we accept the result of **Figure 9.13**, we find the mean coordination number of the nodes to be $\bar{z} = 6.184$. In the theory of bond percolation, it is reported that the reciprocal of the percolation threshold is proportional to the lattice coordination number, z [223]. **Fig. 16** shows the empirical correlation overlaid with the bond percolation thresholds of different 3D lattice structures including diamond [216–222], simple cubic [216,221,224–227], body-centered cubic [216,221,224,227], and face-centered cubic [216,224,228], with corresponding error bars. These data are also reported in **Table 9.3**. When we include our own data, namely $\bar{z} = 6.184$ and $p_c' = 0.240 \pm 0.026$ (obtained with random assignment of TJs), we find a good agreement between our result and the empirical correlation for bond percolation. Accounting for both effects (i-ii) enable us to place the TJ network in the context of theory.

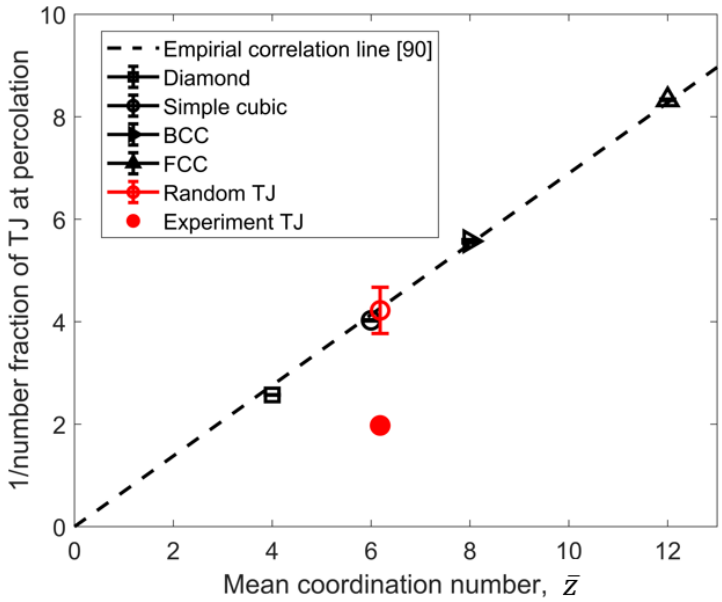

Figure 9.16. Empirical correlation between reciprocal of bond percolation thresholds ($1/p_c'$) and lattice coordination number (z), overlaid with bond percolation thresholds for different lattice structures with their error bars. These values are also given in **Table 9.3.** We include our measurements corresponding to the TJ network: an open red circle refers to TJs assigned at random, and a closed red circle refers to the TJs under crystallographic constraints.

Table 9.3. Number fractions of GBs and TJs at percolation (denoted, respectively) within the finite sized subvolume compared to bond percolation thresholds of ideal lattice structures.

Lattice	Coordination ($\bar{z}$)	Percolation threshold (p_c')	Reference
Diamond	4	$0.389 \pm 7.83e^{-04}$	[216–221]
Simple cubic	6	$0.248 \pm 7.57e^{-04}$	[216,221,224–227]
Body centered cubic	8	$0.180 \pm 1.10e^{-03}$	[216,221,224,227]
Face centered cubic	12	$0.120 \pm 2.11e^{-04}$	[216,224,228]

7.4. Conclusions

The present work has revealed for the first time the percolation threshold of GBs and TJs in a real, experimentally obtained 3D microstructure. Our efforts are made possible due to new strides nondestructive and high-throughput characterization *via* LabDCT that enable us to visualize 10,265 GBs and their connectivity. Firstly, by employing finite-size scaling together with the critical exponents from standard percolation theory, we find self-consistent percolation thresholds p_c of 0.236 ± 0.039 using different metrics. We compare our measurements against those from a simulated 3D microstructure [66], wherein grains are modelled as 14-sided polyhedra. We find that the percolation thresholds are remarkably similar if appropriately normalized by the number of grain neighbors. Secondly, we find that the TJ percolation threshold can serve as a lower bound to the GB percolation threshold due to the existence of one isomerism of quadruple node, Q_{24}, which facilitates TJ connectivity while impeding GB connectivity. Lastly, we test the commonly held hypothesis that the percolative behavior of the TJ network should be identical to that of the idealized diamond lattice due to their topological similarity. Instead, we find that the percolation thresholds are dissimilar due to a spatial clustering of TJs and a hyper-connectivity of nodes ($\bar{z} = 6.184$). Taken altogether, these results provide new insights into the influence of GB and TJs on percolation and help guide the design of polycrystalline materials that may otherwise fail due to the percolation of damage [21,59,181,187] along the GB and TJ networks.

Part IV. Conclusions and Outlooks

Chapter 10. Conclusions

The intrinsic grain structure of polycrystalline material has significant impact on its properties. This dissertation aims to investigate the structure and dynamics of grains and intergranular networks by leveraging nondestructive three-dimensional x-ray imaging techniques. The focus was placed on two scientific phenomena: (1) *abnormal grain growth* and (2) *percolation behavior of grain boundary networks*. **Part I**, composed of **Chapters 1-4,** provides a theoretical basis for the aforementioned the scientific phenomena of interest, as well as brief introduction of other key functions and concepts that were employed in the following main chapters of the dissertation. **Part II** introduces the core imaging techniques that are utilized throughout this dissertation. **Part III**, divided into **Chapter 6-9**, reports the scientific findings using the new imaging platform. The findings along with their broader impacts are reviewed here in **Part IV**.

10.1. In-house 3DXRD Data Processing Framework, *PolyProc*

Direct imaging of three-dimensional microstructure *via* x-ray diffraction-based techniques gives valuable insight into the crystallographic features that influence materials properties and performance. As such techniques become more accessible to researchers, demands are placed on processing the datasets that are inherently "noisy," multi-dimensional, and multimodal. To fulfill this need, **Chapter 6** introduces one-of-a-kind function package, *PolyProc*, that is compatible with

a range of data shapes, from planar sections to time-evolving and three-dimensional orientation data. The package comprises functions to import, filter, analyze, and visualize the reconstructed grain maps. To accelerate the computations in our pipeline, we harness computationally efficient approaches: for instance, data alignment is done *via* genetic optimization; grain tracking through the Hungarian method; and feature-to-feature correlation through k-nearest neighbors algorithm. As a proof-of-concept, we test our approach in characterizing the grain texture, topology, and evolution in a polycrystalline Al–Cu alloy undergoing coarsening.

The function package, *PolyProc*, is currently compatible with laboratory-based x-ray diffraction contrast tomography (LabDCT) and high-energy x-ray diffraction microscopy (HEDM). Thus, it has not only been heavily used throughout other projects of mine and others that employ LabDCT, but is also expected to be relevant to other probes that yield three- and four-dimensional microstructure datasets. Future efforts in the code developments can be directed towards extending compatibility with respect to other 3DXRD datasets, such as scanning 3DXRD (S3DXRD). Furthermore, as *PolyProc* has a modular architecture, additional modules with their own functionalities can be easily developed and integrated into the workflow based on future demands.

10.2. Mechanism of Abnormal Grain Growth in Particle Containing Systems

Second phase particles are routinely dispersed in metals and ceramics to prevent grain growth and take full advantage of the small grain size in the mechanical properties of polycrystals. Somewhat surprisingly, the preferential or abnormal growth of a few grains is observed in particle-containing systems at relatively high temperature (but below the solvus), which will limit the lifetime of the material. The origins and mechanisms of particle-assisted abnormal grain growth (AGG) are widely contested. In **Chapter 7**, we employ integrated three-dimensional x-ray

imaging to shed new light on the complex interactions between grain boundaries and particles in an Al-3.5wt%Cu alloy as a model system. We observe AGG in the presence of a highly non-random distribution of particles. The incipient grain size is set by the local distribution of particles such that the larger grains come from particle-poor regions. Subsequently, grains with a size advantage may "run away" from the grain size distribution, in agreement with predictions from an analytical model that takes into account the competing capillary and particle pinning pressures. This work supports the idea that *statistical fluctuations in the microstructure* (such as a nonuniform distribution of particles or GB mobilities) can trigger abnormal grain growth.

It follows that the processing conditions leading to a non-random particle distribution are far from being understood. In **Chapter 8**, we investigate the particle distribution and concomitant grain growth behavior at different annealing temperatures and times in an Al-3.5wt%Cu alloy by scanning electron microscopy (SEM). At high temperatures and long times, the particle distribution evolves from random to non-random, with an accompanying transition from normal grain growth (NGG) to AGG. Our investigation suggests that a non-random particle distribution is introduced by residual Cu segregation even after homogenization. In short, the corresponding fluctuation of θ-Al_2Cu phase distribution is amplified at elevated temperatures *via* severe particle dissolution. We quantify the spatial inhomogeneity of particles through the Gini coefficient and link this important parameter to the occurrence of AGG. The trends are conveyed succinctly in a temperature–time–(structural) transformation (TTT) diagram, which identifies the onset of AGG in an Al-3.5wt%Cu alloy. This is the first time that such a diagram has been used to describe the stability fields of normal and abnormal microstructures, to the best of my knowledge.

In a broader context, the insights gained from the two related studies in **Chapter 7 and 8** may provide guidance in optimization of processing parameters for particle-containing

engineering materials. That is, in case AGG is undesired (in order to, *e.g.*, maintain consistent properties), one may investigate what tolerance in the degree of nonuniformity in the distribution of the second phase is necessary to control microstructural evolution, as well as to estimate life span until the initiation of AGG. In contrast, AGG can be leveraged to attain single crystals.

10.2.1. Producing Single Crystals *via* AGG

Producing single crystals has been a thriving area of research for at least the past sixty years due to their highly unique properties [229]. For example, single-crystal turbine blades have the advantage of superior mechanical performance at an elevated temperature, which is offered by the high resistance to the creep failure due to the lack of grain boundaries. Currently, single crystals are grown by directional solidification processes that require costly optimization of multiple processing parameters (*e.g.*, solid-liquid interface velocities and thermal gradients). This large parameter space makes the manufacturing process challenging. An alternative route would be to grow single crystals from the solid-state, by taking advantage of AGG. In **Chapter 7**, we indeed observed that abnormal grain propagated and took up major portion of the sample volume, realizing single crystal region of the sample. This study gives us some inspiration: that is, we may design an AGG process to *intentionally* control the positions of grain boundaries.

Single crystals *via* AGG can be realized by passing a thermal gradient along a sample. According to **Chapters 7 - 8**, we know that a non-random particle distribution leads to selection of abnormally large grain. In these studies, the development of non-random particle distribution is attributed to the underlying nonuniformity in Cu distribution. This can be achieved by noting the temperature-dependency of particle phase volume fraction according to chemical thermodynamics. For example, the Al-side of the Al-Cu phase diagram tells us, as temperature increases, the volume fraction of θ-Al_2Cu particle phase as particles dissolve back into Al matrix.

Thus, if we realize large enough temperature gradient along the sample to attain a corresponding gradient in the (local) volume fraction of θ-Al_2Cu phase, AGG is expected to be triggered from the region with high temperatures due to the lack of a particle-pinning pressure. Therefore, we can control the grain and its orientation that is selected in AGG. In practice, such an experiment[8] can be done by directional annealing two- or three-temperature-zone in a Bridgman furnace.

10.2.2. Detailed Interaction between a Grain Boundary and Second Phase Particles

One of the remaining fundamental questions concerns the propagation mechanisms of the abnormal grain as it encounters new microstructural neighborhoods (*e.g.*, the particles) upon prolonged annealing. That is, its grain boundaries must overcome the drag pressure imposed by the second-phase particles in order to eventually "consume" the microstructure. The mechanism by which grain boundaries bypass particles is widely contested, with two divergent viewpoints: Zener-Smith's *pass-through* mechanism where particles effectively "punch out" regions of the grain boundary [44] (**Figure 2.2**) and Rios' *enveloping* mechanism where the grain boundary bends around the particle [230] (similar to dislocation dynamics, see **Figure 10.1**). The *pass-through* mechanism explains the pinning pressure by reduction of interfacial energy from the "punched out" regions. A particle that occupies the "punched out" region lowers energy by decreasing the area of a grain boundary. Once a grain boundary is pinned, areas of the "punched out" regions have to be created again if the grain boundary migrates away from the (immobile) particles. In contrast, the *enveloping* mechanism rationalizes the pinning pressure by introduction of additional interface area, similar to Orowan looping [231] of dislocation bypassing mechanism. A hard particle will lead to a bowing of the boundary and further creation of an increase in the

[8] The proposed strategy requires consideration on thermal conductivity of the system. An alloy with high thermal conductivity, like given example of Al alloy, is less likely to realize large enough temperature gradient. In contrast, an alloy like $Cu_{71.6}Mn_{17}Al_{11.4}$ (atomic percent) has been shown to sustain temperature gradients on the order of 1℃/mm.

interface area corresponding to the surface area of the particle (**Figure 10.1**). To date, conclusive experimental evidence of either mechanism has not been obtained due to technical difficulties in probing the interaction mechanism between grain boundaries and particles. Capturing *in situ* the moment that grain boundaries bypass the particles will be a breakthrough in this domain.

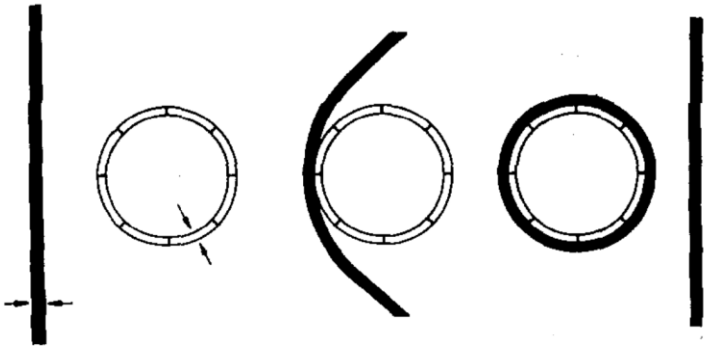

Figure 10.1. Illustration of interaction between a particle with a grain boundary migrating from left to right. The boundary (dark line) bends around the particle (open lines) enveloping it with a surface loop. Interfacial thickness is greatly exaggerated. Reprinted from Ref. [230].

This aforementioned task is challenging as it requires microscopic or atomic-level spatial resolution in 3D to characterize dislocations around the particle as well as the grain boundary curvature. Recent advancement in Bragg coherent diffraction imaging (BCDI) shows great potential for this experiment. BCDI is very sensitive to the presence of crystal defects including dislocations [232–235]. Thus, it could be the method of choice for the experiment. The presence of a dislocation loop before and after migration of a grain boundary would support the *enveloping* mechanism, thereby lending new insights on the long-standing question of the interaction between grain boundaries and the particle. As a first step, we can characterize the granular microstructure holistically *via* HEDM; then, using BCDI we can focus on a particle grain boundary for higher-resolution characterization [236].

10.3. Percolation Behavior of Three-dimensional Grain Boundary Networks

Percolation behavior of grain structures is a fundamental property of grain boundary (GB) networks that has so far been analyzed through synthetic three-dimensional (3D) microstructures alone. In **Chapter 9**, by applying finite-size scaling with the critical exponents from standard percolation theory, we determine from our experimental data a percolation threshold of 0.236 ± 0.039 for the GBs in the thermodynamic limit. We compare our results to those from past simulations, which model the 3D microstructure using space-filling polyhedra; the thresholds show good agreement when they are normalized by the topological characteristics of the GB network. We further investigate the percolation threshold of triple junction (TJ) lines, which we show to be necessarily lower than that of the GBs. The percolation behavior of TJs is also different from that of the theoretical diamond lattice due to two factors: a surprisingly higher coordination of nodes (6.184 *vs.* 4) and also a spatial clustering of TJs in the microstructure.

In a broader context, obtaining the intrinsic percolation thresholds of grain boundary networks using the framework of bond percolation theory provides insights on the design of failure-resistant granular materials *via* grain boundary engineering. That is, the percolation threshold serves as a gauge for how many failure-susceptible grain boundaries an engineering material can afford while ensuring resistivity toward intergranular failure modes (such as crack propagation or liquid metal embrittlement). On the other hand, the findings from percolation of triple junction (TJ) lines leaves many intriguing questions, which are addressed below.

10.3.1. Investigation of Nodes with Higher Coordination

We experimentally observed nodes with hyper-coordination (*i.e.*, greater than four bonds). It was somewhat surprising as previous theoretical studies assumed topological similarity between TJ connectivity and an idealized diamond lattice. On this basis, we compared the percolation

behavior of triple junctions (TJ) to bond percolation of ideal lattice structures solely based on the mean coordination number. Even though we found good alignment with our result and the empirical correlation between percolation threshold and coordination number (**Figure 9.16**), the influence of a wide distribution in node coordination has not been investigated, to our knowledge.

I propose to re-create the (measured) node coordination distribution using idealized diamond lattice structure to investigate the impact of distribution in node coordination. That is, by forcing a fraction of bonds to be "open" in the diamond lattice, we can artificially generate a higher coordination of nodes. Then, we can investigate the percolation behavior of this artificial lattice structure in order to provide insight the influence of distribution in node coordination. Using this approach, we can investigate also how the statistical moments of the node coordination distribution influence the resultant bond percolation threshold.

10.3.2. Transition from Two-dimensional to Three-dimensional Behavior

Percolation behaviors are dependent upon the dimensionality of system [61–63]. For instance, two-dimensional (2D) square and three-dimensional (3D) diamond lattices have the same coordination of 4, but different percolation thresholds of 0.50 and 0.389, respectively [63]. As mentioned in **Chapter 9**, experimental studies of percolation behavior so far have been focused on 2D grain boundary networks due to difficulties in characterizing representative 3D microstructures. As recent developments in crystallographic grain reconstructions and advanced adaptive scanning modes for large volume scanning with the LabDCT module provide unprecedented capabilities in characterizing large volume of grain structures with true sample representativeness, new opportunities arise to answer long standing questions.

One of the long standing questions concerns the transition of percolation behavior from 2D to 3D. Basinger *et al.* [193] reported the percolation threshold for 2D grain boundary networks in

alloy 304 stainless steel to be ~0.46. However, as mentioned earlier, the percolation threshold for 3D networks may be vastly different. Thus, it is of interest to understand the transition of percolation behavior by progressively including depth information on the imaged microstructure. That is, we can observe the change in percolation threshold as the field of volume (FOV) increases incrementally in the depth direction. The change in FOV from a thin layer to a cube may answer over what length-scales the percolation behavior transitions from 2D to 3D.

References

[1] F.J. Humphreys, M. Hatherly, Recrystallization and Related Annealing Phenomena: Second Edition, 2nd editio, Elsevier, 2004.

[2] R.W. Balluffi, S.M. Allen, W.C. Carter, Kinetics of Materials, John Wiley & Sons, 2005.

[3] N.J. Petch, The cleavage strength of polycrystals, J. Iron Steel Inst. 174 (1953) 25–28.

[4] E.O. Hall, The Deformation and Ageing of Mild Steel: I11 Discussion of Results, Proc. Phys. Soc. Sect. B. 64 (1951) 747.

[5] C.S. Pande, K.P. Cooper, Nanomechanics of Hall-Petch relationship in nanocrystalline materials, Prog. Mater. Sci. 54 (2009) 689–706. https://doi.org/10.1016/j.pmatsci.2009.03.008.

[6] E.M. Lehockey, D. Limoges, G. Palumbo, J. Sklarchuk, K. Tomantschger, A. Vincze, On improving the corrosion and growth resistance of positive Pb-acid battery grids by grain boundary engineering, J. Power Sources. 78 (1999) 79–83. https://doi.org/10.1016/S0378-7753(99)00015-4.

[7] Y. Pang, G. Chao, T. Luan, S. Gong, Y. Wang, Z. Jiang, Z. Xiao, Y. Jiang, Z. Li, Microstructure and properties of high strength, high conductivity and magnetic Cu–10Fe-0.4Si alloy, Mater. Sci. Eng. A. 826 (2021) 142012. https://doi.org/10.1016/j.msea.2021.142012.

[8] Q. Zhao, Z. Qian, X. Cui, Y. Wu, X. Liu, Optimizing microstructures of dilute Al-Fe-Si alloys designed with enhanced electrical conductivity and tensile strength, J. Alloys Compd. 650 (2015) 768–776. https://doi.org/10.1016/j.jallcom.2015.08.052.

[9] Q. Wei, D. Jia, K.T. Ramesh, E. Ma, Evolution and microstructure of shear bands in nanostructured Fe, Appl. Phys. Lett. 81 (2002) 1240–1242. https://doi.org/10.1063/1.1501158.

[10] R.A. Andrievskiĭ, G. V. Kalinnikov, N.P. Kobelev, Y.M. Soĭfer, D. V. Shtanskiĭ, Structure and physicomechanical properties of nanocrystalline boride-nitride films, Phys. Solid State. 39 (1997) 1661–1666. https://doi.org/10.1134/1.1129885.

[11] A.B. Witney, P.G. Sanders, J.R. Weertman, J.A. Eastman, Fatigue of nanocrystalline copper, Scr. Metall. Mater. 33 (1995) 2025–2030. https://doi.org/10.1016/0956-716X(95)00441-W.

[12] J.E. Carsley, J. Ning, W.W. Milligan, S.A. Hackney, E.C. Aifantis, A simple, mixtures-based model for the grain size dependence of strength in nanophase metals, Nanostructured Mater. 5 (1995) 441–448. https://doi.org/10.1016/0965-9773(95)00257-F.

[13] G.W. Nieman, J.R. Weertman, R.W. Siegel, Mechanical behavior of nanocrystalline Cu and Pd, J. Mater. Res. 6 (1991) 1012–1027. https://doi.org/10.1557/JMR.1991.1012.

[14] M. Shimada, H. Kokawa, Z.J. Wang, Y.S. Sato, I. Karibe, Optimization of grain boundary character distribution for intergranular corrosion resistant 304 stainless steel by twin-induced grain boundary engineering, in: Acta Mater., Pergamon, 2002: pp. 2331–2341. https://doi.org/10.1016/S1359-6454(02)00064-2.

[15] T. Watanabe, The impact of grain boundary character distribution on fracture in polycrystals, Mater. Sci. Eng. A. 176 (1994) 39–49. https://doi.org/10.1016/0921-5093(94)90957-1.

[16] V.Y. Gertsman, K. Tangri, Modelling of intergranular damage propagation, Acta Mater. 45 (1997) 4107–4116. https://doi.org/10.1016/S1359-6454(97)00083-9.

[17] M. Kumar, W.E. King, A.J. Schwartz, Modifications to the microstructural topology in f.c.c. materials through thermomechanical processing, Acta Mater. 48 (2000) 2081–2091. https://doi.org/10.1016/S1359-6454(00)00045-8.

[18] C.A. Schuh, M. Kumar, W.E. King, Analysis of grain boundary networks and their evolution during grain boundary engineering, Acta Mater. 51 (2003) 687–700. https://doi.org/10.1016/S1359-6454(02)00447-0.

[19] V. Traskine, P. Protsenko, Z. Skvortsova, P. Volovitch, Grain boundary wetting in polycrystals: Wettability of structure elements and liquid phase connectivity (part I), Colloids Surfaces A Physicochem. Eng. Asp. 166 (2000) 261–268. https://doi.org/10.1016/S0927-7757(99)00491-4.

[20] Y. Chen, C.A. Schuh, Percolation of diffusional creep: A new universality class, Phys. Rev. Lett. 98 (2007). https://doi.org/10.1103/PhysRevLett.98.035701.

[21] N. Lu, S. Moniri, M.R. Wiltse, J. Spielman, N. Senabulya, A.J. Shahani, Dynamics of Ga penetration in textured Al polycrystal revealed through multimodal three-dimensional analysis, Acta Mater. 217 (2021) 117145. https://doi.org/10.1016/j.actamat.2021.117145.

[22] G. Gottstein, Physical Foundations of Materials Science, Springer Berlin Heidelberg, 2004. https://doi.org/10.1007/978-3-662-09291-0.

[23] J.E. Burke, D. Turnbull, Recrystallization and grain growth, Prog. Met. Phys. 3 (1952). https://doi.org/10.1016/0502-8205(52)90009-9.

[24] J.. Burke, Some factors affecting the rate of grain growth in metals, Trans. Met. Soc. A.I.M.E. 180 (1949) 73–91.

[25] J.W. CHRISTIAN, Equilibrium and General Kinetic Theory, in: Theory Transform. Met. Alloy., 2002. https://doi.org/10.1016/b978-008044019-4/50003-9.

[26] G.F. Bolling, W.C. Winegard, Grain growth in zone-refined lead, Acta Metall. 6 (1958) 283–287. https://doi.org/10.1016/0001-6160(58)90148-2.

[27] J.P. Drolet, A. Galibois, The impurity-drag effect on grain growth, Acta Metall. 16 (1968) 1387–1399. https://doi.org/10.1016/0001-6160(68)90035-7.

[28] G.T. Higgins, Grain-Boundary Migration and Grain Growth, Met. Sci. 8 (1974) 143–150. https://doi.org/10.1179/msc.1974.8.1.143.

[29] M. Hillert, On the theory of normal and abnormal grain growth, Acta Metall. 13 (1965) 227–238. https://doi.org/10.1016/0001-6160(65)90200-2.

[30] I.M. Lifshitz, V. V. Slyozov, The kinetics of precipitation from supersaturated solid solutions, J. Phys. Chem. Solids. 19 (1961) 35–50. https://doi.org/10.1016/0022-3697(61)90054-3.

[31] C.S. Smith, Grain Shapes and Other Metallurgical Applications of Topology, Trans. Met. Soc. AIME. (1952). https://doi.org/10.1007/s13632-015-0241-1.

[32] J. von Neumann, Metal interfaces, Am. Soc. Met. 108–110 (1952).

[33] W.W. Mullins, Two-dimensional motion of idealized grain boundaries, J. Appl. Phys. 27 (1956) 900–904. https://doi.org/10.1063/1.1722511.

[34] R.D. MacPherson, D.J. Srolovitz, The von Neumann relation generalized to coarsening of three-dimensional microstructures, Nature. 446 (2007) 1053–1055. https://doi.org/10.1038/nature05745.

[35] A.M. Kraynik, S.A. Koehler, H.A. Stone, S. Hilgenfeldt, An accurate von Neumann's law for three-dimensional foams, Phys. Rev. Lett. 86 (2001) 2685–2688. https://doi.org/10.1103/PhysRevLett.86.2685.

[36] D.J. Rowenhorst, A.C. Lewis, G. Spanos, Three-dimensional analysis of grain topology

and interface curvature in a β-titanium alloy, Acta Mater. 58 (2010) 5511–5519. https://doi.org/10.1016/j.actamat.2010.06.030.

[37] M.E. Glicksman, P.R. Rios, Minimal network partitions using average N-hedra, Philos. Mag. 87 (2007) 189–208. https://doi.org/10.1080/14786430600885420.

[38] P.R. Rios, M.E. Glicksman, Polyhedral model for self-similar grain growth, Acta Mater. 56 (2008) 1165–1171. https://doi.org/10.1016/j.actamat.2007.11.010.

[39] D.M. Saylor, B.S. El-Dasher, B.L. Adams, G.S. Rohrer, Measuring the five-parameter grain-boundary distribution from observations of planar sections, Metall. Mater. Trans. A Phys. Metall. Mater. Sci. 35 A (2004) 1981–1989. https://doi.org/10.1007/s11661-004-0147-z.

[40] W.T. Read, W. Shockley, Dislocation models of crystal grain boundaries, Phys. Rev. 78 (1950) 275–289. https://doi.org/10.1103/PhysRev.78.275.

[41] F.J. Humphreys, A unified theory of recovery, recrystallization and grain growth, based on the stability and growth of cellular microstructures - I. The basic model, Acta Mater. 45 (1997) 4231–4240. https://doi.org/10.1016/S1359-6454(97)00070-0.

[42] B.L. DeCost, E.A. Holm, Phenomenology of Abnormal Grain Growth in Systems with Nonuniform Grain Boundary Mobility, Metall. Mater. Trans. A Phys. Metall. Mater. Sci. 48 (2017) 2771–2780. https://doi.org/10.1007/s11661-016-3673-6.

[43] G.S. Grest, M.P. Anderson, D.J. Srolovitz, A.D. Rollett, Abnormal grain growth in three dimensions, Scr. Metall. Mater. 24 (1990) 661–665. https://doi.org/10.1016/0956-716X(90)90219-7.

[44] C.S. Smith, Grains, phases, and interfaces: An introduction of microstructure, in: Trans. Met. Soc. AIME, 1948: p. 15. https://doi.org/10.1007/s11661-010-0215-5.

[45] P.A. Manohar, M. Ferry, T. Chandra, Five Decades of the Zener Equation., ISIJ Int. 38 (2008) 913–924. https://doi.org/10.2355/isijinternational.38.913.

[46] T. Omori, T. Kusama, S. Kawata, I. Ohnuma, Y. Sutou, Y. Araki, K. Ishida, R. Kainuma, Abnormal grain growth induced by cyclic heat treatment, Science. 341 (2013) 1500–2. https://doi.org/10.1126/science.1238017.

[47] T. Kusama, T. Omori, T. Saito, S. Kise, T. Tanaka, Y. Araki, R. Kainuma, Ultra-large single crystals by abnormal grain growth, Nat. Commun. 8 (2017) 354. https://doi.org/10.1038/s41467-017-00383-0.

[48] C. V. Thompson, H.J. Frost, F. Spaepen, The relative rates of secondary and normal grain growth, Acta Metall. 35 (1987) 887–890. https://doi.org/10.1016/0001-6160(87)90166-0.

[49] J. Dennis, P.S. Bate, F.J. Humphreys, Abnormal grain growth in Al-3.5Cu, Acta Mater. 57 (2009) 4539–4547. https://doi.org/10.1016/j.actamat.2009.06.018.

[50] F.T. Lewis, The correlation between cell division and the shapes and sizes of prismatic cells in the epidermis of cucumis, Anat. Rec. 38 (1928) 341–376. https://doi.org/10.1002/AR.1090380305.

[51] J.W. Martin, R.D. Doherty, B. Cantor, Stability of Microstructure in Metallic Systems, 2nd ed., Cambridge university press, 1997. https://doi.org/10.1017/cbo9780511623134.

[52] I. ANDERSEN, O. GRONG, N. RYUM, ANALYTICAL MODELLING OF GRAIN GROWTH IN METALS AND ALLOYS IN THE PRESENCE OF GROWING AND DISSOLVING PRECIPITATES-II. ABNORMAL GRAIN GROWTH, Acta Metall. Mater. 43 (1995) 2689–2700. https://ac-els-cdn-com.proxy.lib.umich.edu/0956715194004895/1-s2.0-0956715194004895-main.pdf?_tid=fd73199e-9734-429b-b9bb-

f22f71ce730d&acdnat=1549503722_2588e35fec9f71872527401716257 5f7 (accessed February 6, 2019).

[53] G.W. Rathenau, J.F.H. Custers, Secondary Recrystallization of Face-Centered Nickel-iran Alloys, Phillips Res. Reports. 4 (1949) 241.

[54] J.S. Bowles, W. Boas, The Effect of Crystal Arrangement on “Secondary Recrystallization” in Metals., J. Inst. Met. 24 (1948) 501.

[55] P.A. Beck, H. Hu, Annealing Textures in Rolled Face-Centered Cubic Metals, JOM. 4 (1952) 83–90. https://doi.org/10.1007/bf03397656.

[56] G. Abbruzzese, K. Lücke, A theory of texture controlled grain growth-I. Derivation and general discussion of the model, Acta Metall. 34 (1986) 905–914. https://doi.org/10.1016/0001-6160(86)90064-7.

[57] H. Eichelkraut, G. Abbruzzese, K. Lücke, A theory of texture controlled grain growth-II. Numerical and analytical treatment of grain growth in the presence of two texture components, Acta Metall. 36 (1988) 55–68. https://doi.org/10.1016/0001-6160(88)90028-4.

[58] Y. Pan, T. Olson, B.L. Adams, Applications of orientation imaging analysis to microstructural control of intergranular stress corrosion cracking, Can. Metall. Q. 34 (1995) 147–154. https://doi.org/10.1016/0008-4433(95)00008-L.

[59] P. Lin, G. Palumbo, U. Erb, K.T. Aust, Influence of grain boundary character distribution on sensitization and intergranular corrosion of alloy 600, Scr. Metall. Mater. 33 (1995) 1387–1392. https://doi.org/10.1016/0956-716X(95)00420-Z.

[60] S. Kirkpatrick, Percolation and Conduction, Rev. Mod. Phys. 45 (1973) 574–588. https://doi.org/10.1103/RevModPhys.45.574.

[61] A. Bunde, S. Havlin, Fractals and Disordered Systems, 2nd ed., Springer-Verlag, 1996.

[62] K. Christensen, N.R. Moloney, COMPLEXITY AND CRITICALITY, in: Imp. Coll. Press. London, 2005.

[63] D. Stauffer, A. Aharony, Introduction to PERCOLATION THEORY, 2003.

[64] M. Frary, C.A. Schuh, Grain boundary networks: Scaling laws, preferred cluster structure, and their implications for grain boundary engineering, Acta Mater. 53 (2005) 4323–4335. https://doi.org/10.1016/j.actamat.2005.05.030.

[65] C.A. Schuh, R.W. Minich, M. Kumar, Connectivity and percolation in simulated grain-boundary networks, Philos. Mag. 83 (2003) 711–726. https://doi.org/10.1080/0141861021000056681.

[66] M. Frary, C.A. Schuh, Connectivity and percolation behaviour of grain boundary networks in three dimensions, Philos. Mag. 85 (2005) 1123–1143. https://doi.org/10.1080/14786430412331323564.

[67] L. Priester, Grain Boundaries From Theory to Engineering, Springer, 2013.

[68] S. Schumacher, R. Birringer, R. Strauß, H. Gleiter, Diffusion of silver in nanocrystalline copper between 303 and 373 K, Acta Metall. 37 (1989) 2485–2488. https://doi.org/10.1016/0001-6160(89)90046-1.

[69] H.E. Schaefer, R. Wurschum, T. Gessmann, G. Stöckl, P. Scharwaechter, W. Frank, R.Z. Valiev, H.J. Fecht, C. Moelle, Diffusion and free volumes in nanocrystalline Pd, Nanostructured Mater. 6 (1995) 869–872. https://doi.org/10.1016/0965-9773(95)00197-2.

[70] H.J. Höfler, R.S. Averback, H. Hahn, H. Gleiter, Diffusion of bismuth and gold in nanocrystalline copper, J. Appl. Phys. 74 (1993) 3832–3839. https://doi.org/10.1063/1.354477.

[71] Y.R. Kolobov, G.P. Grabovetskaya, M.B. Ivanov, A.P. Zhilyaev, R.Z. Valiev, Grain boundary diffusion characteristics of nanostructured nickel, Scr. Mater. 44 (2001) 873–878. https://doi.org/10.1016/S1359-6462(00)00699-0.

[72] J. Horváth, R. Birringer, H. Gleiter, Diffusion in nanocrystalline material, Solid State Commun. 62 (1987) 319–322. https://doi.org/10.1016/0038-1098(87)90989-6.

[73] Z.B. Wang, N.R. Tao, W.P. Tong, J. Lu, K. Lu, Diffusion of chromium in nanocrystalline iron produced by means of surface mechanical attrition treatment, Acta Mater. 51 (2003) 4319–4329. https://doi.org/10.1016/S1359-6454(03)00260-X.

[74] Y. Chen, C.A. Schuh, Contribution of triple junctions to the diffusion anomaly in nanocrystalline materials, Scr. Mater. 57 (2007) 253–256. https://doi.org/10.1016/j.scriptamat.2007.03.057.

[75] K. Miyazawa, Y. Iwasaki, K. Ito, Y. Ishida, Combination rule of Σ values at triple junctions in cubic polycrystals, Acta Crystallogr. Sect. A Found. Crystallogr. 52 (1996) 787–796. https://doi.org/10.1107/S0108767396005934.

[76] D.G. Brandon, The structure of high-angle grain boundaries, Acta Metall. 14 (1966) 1479–1484. https://doi.org/10.1016/0001-6160(66)90168-4.

[77] P.H. Pumphrey, G.A. Chadwick, D.A. Smith, grain boundary structure and properties, in: Acad. Press. London, 1976: p. 139.

[78] G. Palumbo, K.T. Aust, E.M. Lehockey, U. Erb, P. Lin, On a More Restrictive Geometric Criterion for “Special” CSL Grain Boundaries, Scr. Mater. 38 (1998) 1685–1690. https://doi.org/10.1016/S1359-6462(98)00077-3.

[79] Y. Ishida, M. McLean, Burgers vectors of boundary dislocations in ordered grain boundaries of cubic metals, Philos. Mag. 27 (1973) 1125–1134.

https://doi.org/10.1080/14786437308225821.

[80] J. Kang, N. Lu, I. Loo, N. Senabulya, A.J. Shahani, PolyProc: A Modular Processing Pipeline for X-ray Diffraction Tomography, Integr. Mater. Manuf. Innov. 8 (2019) 388–399. https://doi.org/10.1007/s40192-019-00147-2.

[81] N. Lu, J. Kang, N. Senabulya, R. Keinan, N. Gueninchault, A.J. Shahani, Dynamics of particle-assisted abnormal grain growth revealed through integrated three-dimensional microanalysis, Acta Mater. 195 (2020) 1–12. https://doi.org/10.1016/j.actamat.2020.04.049.

[82] N. Lu, J. Kang, A.J. Shahani, Origins of Non-random Particle Distributions and Implications to Abnormal Grain Growth in an Al-3.5 Wt Pct Cu Alloy, Metall. Mater. Trans. A Phys. Metall. Mater. Sci. 52 (2021) 914–927. https://doi.org/10.1007/s11661-020-06125-0.

[83] J. Kang, K. Walter, H. Bale, A.J. Shahani, Percolation of Grain Boundaries and Triple Junctions in Three Dimensions: A Test of Theory, Submitted. (2022).

[84] C. Holzner, L. Lavery, H. Bale, A. Merkle, S. McDonald, P. Withers, Y. Zhang, D.J. Jensen, M. Kimura, A. Lyckegaard, P. Reischig, E.M. Lauridsen, Diffraction Contrast Tomography in the Laboratory – Applications and Future Directions, Micros. Today. 24 (2016) 34–43. https://doi.org/10.1017/s1551929516000584.

[85] A.C. Kak, M. Slaney, Principles of Computerized Tomographic Imaging, Society for Industrial and Applied Mathematics, 2001.

[86] J.C. Russ, The Image Processing Handbook 6th edition, CRC Press, 2011.

[87] R. Keinan, H. Bale, N. Gueninchault, E.M. Lauridsen, A.J. Shahani, Integrated imaging in three dimensions: Providing a new lens on grain boundaries, particles, and their

correlations in polycrystalline silicon, Acta Mater. 148 (2018) 225–234. https://doi.org/10.1016/j.actamat.2018.01.045.

[88] M.D. Uchic, L. Holzer, B.J. Inkson, E.L. Principe, P. Munroe, Three-dimensional microstructural characterization using focused ion beam tomography, MRS Bull. 32 (2007) 408–416. https://doi.org/10.1557/mrs2007.64.

[89] D.J. Rowenhorst, A. Gupta, C.R. Feng, G. Spanos, 3D Crystallographic and morphological analysis of coarse martensite: Combining EBSD and serial sectioning, Scr. Mater. 55 (2006) 11–16. https://doi.org/10.1016/j.scriptamat.2005.12.061.

[90] M.A. Groeber, B.K. Haley, M.D. Uchic, D.M. Dimiduk, S. Ghosh, 3D reconstruction and characterization of polycrystalline microstructures using a FIB-SEM system, Mater. Charact. 57 (2006) 259–273. https://doi.org/10.1016/j.matchar.2006.01.019.

[91] G.N. Hounsfield, Computerized transverse axial scanning (tomography): I. Description of system, Br. J. Radiol. 46 (1973) 1016–1022. https://doi.org/10.1259/0007-1285-46-552-1016.

[92] E.M. Lauridsen, S. Schmidt, R.M. Suter, H.F. Poulsen, Applied Crystallography Tracking: a method for structural characterization of grains in powders or polycrystals, J. Appl. Cryst. 34 (2001). https://journals.iucr.org/j/issues/2001/06/00/pe0072/pe0072.pdf (accessed April 24, 2019).

[93] H.F. Poulsen, An introduction to three-dimensional X-ray diffraction microscopy, J. Appl. Crystallogr. 45 (2012) 1084–1097. https://doi.org/10.1107/s0021889812039143.

[94] W. Ludwig, A. King, P. Reischig, M. Herbig, E.M. Lauridsen, S. Schmidt, H. Proudhon, S. Forest, P. Cloetens, S.R. du Roscoat, J.Y. Buffière, T.J. Marrow, H.F. Poulsen, New opportunities for 3D materials science of polycrystalline materials at the micrometre

lengthscale by combined use of X-ray diffraction and X-ray imaging, Mater. Sci. Eng. A. 524 (2009) 69–76. https://doi.org/10.1016/j.msea.2009.04.009.

[95] R.M. Suter, D. Hennessy, C. Xiao, U. Lienert, Forward modeling method for microstructure reconstruction using x-ray diffraction microscopy: Single-crystal verification, Rev. Sci. Instrum. 77 (2006) 123905. https://doi.org/10.1063/1.2400017.

[96] G. Johnson, A. King, M. Goncalves Honnicke, J. Marrow, W. Ludwig, X-ray diffraction contrast tomography: a novel technique for three-dimensional grain mapping of polycrystals. II. The combined case, J. Appl. Cryst. 41 (2008) 310–318. https://doi.org/10.1107/S0021889808001726.

[97] Y. Hayashi, Y. Hirose, Y. Seno, Polycrystal orientation mapping using scanning three-dimensional X-ray diffraction microscopy, J. Appl. Cryst. 48 (2015) 1094–1101. https://doi.org/10.1107/S1600576715009899.

[98] A. King, P. Reischig, J. Adrien, S. Peetermans, W. Ludwig, Polychromatic diffraction contrast tomography, Mater. Charact. 97 (2014) 1–10. https://doi.org/10.1016/j.matchar.2014.07.026.

[99] L. Renversade, R. Quey, W. Ludwig, D. Menasche, S. Maddali, R.M. Suter, A. Borbély, Comparison between diffraction contrast tomography and high-energy diffraction microscopy on a slightly deformed aluminium alloy, IUCrJ. 3 (2016) 32–42. https://doi.org/10.1107/S2052252515019995.

[100] S.A. McDonald, P. Reischig, C. Holzner, E.M. Lauridsen, P.J. Withers, A.P. Merkle, M. Feser, Non-destructive mapping of grain orientations in 3D by laboratory X-ray microscopy, Sci. Rep. 5 (2015). https://doi.org/10.1038/srep14665.

[101] J. Sun, Y. Zhang, A. Lyckegaard, F. Bachmann, E.M. Lauridsen, D. Juul Jensen, Grain

boundary wetting correlated to the grain boundary properties: A laboratory-based multimodal X-ray tomography investigation, Scr. Mater. 163 (2019) 77–81. https://doi.org/10.1016/j.scriptamat.2019.01.007.

[102] S.A. McDonald, C. Holzner, E.M. Lauridsen, P. Reischig, A.P. Merkle, P.J. Withers, Microstructural evolution during sintering of copper particles studied by laboratory diffraction contrast tomography (LabDCT), Sci. Rep. 7 (2017) 5251. https://doi.org/10.1038/s41598-017-04742-1.

[103] J. Sun, A. Lyckegaard, Y.B. Zhang, S.A. Catherine, B.R. Patterson, F. Bachmann, N. Gueninchault, H. Bale, C. Holzner, E. Lauridsen, D. Juul Jensen, 4D Study of Grain Growth in Armco Iron Using Laboratory X-ray Diffraction Contrast Tomography, in: IOP Conf. Ser. Mater. Sci. Eng., 2017. https://doi.org/10.1088/1757-899X/219/1/012039.

[104] D. Gürsoy, F. De Carlo, X. Xiao, C. Jacobsen, TomoPy: A framework for the analysis of synchrotron tomographic data, J. Synchrotron Radiat. 21 (2014) 1188–1193. https://doi.org/10.1107/S1600577514013939.

[105] F. Bachmann, R. Hielscher, H. Schaeben, Texture Analysis with MTEX – Free and Open Source Software Toolbox, Solid State Phenom. 160 (2010) 63–68. https://doi.org/10.4028/www.scientific.net/ssp.160.63.

[106] M.A. Groeber, M.A. Jackson, DREAM.3D: A Digital Representation Environment for the Analysis of Microstructure in 3D, Integr. Mater. Manuf. Innov. 3 (2014) 5. https://doi.org/10.1186/2193-9772-3-5.

[107] D.E. Goldberg, J.H. Holland, Genetic Algorithms and Machine Learning, Mach. Learn. 3 (1988) 95–99. https://doi.org/10.1023/A:1022602019183.

[108] C.K. Chow, H.T. Tsui, T. Lee, Surface registration using a dynamic genetic algorithm,

Pattern Recognit. 37 (2004) 105–117. https://doi.org/10.1016/S0031-3203(03)00222-X.

[109] E. Lomonosov, D. Chetverikov, A. Ekárt, Pre-registration of arbitrarily oriented 3D surfaces using a genetic algorithm, Pattern Recognit. Lett. 27 (2006) 1201–1208. https://doi.org/10.1016/j.patrec.2005.07.018.

[110] K. Brunnstrom, A.J. Stoddart, Genetic algorithms for free-form surface matching, in: Proc. 13th Int. Conf. Pattern Recognit., IEEE, 1996: pp. 689–693 vol.4. https://doi.org/10.1109/ICPR.1996.547653.

[111] E.E. Underwood, QUANTITATIVE STEREOLOGY FOR MICROSTRUCTURAL ANALYSIS, n.d. https://link.springer.com/content/pdf/10.1007/978-1-4615-8693-7_3.pdf (accessed April 27, 2019).

[112] R.T. DeHoff, E.H. Aigeltinger, K.R. Craig, Experimental determination of the topological properties of three-dimensional microstructures, J. Microsc. 95 (1972) 69–91. https://doi.org/10.1111/j.1365-2818.1972.tb03712.x.

[113] A.J. Shahani, X. Xiao, K. Skinner, M. Peters, P.W. Voorhees, Ostwald ripening of faceted Si particles in an Al-Si-Cu melt, Mater. Sci. Eng. A. 673 (2016) 307–320. https://doi.org/10.1016/j.msea.2016.06.077.

[114] C.G. Roberts, S.L. Semiatin, A.D. Rollett, Particle-associated misorientation distribution in a nickel-base superalloy, Scr. Mater. 56 (2007) 899–902. https://doi.org/10.1016/j.scriptamat.2007.01.034.

[115] G.S. Rohrer, Measuring changes in grain shapes and sizes in polycrystalline Ni, n.d.

[116] H.W. Kuhn, The Hungarian method for the assignment problem, Nav. Res. Logist. Q. 2 (1955) 83–97. https://doi.org/10.1002/nav.3800020109.

[117] F. Bourgeois, J.-C. Lassalle, An extension of the Munkres algorithm for the assignment

problem to rectangular matrices, Commun. ACM. 14 (2002) 802–804. https://doi.org/10.1145/362919.362945.

[118] T. Gladman, On the theory of the effect of precipitate particles on grain growth in metals, Proc. R. Soc. London. Ser. A. Math. Phys. Sci. 294 (1966) 298–309. https://doi.org/10.1098/rspa.1966.0208.

[119] N. Louat, The inhibition of grain-boundary motion by a dispersion of particles, Http://Dx.Doi.Org/10.1080/01418618308243128. 47 (2006) 903–912. https://doi.org/10.1080/01418618308243128.

[120] N. Louat, The resistance to normal grain growth from a dispersion of spherical particles, Acta Metall. 30 (1982) 1291–1294. https://doi.org/10.1016/0001-6160(82)90147-X.

[121] D.J. Srolovitz, M.P. Anderson, G.S. Grest, P.S. Sahni, Computer simulation of grain growth-III. Influence of a particle dispersion, Acta Metall. 32 (1984) 1429–1438. https://doi.org/10.1016/0001-6160(84)90089-0.

[122] E. El-Kashif, K. Asakura, T. Koseki, K. Shibata, Effects of boron, niobium and titanium on grain growth in ultra high purity 18% Cr ferritic stainless steel, ISIJ Int. 44 (2004) 1568–1575. https://doi.org/10.2355/isijinternational.44.1568.

[123] J. Janis, K. Nakajima, A. Karasev, H. Shibata, P.G. Jönsson, An experimental study on the influence of particles on grain boundary migration, J. Mater. Sci. 45 (2010) 2233–2238. https://doi.org/10.1007/s10853-009-3908-7.

[124] J. Janis, A. Karasev, K. Nakajima, P. Göran JÖNSSON, Effect of Secondary Nitride Particles on Grain Growth in a Fe-20 mass% Cr Alloy Deoxidised with Ti and Zr, ISIJ Int. 53 (2013) 476–483. https://doi.org/10.2355/isijinternational.53.476.

[125] D. Duly, G.J. Baxter, H.R. Shercliff, J.A. Whiteman, C.M. Sellars, M.F. Ashby,

Microstructure and local crystallographic evolution in an Al-1 wt% Mg alloy deformed at intermediate temperature and high strain-rate, Acta Mater. 44 (1996) 2947–2962. https://doi.org/10.1016/1359-6454(95)00392-4.

[126] C. V. Thompson, R. Carel, Stress and grain growth in thin films, J. Mech. Phys. Solids. 44 (1996) 657–673. https://doi.org/10.1016/0022-5096(96)00022-1.

[127] E.M. Zielinski, R.P. Vinci, J.C. Bravman, The influence of strain energy on abnormal grain growth in copper thin films, Appl. Phys. Lett. 67 (1995) 1078. https://doi.org/10.1063/1.114455.

[128] J.M. Zhang, K.W. Xu, V. Ji, Strain-energy-driven abnormal grain growth in copper films on silicon substrates, J. Cryst. Growth. 226 (2001) 168–174. https://doi.org/10.1016/S0022-0248(01)01376-8.

[129] N. Rajmohan, J.. Szpunar, Y. Hayakawa, A role of fractions of mobile grain boundaries in secondary recrystallization of Fe–Si steels, Acta Mater. 47 (1999) 2999–3008. https://doi.org/10.1016/S1359-6454(99)00162-7.

[130] Y. Ushigami, T. Kumano, T. Haratani, S. Nakamura, S. Takebayashi, T. Kubota, Secondary recrystallization in grain-oriented silicon steel, in: Mater. Sci. Forum, 2004: pp. 853–862. https://doi.org/10.4028/www.scientific.net/msf.467-470.853.

[131] I.J. Bae, S. Baik, Abnormal grain growth of alumina, J. Am. Ceram. Soc. 80 (1997) 1149–1156. https://doi.org/10.1111/j.1151-2916.1997.tb02957.x.

[132] J. Dennis, P.S. Bate, F.J. Humphreys, Abnormal Grain Growth in Metals, Acta Mater. 558–559 (2007) 717–722. https://doi.org/10.1016/j.actamat.2009.06.018.

[133] E.A. Holm, T.D. Hoffmann, A.D. Rollett, C.G. Roberts, Particle-assisted abnormal grain growth, in: IOP Conf. Ser. Mater. Sci. Eng., 2015. https://doi.org/10.1088/1757-

899X/89/1/012005.

[134] J. Calvet, C. Renon, DISCONTINUOUS GROWTH OF CRYSTALS IN THE ALUMINUM-COPPER ALLOYS, Mem. Sci. Rev. Met. (1960). https://www.osti.gov/biblio/4177791 (accessed December 5, 2019).

[135] A. Gangulee, F.M. D'Heurle, Anomalous large grains in alloyed aluminum thin films I. Secondary grain growth in aluminum-copper films, Thin Solid Films. 12 (1972) 399–402. https://doi.org/10.1016/0040-6090(72)90103-4.

[136] B. Hutchinson, Origin of goss texture during secondary recrystallisation in silicon-steel, in: Mater. Sci. Forum, 2012: pp. 73–80. https://doi.org/10.4028/www.scientific.net/MSF.715-716.73.

[137] A. Bhattacharya, Y.F. Shen, C.M. Hefferan, S.F. Li, J. Lind, R.M. Suter, G.S. Rohrer, Three-dimensional observations of grain volume changes during annealing of polycrystalline Ni, Acta Mater. 167 (2019) 40–50. https://doi.org/10.1016/j.actamat.2019.01.022.

[138] M.A. Razzak, M. Perez, T. Sourmail, S. Cazottes, M. Frotey, A Simple Model for Abnormal Grain Growth, ISIJ Int. 52 (2012) 2278–2282. https://doi.org/10.2355/isijinternational.52.2278.

[139] A.D. Rollett, D.J. Srolovitz, M.P. Anderson, Simulation and theory of abnormal grain growth—anisotropic grain boundary energies and mobilities, Acta Metall. 37 (1989) 1227–1240. https://doi.org/10.1016/0001-6160(89)90117-X.

[140] K.J. Ko, P.R. Cha, D. Srolovitz, N.M. Hwang, Abnormal grain growth induced by sub-boundary-enhanced solid-state wetting: Analysis by phase-field model simulations, Acta Mater. 57 (2009) 838–845. https://doi.org/10.1016/j.actamat.2008.10.030.

[141] A.D. Rollett, W.W. Mullins, On the growth of abnormal grains, Scr. Mater. 36 (1997) 975–980. https://doi.org/10.1016/S1359-6462(96)00501-5.

[142] T.L. Burnett, S.A. McDonald, A. Gholinia, R. Geurts, M. Janus, T. Slater, S.J. Haigh, C. Ornek, F. Almuaili, D.L. Engelberg, G.E. Thompson, P.J. Withers, Correlative tomography, Sci. Rep. 4 (2014) 1–6. https://doi.org/10.1038/srep04711.

[143] T.J.A. Slater, R.S. Bradley, G. Bertali, R. Geurts, S.M. Northover, M.G. Burke, S.J. Haigh, T.L. Burnett, P.J. Withers, Multiscale correlative tomography: An investigation of creep cavitation in 316 stainless steel, Sci. Rep. 7 (2017) 1–10. https://doi.org/10.1038/s41598-017-06976-5.

[144] F. Bachmann, H. Bale, N. Gueninchault, C. Holzner, E.M. Lauridsen, 3D grain reconstruction from laboratory diffraction contrast tomography, J. Appl. Crystallogr. 52 (2019) 643–651. https://doi.org/10.1107/S1600576719005442.

[145] F. Shinichiro, H. Kenichi, Diffusion of gold and copper in aluminum, Trans. Japan Inst. Met. 20 (1970) 267–277. https://doi.org/10.2464/jilm.20.267.

[146] Lord Rayleigh, On the instability of jets, Proc. London Math. Soc. s1-10 (1878) 4–13. https://doi.org/10.1112/plms/s1-10.1.4.

[147] W.S. Tong, J.M. Rickman, K. Barmak, Quantitative analysis of spatial distribution of nucleation sites: Microstructural implications, Acta Mater. 47 (1999) 435–445. https://doi.org/10.1016/S1359-6454(98)00382-6.

[148] G. Gottstein, L.S. Shvindlerman, Grain Boundary Migration in Metals, Second Edi, CRC Press, 2009. https://doi.org/10.1201/9781420054361.

[149] W.W. Mullins, Estimation of the geometrical rate constant in idealized three dimensional grain growth, Acta Metall. 37 (1989) 2979–2984. https://doi.org/10.1016/0001-

6160(89)90333-7.

[150] J.K. Mason, E.A. Lazar, R.D. Macpherson, D.J. Srolovitz, Geometric and topological properties of the canonical grain-growth microstructure, Phys. Rev. E - Stat. Nonlinear, Soft Matter Phys. 92 (2015). https://doi.org/10.1103/PhysRevE.92.063308.

[151] A. Lawrence, J.M. Rickman, M.P. Harmer, A.D. Rollett, Parsing abnormal grain growth, Acta Mater. 103 (2016) 681–687. https://doi.org/10.1016/j.actamat.2015.10.034.

[152] J.M. Rickman, Y. Wang, A.D. Rollett, M.P. Harmer, C. Compson, Data analytics using canonical correlation analysis and Monte Carlo simulation, Npj Comput. Mater. 3 (2017) 26. https://doi.org/10.1038/s41524-017-0028-9.

[153] C. Wagner, Theorie der Alterung von Niederschlägen durch Umlösen (Ostwald-Reifung), Zeitschrift Für Elektrochemie, Berichte Der Bunsengesellschaft Für Phys. Chemie. 65 (1961) 581–591. https://doi.org/10.1002/BBPC.19610650704.

[154] J.E. May, D. Turnbull, Secondary recrystallization in silicon iron, Trans. Met. Soc. AIME. 212 (1958) 769.

[155] T. Gladman, Abnormal grain growth during the heat treatment of steel, Mater. Sci. Forum. 94–96 (1992) 113–128.

[156] S. Jin, S. Jin, M. Huang, Y. Kwon, L. Zhang, B. Li, S. Oh, J. Dong, D. Luo, M. Biswal, B. V Cunning, P. V Bakharev, I. Moon, W.J. Yoo, Y. Kim, S.H. Lee, B. Wang, W.K. Seong, M. Saxena, H. Shin, R.S. Ruoff, Colossal grain growth yields single-crystal metal foils by contact-free annealing, Science (80-.). 3373 (2018) 1–11. https://doi.org/10.1126/science.aao3373.

[157] G.C. Abbruzzese, C. Forzanti, Homogeneous abnormal grain growth in polycrystalline materials, in: Mater. Sci. Forum, Trans Tech Publications Ltd, 2012: pp. 1355–1360.

https://doi.org/10.4028/www.scientific.net/MSF.706-709.1355.

[158] G.C. Abbruzzese, Limit conditions for the onset of abnormal grain growth in a homogeneous microstructure: Theory and Experiments, in: J. Phys. Conf. Ser., IOP Publishing, 2019: p. 012036. https://doi.org/10.1088/1742-6596/1270/1/012036.

[159] P.R. Rios, Abnormal grain growth development from uniform grain size distributions, Acta Mater. 45 (1997) 1785–1789. https://doi.org/10.1016/S1359-6454(96)00284-4.

[160] C. Gini, Variabilità e mutabilità: contributo allo studio delle distribuzioni e delle relazioni statische, 1912. https://books.google.com/books?hl=en&lr=&id=fqjaBPMxB9kC&oi=fnd&pg=PA1&dq=C.+Gini:+Variabilità+e+mutabilità+(1912).&ots=EPABS7QAi8&sig=-mXIsqLEKTKHstBlswGAKwd1eDg#v=onepage&q=C. Gini%3A Variabilità e mutabilità (1912).&f=false (accessed June 23, 2022).

[161] C. Gin, Concentration and dependency ratios, Riv. Di Polit. Econ. 87 (1997) 769–790.

[162] W.J. Carrington, K.R. Troske, On measuring segregation in samples with small units, J. Bus. Econ. Stat. 15 (1997) 402–409. https://doi.org/10.1080/07350015.1997.10524718.

[163] S.J. Rey, R.J. Smith, A spatial decomposition of the Gini coefficient, Lett. Spat. Resour. Sci. 6 (2013) 55–70. https://doi.org/10.1007/s12076-012-0086-z.

[164] Z.I. Botev, J.F. Grotowski, D.P. Kroese, Kernel density estimation via diffusion, Ann. Stat. 38 (2010) 2916–2957. https://doi.org/10.1214/10-AOS799.

[165] E. Nes, N. Ryum, O. Hundert, On the zener drag-Addendum, Acta Metall. 37 (1989) 129–133. https://doi.org/10.1016/0001-6160(89)90272-1.

[166] A.W. Bowen, M.G. Ardakani, J.F. Humphreys, Deformation and recrystallization textures in Al-SiC metal-matrix composites, Mater. Sci. Forum. 157–162 (1994) 919–926.

[167] S.-J.L. Kang, Sintering: densification, grain growth, and microstructure, 2005. https://books.google.com/books?hl=en&lr=&id=uPWbuZohRmoC&oi=fnd&pg=PP2&ots=-EAiEyM4zt&sig=gnJp85oxUUs_atL4MvL2rxL_d1o#v=onepage&q&f=false (accessed June 23, 2022).

[168] J.O. Andersson, T. Helander, L. Höglund, P. Shi, B. Sundman, Thermo-Calc & DICTRA, computational tools for materials science, Calphad Comput. Coupling Phase Diagrams Thermochem. 26 (2002) 273–312. https://doi.org/10.1016/S0364-5916(02)00037-8.

[169] W.F. Smith, J. Hashemi, F. Presuel-Moreno, Foundations of Materials Science and Engineering, McGraw-Hill, 2006.

[170] V. Bezák, HOMOGENIZATION OF RANDOM CONCENTRATION PROFILES BY DIFFUSION., Met. Trans. 3 (1972) 1235–1237. https://doi.org/10.1007/BF02642457.

[171] H. Fredriksson, U. Åkerlind, Materials Processing during Casting, Wiley, 2006. https://doi.org/10.1002/9780470017920.

[172] E.M. Lifshitz, L.P. Pitaevskij, Statistical physics. Part 2. Theory of the condensed state, Butterworth-Heinenann, 1995. https://books.google.com/books?hl=en&lr=&id=lgiBDAAAQBAJ&oi=fnd&pg=PP1&ots=a-6ipZM_IA&sig=1I8zYgnVrL_IdxSHYgGRHcWpY14#v=onepage&q&f=false (accessed June 23, 2022).

[173] S. Nag, Y. Zheng, R.E.A. Williams, A. Devaraj, A. Boyne, Y. Wang, P.C. Collins, G.B. Viswanathan, J.S. Tiley, B.C. Muddle, R. Banerjee, H.L. Fraser, Non-classical homogeneous precipitation mediated by compositional fluctuations in titanium alloys, Acta Mater. 60 (2012) 6247–6256. https://doi.org/10.1016/j.actamat.2012.07.033.

[174] I. Kaur, Y. Mishin, W. Gust, Fundamentals of Grain and Interphase Boundary Diffusion,

3rd Editio, Wiley, 1995.

[175] J.R. Fernández, R.C. Pasianot, Grain-boundary diffusion by vacancy mechanism in α-Ti and α-Zr, Metall. Mater. Trans. A Phys. Metall. Mater. Sci. 33 (2002) 791–796. https://doi.org/10.1007/s11661-002-0146-x.

[176] N.L. Peterson, Diffusion mechanisms and structural effects in grain boundaries, J. Vac. Sci. Technol. A Vacuum, Surfaces, Film. 4 (1986) 3066–3070. https://doi.org/10.1116/1.573629.

[177] E.M. Lehockey, G. Palumbo, P. Lin, A. Brennenstuhl, Mitigating intergranular attack and growth in lead-acid battery electrodes for extended cycle and operating life, Metall. Mater. Trans. A Phys. Metall. Mater. Sci. 29 (1998) 387–396. https://doi.org/10.1007/s11661-998-0190-2.

[178] B. Alexandreanu, B. Capell, G.S. Was, Combined effect of special grain boundaries and grain boundary carbides on IGSCC of Ni-16Cr-9Fe-xC alloys, Mater. Sci. Eng. A. 300 (2001) 94–104. https://doi.org/10.1016/S0921-5093(00)01705-6.

[179] G. Palumbo, P.J. King, K.T. Aust, U. Erb, P.C. Lichtenberger, Grain boundary design and control for intergranular stress-corrosion resistance, Scr. Metall. Mater. 25 (1991) 1775–1780. https://doi.org/10.1016/0956-716X(91)90303-I.

[180] G. Wang, L. Zuo, C. Esling, Computer simulation on the tendency of intergranular fracture in textured polycrystalline materials, Philos. Mag. A Phys. Condens. Matter, Struct. Defects Mech. Prop. 82 (2002) 2499–2510. https://doi.org/10.1080/01418610208240049.

[181] K.T. Aust, U. Erb, G. Palumbo, Interface control for resistance to intergranular cracking, Mater. Sci. Eng. A. 176 (1994) 329–334. https://doi.org/10.1016/0921-5093(94)90995-4.

[182] A.S. Argon, Y. Qiao, Cleavage cracking resistance of large-angle grain boundaries in Fe-3 wt% Si alloy, Philos. Mag. A Phys. Condens. Matter, Struct. Defects Mech. Prop. 82 (2002) 3333–3347. https://doi.org/10.1080/01418610208240445.

[183] A.F. Gourgues, Electron backscatter diffraction and cracking, Mater. Sci. Technol. 18 (2002) 119–133. https://doi.org/10.1179/026708301125000320.

[184] H. Yoshida, K. Yokoyama, N. Shibata, Y. Ikuhara, T. Sakuma, High-temperature grain boundary sliding behavior and grain boundary energy in cubic zirconia bicrystals, Acta Mater. 52 (2004) 2349–2357. https://doi.org/10.1016/j.actamat.2004.01.026.

[185] V.Y. Gertsman, S.M. Bruemmer, Study of grain boundary character along intergranular stress corrosion crack paths in austenitic alloys, Acta Mater. 49 (2001) 1589–1598. https://doi.org/10.1016/S1359-6454(01)00064-7.

[186] E.A. Holm, P.M. Duxbury, Three-dimensional materials science, Scr. Mater. 54 (2006) 1035–1040. https://doi.org/10.1016/j.scriptamat.2005.11.048.

[187] D.B. Wells, J. Stewart, A.W. Herbert, P.M. Scott, D.E. Williams, Use of percolation theory to predict the probability of failure of sensitized, austenitic stainless steels by intergranular stress corrosion cracking, Corrosion. 45 (1989) 649–660. https://doi.org/10.5006/1.3579319.

[188] T. Keller, B. Cutler, E.A. Lazar, G. Yauney, D.J. Lewis, Comparative grain topology, Acta Mater. 66 (2014) 414–423. https://doi.org/10.1016/j.actamat.2013.11.039.

[189] B. Bokstein, V. Ivanov, O. Oreshina, A. Peteline, S. Peteline, Direct experimental observation of accelerated Zn diffusion along triple junctions in A1, Mater. Sci. Eng. A. 302 (2001) 151–153. https://doi.org/10.1016/S0921-5093(00)01367-8.

[190] D. Wolf, S. Yip, Material Interfaces: Atomic-level structure and properties, Chapman and

Hall, 1992.

[191] T. Frolov, Y. Mishin, Temperature dependence of the surface free energy and surface stress: An atomistic calculation for Cu(110), Phys. Rev. B - Condens. Matter Mater. Phys. 79 (2009) 045430. https://doi.org/10.1103/PhysRevB.79.045430.

[192] P. Volovitch, V. Traskine, L. Barrallier, Analysis of grain boundary network topology using grain boundary wetting, in: Zeitschrift Fuer Met. Res. Adv. Tech., De Gruyter, 2004: pp. 215–218. https://doi.org/10.3139/146.017935.

[193] J.A. Basinger, E.R. Homer, D.T. Fullwood, B.L. Adams, Two-dimensional grain boundary percolation in alloy 304 stainless steel, Scr. Mater. 53 (2005) 959–963. https://doi.org/10.1016/j.scriptamat.2005.06.026.

[194] D.G. Brandon, B. Ralph, S. Ranganathan, M.S. Wald, A field ion microscope study of atomic configuration at grain boundaries, Acta Metall. 12 (1964) 813–821. https://doi.org/10.1016/0001-6160(64)90175-0.

[195] J.M. Burgers, Geometrical considerations concerning the structural irregularities to be assumed in a crystal, Proc. Phys. Soc. 52 (1940) 23. https://doi.org/10.1088/0959-5309/52/1/304.

[196] M.E.J. Newman, R.M. Ziff, Fast Monte Carlo algorithm for site or bond percolation, Phys. Rev. E. 64 (2001) 16. https://doi.org/10.1103/PhysRevE.64.016706.

[197] R.M. Ziff, M.E.J. Newman, Convergence of threshold estimates for two-dimensional percolation, Phys. Rev. E. 66 (2002) 016129. https://doi.org/10.1103/PhysRevE.66.016129.

[198] A. Sikorski, The Influence of Temperature on the Percolation Threshold in Two-Dimensional Polymer Systems, CMST. 26 (2020) 143–149.

https://doi.org/10.12921/cmst.2020.0000040.

[199] C.A. Schuh, R.W. Minich, M. Kumar, Connectivity and percolation in simulated grain-boundary networks, Philos. Mag. 83 (2003) 711–726. https://doi.org/10.1080/0141861021000056681.

[200] R.W. Minich, C.A. Schuh, M. Kumar, Role of topological constraints on the statistical properties of grain boundary networks, Phys. Rev. B - Condens. Matter Mater. Phys. 66 (2002) 1–4. https://doi.org/10.1103/PhysRevB.66.052101.

[201] M. Frary, C.A. Schuh, Percolation and statistical properties of low- and high-angle interface networks in polycrystalline ensembles, Phys. Rev. B - Condens. Matter Mater. Phys. 69 (2004). https://doi.org/10.1103/PhysRevB.69.134115.

[202] F. Wakai, N. Enomoto, H. Ogawa, Three-dimensional microstructural evolution in ideal grain growth general statistics, Acta Mater. 48 (2000) 1297–1311. https://doi.org/10.1016/S1359-6454(99)00405-X.

[203] M.P. Anderson, G.S. Grest, D.J. Srolovitz, Computer simulation of normal grain growth in three dimensions, Philos. Mag. B Phys. Condens. Matter; Stat. Mech. Electron. Opt. Magn. Prop. 59 (1989) 293–329. https://doi.org/10.1080/13642818908220181.

[204] C.E. Krill, L.Q. Chen, Computer simulation of 3-D grain growth using a phase-field model, Acta Mater. 50 (2002) 3057–3073. https://doi.org/10.1016/s1359-6454(02)00084-8.

[205] T. Liu, S. Xia, B. Zhou, Q. Bai, G.S. Rohrer, Three-dimensional geometrical and topological characteristics of grains in conventional and grain boundary engineered 316L stainless steel, Micron. 109 (2018) 58–70. https://doi.org/10.1016/j.micron.2018.04.002.

[206] F.C. Hull, Plane section and spatial characteristics of equiaxed β-brass grains, Mater. Sci.

Technol. (United Kingdom). 4 (1988) 778–785. https://doi.org/10.1179/mst.1988.4.9.778.

[207] C. Zhang, A. Suzuki, T. Ishimaru, M. Enomoto, Characterization of three-dimensional grain structure in polycrystalline iron by serial sectioning, Metall. Mater. Trans. A Phys. Metall. Mater. Sci. 35 A (2004) 1927–1933. https://doi.org/10.1007/s11661-004-0141-5.

[208] M.N. Kelly, K. Glowinski, N.T. Nuhfer, G.S. Rohrer, The five parameter grain boundary character distribution of α-Ti determined from three-dimensional orientation data, Acta Mater. 111 (2016) 22–30. https://doi.org/10.1016/j.actamat.2016.03.029.

[209] M. Groeber, S. Ghosh, M.D. Uchic, D.M. Dimiduk, A framework for automated analysis and simulation of 3D polycrystalline microstructures. Part 1: Statistical characterization, Acta Mater. 56 (2008) 1257–1273. https://doi.org/10.1016/j.actamat.2007.11.041.

[210] A. Ullah, G. Liu, J. Luan, W. Li, M.U. Rahman, M. Ali, Three-dimensional visualization and quantitative characterization of grains in polycrystalline iron, Mater. Charact. 91 (2014) 65–75. https://doi.org/10.1016/j.matchar.2014.02.009.

[211] P.R. Rios, M.E. Glicksman, Self-similar evolution of network structures, Acta Mater. 54 (2006) 1041–1051. https://doi.org/10.1016/j.actamat.2005.10.027.

[212] R.M. Ziff, Spanning probability in 2D percolation, Phys. Rev. Lett. 69 (1992) 2670–2673. https://doi.org/10.1103/PhysRevLett.69.2670.

[213] D.T. Fullwood, J.A. Basinger, B.L. Adams, Lattice-based structures for studying percolation in two-dimensional grain networks, Acta Mater. 54 (2006) 1381–1388. https://doi.org/10.1016/j.actamat.2005.11.012.

[214] G. Abbruzzese, I. Heckelmann, K. Lücke, Statistical theory of two-dimensional grain growth-I. The topological foundation, Acta Metall. Mater. 40 (1992) 519–532. https://doi.org/10.1016/0956-7151(92)90401-Y.

[215] C. Donadille, R. Valle, P. Dervin, R. Penelle, Development of texture and microstructure during cold-rolling and annealing of F.C.C. alloys: Example of an austenitic stainless steel, Acta Metall. 37 (1989) 1547–1571. https://doi.org/10.1016/0001-6160(89)90123-5.

[216] D.S. Gaunt, M.F. Sykes, Series study of random percolation in three dimensions, J. Phys. A Gen. Phys. 16 (1983) 783–799. https://doi.org/10.1088/0305-4470/16/4/016.

[217] M.F. Sykes, D.S. Gaunt, M. Glen, Percolation processes in three dimensions, J. Phys. A Gen. Phys. 9 (1976) 1705–1712. https://doi.org/10.1088/0305-4470/9/10/021.

[218] V.A. Vyssotsky, S.B. Gordon, H.L. Frisch, J.M. Hammersley, Critical percolation probabilities (bond problem), Phys. Rev. 123 (1961) 1566–1567. https://doi.org/10.1103/PhysRev.123.1566.

[219] S.C. van der Marck, Percolation thresholds and universal formulas, Phys. Rev. E - Stat. Physics, Plasmas, Fluids, Relat. Interdiscip. Top. 55 (1997) 1514–1517. https://doi.org/10.1103/PhysRevE.55.1514.

[220] S.C. Van Der Marck, Calculation of percolation thresholds in high dimensions for FCC, BCC and diamond lattices, Int. J. Mod. Phys. C. 9 (1998) 529–540. https://doi.org/10.1142/S0129183198000431.

[221] M.F. Sykes, J.W. Essam, Critical percolation probabilities by series methods, Phys. Rev. 133 (1964) A310. https://doi.org/10.1103/PhysRev.133.A310.

[222] X. Xu, J. Wang, J.P. Lv, Y. Deng, Simultaneous analysis of three-dimensional percolation models, Front. Phys. 9 (2014) 113–119. https://doi.org/10.1007/s11467-013-0403-z.

[223] R. Zallen, The Physics of Amorphous Solids, Wiley Blackwell, 1998. https://doi.org/10.1002/9783527617968.

[224] C.D. Lorenz, R.M. Ziff, Precise determination of the bond percolation thresholds and

finite-size scaling corrections for the sc, fcc, and bcc lattices, Phys. Rev. E - Stat. Physics, Plasmas, Fluids, Relat. Interdiscip. Top. 57 (1998) 230–236. https://doi.org/10.1103/PhysRevE.57.230.

[225] S.M. Dammer, H. Hinrichsen, Spreading with immunization in high dimensions, J. Stat. Mech. Theory Exp. 2004 (2004) P07011. https://doi.org/10.1088/1742-5468/2004/07/P07011.

[226] J. Wang, Z. Zhou, W. Zhang, T.M. Garoni, Y. Deng, Bond and site percolation in three dimensions, Phys. Rev. E - Stat. Nonlinear, Soft Matter Phys. 87 (2013) 052107. https://doi.org/10.1103/PhysRevE.87.052107.

[227] J. Adler, Y. Meir, A. Aharony, A.B. Harris, L. Klein, Low-concentration series in general dimension, J. Stat. Phys. 58 (1990) 511–538. https://doi.org/10.1007/BF01112760.

[228] Y. Hu, P. Charbonneau, Percolation thresholds on high-dimensional Dn and E8 -related lattices, Phys. Rev. E. 103 (2021) 062115. https://doi.org/10.1103/PhysRevE.103.062115.

[229] M. Gell, D.N. Duhl, A.F. Giamei, DEVELOPMENT OF SINGLE CRYSTAL SUPERALLOY TURBINE BLADES, in: Superalloys, 1986: pp. 41–49.

[230] P.R. Rios, Overview no. 62. A theory for grain boundary pinning by particles, Acta Metall. 35 (1987) 2805–2814. https://doi.org/10.1016/0001-6160(87)90280-X.

[231] E. Orowan, Symposium on Internal Stresses in Metal, Inst. Met. London. (1947) 451.

[232] M. Dupraz, G. Beutier, T.W. Cornelius, G. Parry, Z. Ren, S. Labat, M.-I. Richard, G.A. Chahine, O. Kovalenko, ‖ M De Boissieu, E. Rabkin, ‖ M Verdier, O. Thomas, 3D Imaging of a Dislocation Loop at the Onset of Plasticity in an Indented Nanocrystal, Nano Lett. 17 (2017) 6696–6701. https://doi.org/10.1021/acs.nanolett.7b02680.

[233] M.A. Pfeifer, G.J. Williams, I.A. Vartanyants, R. Harder, I.K. Robinson, Three-

dimensional mapping of a deformation field inside a nanocrystal, (2006). https://doi.org/10.1038/nature04867.

[234] A. Ulvestad, M.J. Welland, W. Cha, Y. Liu, J.W. Kim, R. Harder, E. Maxey, J.N. Clark, M.J. Highland, H. You, P. Zapol, S.O. Hruszkewycz, G.B. Stephenson, Three-dimensional imaging of dislocation dynamics during the hydriding phase transformation, (2017) 16. https://doi.org/10.1038/NMAT4842.

[235] J.N. Clark, J. Ihli, A.S. Schenk, Y.-Y. Kim, A.N. Kulak, J.M. Campbell, G. Nisbet, F.C. Meldrum, I.K. Robinson, Three-dimensional imaging of dislocation propagation during crystal growth and dissolution, (2015). https://doi.org/10.1038/NMAT4320.

[236] R. Suter, Materials science: Multiscale measurements for materials modeling, Science (80-.). 356 (2017) 704–705. https://doi.org/10.1126/science.aan2544.

[237] J.H. Friedman, J.L. Bentley, R.A. Finkel, An Algorithm for Finding Best Matches in Logarithmic Expected Time, ACM Trans. Math. Softw. 3 (1977) 209–226. https://doi.org/10.1145/355744.355745.